UNIVERSIDAD NACIONAL DE GENERAL SAN MARTÍN
COMISIÓN NACIONAL DE ENERGÍA ATÓMICA
INSTITUTO DE TECNOLOGÍA
"Prof. Jorge A. Sabato"

Búsqueda de nueva física en quarks pesados en el LHC Run II [(*)]

por Lic. Mariel Estevez

Directores

Dr. Ezequiel Álvarez
Dr. Leandro Da Rold

[(*)] Tesis para optar al título de Doctor en Ciencia y Tecnología, mención Física

República Argentina

2020

UNIVERSIDAD NACIONAL DE GENERAL SAN MARTÍN
COMISIÓN NACIONAL DE ENERGÍA ATÓMICA
INSTITUTO DE TECNOLOGÍA
"Prof. Jorge A. Sabato"

Search for new physics in heavy quarks at the LHC Run II (*)

by Lic. Mariel Estevez

Supervisors

Dr. Ezequiel Álvarez
Dr. Leandro Da Rold

(*) Thesis submitted for the degree of Doctor in Science and Technology, Physics

República Argentina

2020

Para mis queridos Nico y Luken

Resumen

Las últimas décadas trajeron innumerables avances en el ámbito de la física de partículas, tanto en el campo experimental como en el teórico. El modelo estándar se erigió como una teoría casi cerrada, casi perfecta donde engranaje por engranaje todo parece funcionar. Los aceleradores permitieron testear con gran precisión los límites del modelo y traer a la luz hallazgos largamente esperados como el descubrimiento del bosón de Higgs. Sin embargo, muchas piezas aún no encajan. Elementos como la materia oscura, la energía oscura y los axiones nunca fueron detectados, entre otros, aunque son imprescindibles para explicar muchos fenómenos, y sin embargo cada día los experimentos siguen agregándole orden de precisión a los parámetros ya predichos por el modelo. La búsqueda de nuevas partículas deja de centrarse únicamente en la detección directa de producción de las mismas para buscar más minuciosamente la forma indirecta de medirlas. Esta tesis se propone estudiar algunas posibles formas de encarar la tarea desde un punto de vista más fenomenológico y plantea algunas mediciones indirectas para el LHC. En particular, la tercera generación de quarks, la más pesada, presenta un gran atractivo a la hora de buscar nuevas partículas. Esto se debe a sus particulares características, pero especialmente a la gran masa del quark top. Muchas teorías predicen que esta partícula podría estar acoplada de forma significativa a un sector con nuevas partículas aún desconocidas. Además, este quark es hoy en día una de las partículas menos estudiadas y que sin embargo tiene la posibilidad de ser producida en cantidad en el LHC.

Esta tesis es el compendio de varios trabajos diferentes que intentan encontrar fenomenológicamente el espacio de parámetros donde la búsqueda de nuevas partículas podría ser más sensible y también proponen observables y mediciones que podrían realizarse en el LHC con el fin de detectarlas de forma indirecta. Como primer trabajo, utilizamos un modelo con acoples genéricos a distintos tipos de partículas que interactúan con los quarks pesados, simulamos su producción en el LHC a través del uso del algoritmo de Monte Carlo y, haciendo uso de los límites experimentales actuales para la detección de nuevas partículas, mostramos el espacio de parámetros donde podría no haber sido descartada una partícula dentro de nuestras hipótesis. Como segundo trabajo, nos abocamos a la medición directa del elemento de mezcla V_{td}, el cual aún no ha sido medido con precisión y que, de existir una nueva física desconocida, podría acarrear variaciones inesperadas. Proponemos diversas búsquedas para el LHC y el (HL)LHC que podrían tener una significancia de más de dos sigmas. Por último, presentamos un software sencillo que, mediante la introducción numérica de acoples y anchos de decaimiento por parte del usuario, permite estimar la sensibilidad que tendrán los canales de decaimiento de una nueva partícula de cualquier modelo cuyos parámetros se utilicen. Como corolario, estudiamos la fenomenología de un modelo simplificado de la teoría de Randall Sundrum a energías del orden del TeV y estimamos, mediante el uso de nuestro software, en qué espacio de parámetros un nuevo bosón podría no estar descartado aún.

Abstract

The last decades brought innumerable developments in the field of particle physics, from the experimental and the theoretical point of view. The Standard Model was born as a theory almost closed, almost perfect where every single gear appears to be in its right place. The particle colliders allowed to probe the model to its limits and shed light into long-awaited discoveries, such as the detection of a Higgs boson. Nevertheless, there are many pieces which still do not fit. Dark matter, dark energy and axions has never been found, amongst others, although necessary to explain many phenomena, and yet everyday experiments keep on adding precision order to the parameters measurements already known by the model. The search for new particles stops centering on direct product detection of these particles to look for an indirect way to measure them. This thesis tries to study some possible ways of facing the job from a phenomenological point of view and presents some indirect measurements which could be done at the LHC. In particular, the third generation of quarks, the heavier one, represents a big attraction in the search for new particles. This is due to its particular characteristics, but specially because of the top's large mass. Many theories predict that it is this particle which is most strongly coupled to an unknown sector of particles. Besides, this quark is today one of the least tested particles and yet it can be produced in huge amounts at the LHC.

This thesis is a summary of different works which try to find phenomenologically the parameter space where the search of new particles could be more sensitive and also propose observables and measurements to perform at the LHC with the idea of detecting them in an indirect way. In the first work we use a model with generic couplings to different kinds of particles which interact with the heavy quarks and we simulated its production at the LHC through a Monte Carlo algorithm and, using the current known experimental limits for production of new particles. We find the space parameter of couplings where the existence of a new particle could be not excluded. As a second work, we dedicate to the direct measurement of the V_{td} quark mixing element, which still has not been measured with precision and, in case of the existence of new physics related to the top, it could present unexpected variations. We propose different searches to perform at the LHC and the (HL)LHC that could present more than two sigmas of significance. Lastly, we present a software that, by introducing numerical couplings and widths, allows to estimate the sensitivity that a decay channel of a new particle coupled to the Standard Model particles would present, using any model. As a corollary, we study the phenomenology of a simplified Randall Sundrum theory at lower energies and, using our software, estimate the parameter space in which a new boson could be excluded.

Agradecimientos

Antes que nada, quisiera agradecer al CONICET, al Instituto Sábato y a la UNSAM, otra más de *esas* universidades del conurbano, por darme el espacio y una beca para poder desarrollar mi doctorado, el cual hubiera sido imposible en otra situación. Quiero agradecer a mis directores, por haberme tomado como su estudiante y por las cosas que aprendí con ellos. A mis compañeros de oficina, por hacer las tardes más amenas, y en particular a Yamila, Rocío y Leonel, por los asados y los cafés, y a Rosa, por las charlas y por estar siempre ahí. A Ninja, por ayudarme a definir mi camino.

A los amigos que me dió la física, Ceci, Caro y Santiago, por ser de las personas más valiosas que conocí y que ya son amigos de la vida. A Yani, el Chino y Dani, por compartir las pequeñas cosas diarias y por ese guiso que ya va a llegar. A Sol, por estar a través del tiempo. A las chicas, las imprescindibles, por bancarme todos estos años, no me imagino que me falten.

A mi familia, con mención especial para Malena y Silvina. A Mari y Sergio, por toda la ayuda que nos dieron en este tiempo. A Laura y Roberto, que siempre están cuando más se los necesita. A mis padres, por haberme dado la libertad de elegir qué hacer con mi vida y haberme apoyado siempre. A mi hermana, que me enseñó sobre física y astronomía, y sin la cual no estaría escribiendo esto hoy. Espero que sigamos acompañándonos siempre. Ustedes saben lo que los quiero y necesito. A Nico, el mejor compañero de vida, que me apoyó enormemente todos estos años y cuya presencia es incondicional para mí. Y por último, pero acaso el más importante, Luken, porque una sonrisa tuya me llena de vida. Los amo profundamente a ambos, todo es mejor cuando están conmigo.

Gracias.

Table of Contents

CHAPTER 1

INTRODUCCIÓN

Desde que el Modelo Estándar (ME) fue formulado hace 50 años, las búsquedas de Nueva Física (NF) se pensaron siguiendo el objetivo de lograr una teoría completa que, además de resolver muchos de los problemas observacionales, también resuelva problemas teóricos como las divergencias ultravioletas (UV) y el problema de jerarquía, entre otros. Dados los resultados negativos en búsquedas experimentales de NF hasta ahora, podría ser útil empezar a considerar que al siguiente nivel energético quizás la NF pueda ser vista sólo como una teoría incompleta con muchos parches para ser comprendida y resuelta, permitiendo el desarrollo de una teoría completa a un nivel de energía mayor, como por ejemplo Supersimetría [1, 2] o Dimensiones Extra [3], entre otras. Este nuevo escenario puede conducir a formulaciones más fenomenológicas.

A lo largo de esta tesis estudiaremos distintas teorías fenomenológicas simplificadas y modelos. Además propondremos observables y formas de medirlos de modo de resaltar las características que distinguen la NF del ME, basados en la idea de que una nueva partícula podría estar fuertemente acoplada al quark top e incluso al quark bottom. Consideramos que la tercera generación de quarks es una interesante puerta de entrada al mundo de la NF.

En este capítulo repasaremos los atributos tanto teóricos como experimentales que poseen los quarks pesados y que podrían estar relacionados con posibles pistas que apunten hacia la NF. Nos enfocaremos en las características básicas del quark top y rastros de NF en las búsquedas del LHC de estados con quarks pesados, como así también en la forma en la que los quarks se mezclan entre sí y las carcaterísticas especiales que aparecen. En el próximo capítulo estudiaremos un modelo fenomenológico simplificado de una teoría muy conocida mas allá del ME, en la cual nuevos bosones se acoplan fuertemente al quark top.

En las próximas secciones mostraremos estudios fenomenológicos y búsquedas de NF usando los resultados ya existentes del LHC, incluído un análisis genérico para la búsqueda de nuevas

partículas y propuestas para mediciones directas del parámetro de mezcla que relaciona al quark top con el quark down.

1.1 ¿ Por qué la tercera generación de quarks?

Los quarks bottom y top también se conocen como quarks pesados. Tienen las masas más grandes entre los quarks y, de hecho, el top quark es la partícula más pesada del ME. Su enorme masa cercana a la escala de ruptura de simetría electrodébil (EWSB) implica un gran acoplamiento con el bosón de Higgs, lo que convierte al top en un intermediario privilegiado del sector de Higgs. Este quark además tiene un tiempo de vida tan corto que se desintegra antes de la hadronización, lo que nos permite estudiar sus propiedades, conservadas en la descomposición y transferidas a las partículas hijas. Debido a estas características especiales, el quark top juega un papel esencial en la búsqueda de NF. Existen varios modelos que predicen la existencia de nuevas partículas acopladas a este quark. Esto suele ser debido a su gran masa, dado que la misma implica un acople de Yukawa grande (cercano a uno), y es posible pensar en nuevas partículas pesadas con las mismas características. En la Secc. 3 estudiamos una de estas teorías. Conocer al quark top podría ayudarnos a encontrar nuevas partículas ocultas.

El estudio experimental de estados finales con quarks de sabores pesados siempre ha sido un área interesante a partir del cual buscar desviaciones del ME, y en particular en el LHC, Tevatron y LEP esto se ha llevado a cabo para la tercera generación de quarks. El estudio de pares de quarks de la tercera generación ha dado resultados esperados en el marco del ME para $t\bar{t}$ en el LHC [4, 5] y Tevatron [6], mientras que $b\bar{b}$ ha sido un proceso difícil de estudiar en estas máquinas hadrónicas debido a la gran cantidad de procesos de background y a muy pocos resultados limpios disponibles al día de hoy [7, 8]. En el LEP, el estado final $b\bar{b}$ dejó una de sus mayores desviaciones en lo que se conoce como la b -anomalía LEP [9].

El estudio de estados finales con tres o más quarks de tercera generación en el LHC es un campo en desarrollo que está generando un importante conjunto de nuevos resultados. El estado final de cuatro bottoms generalmente se estudia en búsquedas de Higgs pesados que se producen a través de la fusión $b\bar{b}$ y que también decae a $b\bar{b}$ [10–12]. Sin embargo, este estado final tiene la dificultad de estar oculto en los backgrounds de QCD, además de que taggear a los bottoms resulta una tarea difícil. El estado final de cuatro tops se analiza muchas veces como posible señal de resonancias pesadas que decaen a $t\bar{t}$ [13], y también, en especial en los últimos tiempos, al buscar el proceso del ME de cuatro tops [14, 15] que también puede ocultar NF no resonante [16]. Sin embargo, el de cuatro tops es un estado final muy pesado y, por lo general, su sección eficaz tiene supresiones importantes. Este estado tiene además la característica de ser muy poblado, lo que puede generar dificultades en su reconstrucción. Sin embargo, el estado final de $t\bar{t}b\bar{b}$ [17, 18] es el término medio entre los dos estados finales anteriores y es muy interesante porque la mayoría de las dificultades mencionadas anteriormente se reducen mientras que aún presenta

los efectos atractivos de la NF. Es por ello que nos dedicaremos al estudio de su fenomenología en el LHC.

1.1.1 Posibles pistas

La mayoría de los estados finales mencionados tienen pequeños excesos que se agrandan a medida que aumenta el número de b taggeados. Por ejemplo, y sin ser exhaustivos, en la búsqueda de ATLAS del cuatro tops en la Ref. [19], la comparación de la predicción con los datos en todas las regiones de control y señal produce una desviación sistemática que crece a medida que el número de b taggeados requeridos va de 2 a 4. En el primer estudio de ATLAS sobre $t\bar{t}b\bar{b}$ [20], la sección eficaz fiducial medida fue de 2σ más allá de la predicción del ME. Los resultados posteriores [18] que incluyen más datos y algunos nuevos análisis redujeron este exceso a 1.2σ. La Ref. [18] dedica una sección completa a discutir posibles ajustes diferentes del Montecarlo, principalmente en los kernels de división $g \to b\bar{b}$ cuyo ajuste tiene un efecto importante en los datos para tener acuerdo en la predicción. El estudio de CMS sobre $t\bar{t}b\bar{b}$ fue abordado desde el principio de forma tal de reducir el impacto de eventuales problemas de Montecarlo debido al par de b en el estado final. En su primer trabajo [17] presentaron una comparación entre $\sigma(t\bar{t}b\bar{b})$ y $\sigma(t\bar{t}jj)$ con un exceso de 1σ. En su segundo artículo [21] han presentado medidas diferenciales relevantes en variables cinemáticas como $\Delta R_{b\bar{b}}$ y $m_{b\bar{b}}$, en las que una señal resonante puede distinguirse utilizando medidas de banda lateral. Curiosamente, ambas mediciones tienen excesos de $\sim 1.5\sigma$ en el bineado de $\Delta R_{b\bar{b}}$ back-to-back y en el bineado de masa grande $m_{b\bar{b}} > 170$ GeV. Estas mediciones también se realizan en el estado final $t\bar{t}jj$ bajo condiciones similares y no se encuentra exceso ni en ΔR_{jj} ni en m_{jj}. También es interesante notar que se necesitan aplicar factores de normalización de 2 y 4 para todas las predicciones sobre cantidades de leading y subleading jets de b para llegar a un acuerdo con los datos, lo que refleja algún problema, al menos en Montecarlo.

En los últimos años, los resultados preliminares de $t\bar{t}b\bar{b}$ de ATLAS [22] y CMS [23] aparecieron en los datos de 13 TeV. Los resultados de ATLAS, antes de ajustar el Montecarlo a los datos, muestran nuevamente un exceso que aumenta con el número de b taggeados. Este exceso desaparece después de realizar un ajuste a los datos bajo la hipótesis de que sólo hay background. El cociente de CMS [23] $\sigma(t\bar{t}b\bar{b})/\sigma(t\bar{t}jj)$ produce un exceso de 1.5σ en comparación con la predicción del ME. Sin embargo, en esta tesis restringiremos el análisis principal a los datos publicados en $t\bar{t}b\bar{b}$ [17, 18], que corresponde a datos de 7 y 8 TeV. También hay muchos trabajos teóricos que han abordado los estados finales $t\bar{t}b\bar{b}$ [24–29] y $t\bar{t}t\bar{t}$ [30, 31]. Los resultados más recientes publicados en 2020 del cuatro tops y búsquedas de $t\bar{t}b\bar{b}$ mantienen algunos de los resultados de los experimentos anteriores. En el trabajo publicado por ATLAS [32] donde se estudió el estado final de cuatro tops a 13 TeV, todavía se pueden encontrar desviaciones de alrededor de $\sim 2\sigma$, especialmente cuando una gran cantidad de b jets son taggeados. Los factores de normalización siguen presentes. Por otro lado, el trabajo publicado por CMS [33] también presenta excesos y

desviaciones. Se dice en la publicación que la relación de la sección eficaz medida es mayor que la predicción simulada por un factor de 1.3, con una significancia de 3σ en el canal de dileptón (ver la Fig. 1.1). Se menciona que una relación de sección eficaz mayor con respecto a la predicción por un factor de 1.8 a 2σ también estuvo presente en una medición previa realizada por CMS a 13 TeV.

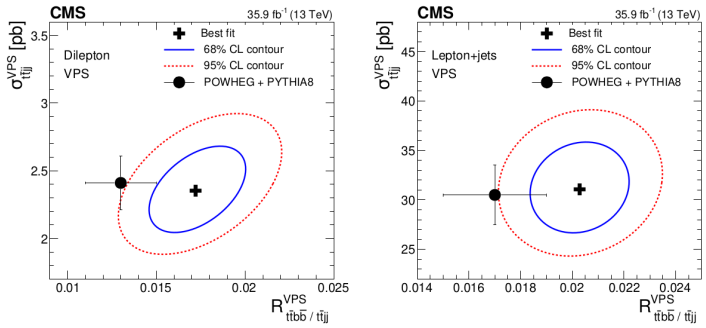

Figure 1.1: Ajuste simultáneo para $R_{ttbb/ttjj}$ y σ_{ttjj} en el espacio de fase visible (marcado con una cruz). El punto representa la predicción. Gráficos extraídos del trabajo publicado por CMS [33].

Aunque los resultados aquí mencionados son meros excesos y no estamos sugiriendo que representen un descubrimiento real, los consideramos como motivación y punto de partida para estudiar formas de encontrar y medir observables que podrían arrojar pistas asociadas a la existencia de nuevas partículas.

1.2 Modelos de NF simplificados

Debido a que aún no se ha encontrado ninguna señal real de nuevas partículas, decidimos realizar un estudio fenomenológico en el que usamos modelos simplificados de NF donde una nueva partícula se acopla a la tercera generación de quarks a través de acoplamientos genéricos. Estos modelos deben presentar las características básicas de dichas partículas sin las dificultades extra que introduciría una teoría completa. Presentamos cuatro modelos en los que la nueva partícula es un escalar, un pseudoescalar, un vector y un gravitón. Restringimos nuestro estudio a una NF eléctricamente neutra, aunque también hay modelos interesantes que introducen NF cargada. Dependiendo de la magnitud de los parámetros en el modelo, este tipo de NF se manifestaría principalmente en estados finales como $t\bar{t}b\bar{b}$, $t\bar{t}t\bar{t}$, $b\bar{b}b\bar{b}$, $t\bar{t}$ y $b\bar{b}$. En particular, la sensibilidad relativa de estos estados finales a la NF cambiará drásticamente dependiendo de si la masa de la nueva partícula es más pesada o más ligera que $2m_t$.

Para mantener la discusión lo más general posible, no hacemos suposiciones en el modelo subyacente, simplemente nos enfocamos en la fenomenología y presentamos posibles lagrangianos de NF simplificados que se acoplan a los quarks top y bottom.

1.2.1 Escalar ϕ

El caso de un campo escalar masivo que se acopla exclusivamente a los quark top y bottom es uno de los modelos de NF más simples. Sin embargo, un campo escalar abre la posibilidad a distintos problemas, ya que involucra interacciones con quarks izquierdos y derechos, lo que produce un vértice con una estructura no trivial del gauge EW dentro del ME. Sin embargo, este tipo de términos interactuantes se pueden lograr en una variedad de modelos sin mayores complicaciones, ya que el vértice efectivo puede entenderse, por ejemplo, como proveniente de operadores de dimensiones superiores o de una ruptura espontánea de la simetría. Los parámetros de dicho modelo pueden, en general, coincidir con los modelos completos UV, como algunos de los muchos modelos disponibles dentro de la teoría del Two Higgs Doublet Model (2HDM) (ver, por ejemplo, y sin ser exhaustivos, Refs. [34–36]). El problema principal aquí puede ser cuán independientes pueden ser los acoplamientos de los quarks top y bottom. En un 2HDM, esto se aborda con el parámetro libre $\tan\beta$, aunque podría darse el caso de que, para valores arbitrarios dados de los acoplamientos del top y del bottom, este escenario particular UV completo pueda estar restringido en el espacio de parámetros por otros límites experimentales situados dentro del caso 2HDM específico que corresponda. En cualquier caso, destacamos que el análisis en este trabajo se centra en los lagrangianos de NF fenomenológicos, más que en las teorías completas UV. Otro problema con este modelo es que para grandes acoplamientos con quarks bottom y masas pequeñas, podría entrar en conflicto con los observables de precisión LEP.

Para el caso escalar estudiamos el siguiente lagrangiano simplificado

$$L_\phi^{tree} = c_{\phi t}\,\bar{t}_L \phi t_R + c_{\phi b}\,\bar{b}_L \phi b_R + h.c. \tag{1.1}$$

Se puede agregar al lagrangiano un acoplamiento efectivo a los gluones del tipo $gg\phi$ debido a un lazo de top y bottom virtuales. El lagrangiano extra en este caso es

$$L_\phi^{loop} = \frac{\alpha_s}{12\sqrt{2}\pi}\left[\frac{c_{\phi t}}{m_t}F(z_t) + \frac{c_{\phi b}}{m_b}F(z_b)\right]\phi G^a_{\mu\nu}G_a^{\mu\nu} \tag{1.2}$$

donde

$$z_{t,b} = (2m_{t,b}/M)^2$$

con M la masa de resonancia (en este caso $M = M_\phi$), y $F(z)$ la función de lazo que puede encontrarse en el Apéndice.

El lagrangiano de NF efectivo interactuante es entonces

$$L_\phi = L_\phi^{tree} + L_\phi^{loop}. \tag{1.3}$$

1.2.2 Pseudoescalar A

El caso pseudoescalar, que también podría entenderse como miembro de un 2HDM, tiene el siguiente lagrangiano

$$L_A^{tree} = c_{At}\,\bar{t}_L A i\gamma^5 t_R + c_{Ab}\,\bar{b}_L A i\gamma^5 b_R + h.c. \tag{1.4}$$

El lagrangiano efectivo a un lazo que se acopla a ggA es

$$L_A^{loop} = -\frac{\alpha_s}{8\sqrt{2}\pi}\left[\frac{c_{At}}{m_t}H(z_t)+\frac{c_{Ab}}{m_b}H(z_b)\right]A\,G^a_{\mu\nu}\tilde{G}^{\mu\nu}_a, \tag{1.5}$$

donde la función de lazo $H(z)$ se puede encontrar en el Apéndice. El lagrangiano pseudoescalar completo es $L_A = L_A^{tree} + L_A^{loop}$.

1.2.3 Escalar CP-violador φ

El último caso de espín 0 es el de un escalar violador de CP φ cuyo lagrangiano a nivel árbol es

$$L_\varphi^{tree} = c_{\varphi t}\,\bar{t}_R\varphi(1+i\gamma^5)t_L + c_{\varphi b}\,\bar{b}_R\varphi(1+i\gamma^5)b_L + h.c. \tag{1.6}$$

El lagrangiano a nivel de lazo es el correspondiente a la suma de los lagrangianos en las Ecs. 2.2 y 2.5 después de reemplazar $\phi,\ A \to \varphi$.

1.2.4 Vector Z'

Un Z' con espín uno, incoloro y neutral con masa $M_{Z'}$ que se acopla exclusivamente a t y b resulta ser el modelo con menor cantidad de posibles problemas. Para mantener los acoplamientos con el top y el bottom como parámetros libres independientemente del grupo de gauge EW del ME, solo mantenemos acoplamientos para quarks diestros. Esto también ayuda a evitar conflictos con las mediciones de precisión de LEP. La interacción de un Z' con las partículas del ME es

$$L_{Z'} = -c_{Z't}\,\bar{Z}'_\mu t_R\gamma^\mu t_R - c_{Z'b}\,Z'_\mu\bar{b}_R\gamma^\mu b_R. \tag{1.7}$$

Como el Z' tiene espín uno, no puede acoplarse a ningún orden a un estado inicial de gg.

1.2.5 Vector axial $\tilde{Z}'$

Como caso adicional de espín uno, también estudiamos un vector cuyo acople es puramente axial y se acopla a los fermiones

$$L_{\tilde{Z}'} = -c_{\tilde{Z}'t}\,\tilde{Z}'_\mu\bar{t}\gamma^5\gamma^\mu t - c_{\tilde{Z}'b}\,\tilde{Z}'_\mu\bar{b}\gamma^5\gamma^\mu b. \tag{1.8}$$

Esta partícula tampoco puede acoplarse a un estado inicial gg.

1.2.6 Gravitón G

Consideramos un lagrangiano efectivo para un gravitón de espín 2 con campo $\hat{G}_{\mu\nu}$. El lagrangiano de interacción a nivel de lazo es

$$L_G^{tree} = -\frac{i}{2\Lambda}\hat{G}^{\mu\nu}\left[c_{Gt}\left(\bar{t}_R\gamma_\mu\overleftrightarrow{D}_\nu t_R - \eta_{\mu\nu}\bar{t}_R\gamma^\rho\overleftrightarrow{D}_\rho t_R\right) + c_{Gb}\left(\bar{b}_R\gamma_\mu\overleftrightarrow{D}_\nu b_R - \eta_{\mu\nu}\bar{b}_R\gamma^\rho\overleftrightarrow{D}_\rho b_R\right)\right], \tag{1.9}$$

donde $\bar{f}\gamma_\mu \overleftrightarrow{D}_\nu f = \bar{f}\gamma_\mu D_\nu f - D_\nu \bar{f}\gamma_\mu f$. Para los propósitos de este trabajo, solo usamos el término de derivada parcial en la derivada covariante, ya que despreciamos la interacción de 4 partículas contenida en los otros términos.

A diferencia de los modelos de NF anteriores, el lagrangiano de espín 2 necesita acoplamientos dimensionales, y es por eso que la constante dimensional Λ aparece en el denominador. Durante toda esta tesis tomaremos entonces

$$\Lambda = 1 \text{ TeV}.$$

Esta elección arbitraria coincide con las secciones eficaces $\sigma(b\bar{b} \to G) = \sigma(b\bar{b} \to \phi)$ para los mismos valores numéricos de los acoplamientos $c_{\phi b} = c_{Xb} = 1$ y $M_G = M_\phi = 300$ GeV. Por supuesto que esta concordancia se pierde a medida que se modifican los valores numéricos de los acoplamientos o la masa de la resonancia, ya que ambos modelos tienen una dinámica diferente. Esta elección es solo para tener un punto de contacto para el modelo de NF espín 2 cuyos acoplamientos no son adimensionales.

El lagrangiano efectivo de un lazo que acopla ggG es

$$L_G^{loop} = -\frac{\alpha_s}{12\pi\Lambda}\left[c_{Gt}A_G(z_t,\mu_0) + c_{Gb}A_G(z_b,\mu_0)\right]\hat{G}_{\mu\nu}\left(\frac{\eta^{\mu\nu}}{4}G^a_{\rho\sigma}G^{\rho\sigma}_a - G^{a\mu}_\rho G^{\nu\rho}_a\right). \tag{1.10}$$

Aquí μ_0 es la escala de renormalización y la función de lazo $A_G(z,\mu_0)$ puede encontrarse en el Apéndice. El lagrangiano de espín 2 completo es $L_G = L_G^{tree} + L_G^{loop}$.

1.3 Mezcla de quarks

Otra característica interesante del quark top es su mezcla con quarks livianos. Los ángulos que determinan la mezcla son parámetros que actualmente se conocen con un alto porcentaje de incertidumbre y que representan un buen lugar a la hora de buscar nuevos acoplamientos. En esta sección haremos un breve repaso de la teoría de la mezcla de quarks.

Los quarks, al igual que los leptones, interactúan electromagnéticamente a través de la fuerza débil. Es posible modelar la corriente cargada como

$$J_q^\mu = \overline{u}_u \gamma^\mu \frac{1}{2}(1-\gamma^5)u_d, \tag{1.11}$$

donde u es el campo de quark. Esta corriente tiene una estructura vectorial-axial, ya que su acoplamiento involucra a un escalar y a la matriz γ^5. Por lo tanto, solo puede acoplar u y d zurdos o bien $\overline{u}$ y $\overline{d}$ zurdos, y siempre quarks pertenecientes a la misma familia. Esta corriente puede acoplarse a los bosones dando como resultado interacciones como en la Fig. 1.2.

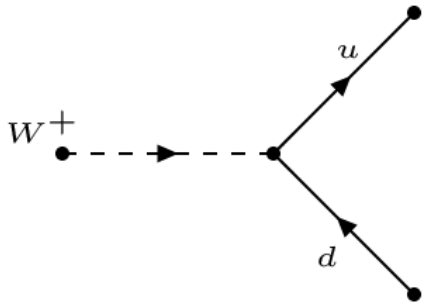

Figure 1.2: Diagrama de Feynman para la corriente de los quarks acoplada al bosón débil W^+.

Esto funciona bien para la primera generación de quarks, pero con el tiempo los físicos se dieron cuenta de que no podía explicar las interacciones observadas con quarks más pesados, al igual que el decaimiento de kaones $K^+ \to \mu^+ \nu_\mu$ con K^+ constituido por quarks u y $\overline{s}$. Para evitar la introducción de nuevos acoplamientos especializados en cada interacción, Cabibbo propuso en 1963 [37] rotar los quarks con un ángulo de mezcla, un parámetro arbitrario conocido como el ángulo de Cabibbo θ_c. De esta manera, los dobletes

$$\begin{pmatrix} u \\ d \end{pmatrix} \quad , \quad \begin{pmatrix} c \\ s \end{pmatrix} \tag{1.12}$$

cuando participan de interacciones son cambiados por los nuevos dobletes

$$\begin{pmatrix} u \\ d' \end{pmatrix} \quad , \quad \begin{pmatrix} c \\ s' \end{pmatrix} \tag{1.13}$$

definidos por

$$d' = d\cos\theta_c + s\sin\theta_c, \tag{1.14}$$

$$s' = -d\sin\theta_c + s\sin\theta_c. \tag{1.15}$$

El quark strange s introduce el número cuántico S al proceso, llamado rareza. Si hay un cambio de sabor en una descomposición, donde se crea o destruye un quark s, hay un cambio en la extrañeza que se puede determinar. Cabibbo introdujo su rotación para explicar este fenómeno, ya que permitía cambios de sabor, con $\Delta S = 1$. Los experimentos mostraron que las transiciones con $\Delta S = 1$ se suprimen por un factor de 20 con respecto a las transiciones sin cambio de sabor [38]. Eso dio como resultado que el ángulo de Cabibbo debiera ser $\theta_c \approx 13°$. Como resultado, hay algunas transiciones favorecidas y algunas suprimidas, véanse las Figs. 1.3.

La corriente puede escribirse entonces como

$$J^\mu = (\overline{u} \quad \overline{c}) \frac{\gamma^\mu(1-\gamma^5)}{2} V \begin{pmatrix} d \\ s \end{pmatrix} \tag{1.16}$$

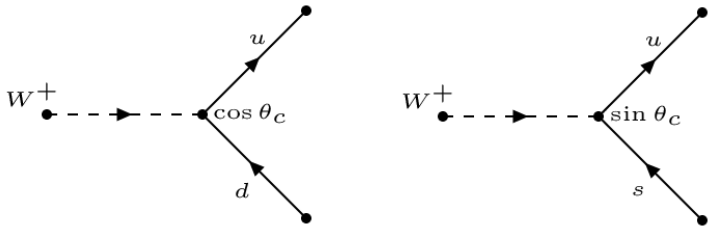

Figure 1.3: Diagramas de Feynman para el proceso de decaimiento del bosón W^+ en quarks. El de la izquierda se ve favorecido por la mezcla, con un acoplamiento proporcional a $\cos\theta_c$, mientras que el de la derecha se suprime debido a la mezcla, con un acoplamiento proporcional a $\sin\theta_c$.

donde V es la matriz de rotación definida por

$$\begin{pmatrix} \cos\theta_c & \sin\theta_c \\ -\sin\theta_c & \cos\theta_c \end{pmatrix}. \tag{1.17}$$

Los quarks d y s originales son los llamados estados de masa, o físicos, porque son los quarks que aparecen en el término de masa dentro del lagrangiano. Los nuevos estados d' y s' son combinaciones ortogonales de los primeros y aparecen en el término de interacciones. Son dados formalmente por el mecanismo Cabibbo-GIM

$$\begin{pmatrix} d' \\ s' \end{pmatrix} = \begin{pmatrix} \cos\theta_c & \sin\theta_c \\ -\sin\theta_c & \cos\theta_c \end{pmatrix} \begin{pmatrix} d \\ s \end{pmatrix} \tag{1.18}$$

Este mecanismo permite el cambio de extrañeza en el estado final pero asegura que no haya cambio en la carga eléctrica de los quarks. Kobayashi y Maskawa lo generalizaron a las tres generaciones de quarks años después [39]. Escribimos a continuación la corriente en esta nueva formulación, donde V es ahora una matriz de 3×3 y la nueva corriente viene dada por

$$J^\mu = (\overline{u} \quad \overline{c}\overline{t}) \frac{\gamma^\mu(1-\gamma^5)}{2} V_{CKM} \begin{pmatrix} d \\ s \\ b \end{pmatrix} \tag{1.19}$$

donde V_{CKM} es la matriz Cabibbo-Kobayashi-Maskawa. Puede parametrizarse mediante tres ángulos de mezcla (análogos al ángulo de Cabibbo) y una fase KM que viola CP. Cada uno de los coeficientes V_{ij} representa la mezcla entre el quark i y el quark j y en la actualidad los conocemos experimentalmente como

$$V_{CKM} = \begin{pmatrix} V_{ud} & V_{us} & V_{ub} \\ V_{cd} & V_{cs} & V_{cb} \\ V_{td} & V_{ts} & V_{tb} \end{pmatrix} \approx \begin{pmatrix} 0.974 & 0.225 & 0.004 \\ 0.224 & 0.974 & 0.042 \\ 0.009 & 0.041 & 0.999 \end{pmatrix}. \tag{1.20}$$

Se puede ver que los elementos de la diagonal están muy cerca de la unidad mientras que los demás son mucho más pequeños. Esto se debe a que, como ya se dijo, hay algunas transiciones

que se favorecen. Corresponden a las interacciones entre quarks de la misma generación, como si no hubiera mezcla entre ellos. Las interacciones debidas a la mezcla de Cabibbo se encuentran suprimidas. De la unitaridad de la matriz, podemos derivar condiciones sobre los elementos, $\sum_i V_{ij}V_{ik}^* = \delta_{jk}$ y $\sum_j V_{ij}V_{kj}^* = \delta_{ik}$. Estas condiciones dan seis relaciones igualadas a cero que se pueden interpretar gráficamente en términos de triángulos en un plano complejo.

Las entradas en la matriz CKM que gobiernan las transiciones de sabor entre quarks son parámetros fundamentales del ME. Como tales, merecen un intenso escrutinio experimental. Actualmente, las dos primeras filas de la CKM ya se están testeando directamente con una precisión cada vez mayor utilizando desintegraciones de núcleos, kaones, mesones charm y hadrones B [40]. Por otro lado, existen pocas mediciones experimentales directas en la tercera fila de la CKM. En esta tesis estudiaremos formas directas de medir V_{td} y, por lo tanto, solo nos interesarán los elementos V_{tq} de la matriz CKM.

1.3.1 Medición de los elementos $|V_{tq}|$

Las predicciones del ME para los elementos de matriz V_{tq}, con $q = d,s,b$ se derivan actualmente de consideraciones de unitaridad de la CKM, así como de las mediciones de decaimientos radiativos y oscilaciones de mesones B, donde V_{tq} aparece en lazos que involucran tops virtuales. Un ajuste global reciente de la CKM arroja [41]

$$|V_{tb}^{SM}| = 1 - 8.81^{+0.12}_{-0.24} \times 10^{-3}, \quad |V_{ts}^{SM}| = 41.08^{+3.0}_{-5.7} \times 10^{-3}, \quad |V_{td}^{SM}| = 8.575^{+0.076}_{-0.098} \times 10^{-3}. \quad (1.21)$$

Mediciones de fracciones de b-jet en decaimientos del top $t \to Wj$ hoy en día ponen una cota en [42]

$$\frac{B(t \to bW)}{\sum_{q=d,s,b} B(t \to qW)} > 0.955 \ @ \ 95\% \ C.L., \quad (1.22)$$

que puede ser interpretado como $\sqrt{|V_{td}|^2 + |V_{ts}|^2} < 0.217|V_{tb}|$. Además, mediciones precisas de la producción de un solo canal de t y su asimetría de carga en el LHC [43–45] en comparación con las predicciones teóricas precisas [46–49], pueden interpretarse como mediciones de $|V_{tq}|$. Un análisis de ATLAS reciente que ignora los efectos de $|V_{td,ts}|$ encontró que $|V_{tb}| = 1.07 \pm 0.09$ [43]. Si bien, en principio, estas mediciones también pueden probar los elementos de matriz $|V_{ts}|$ y $|V_{td}|$ [50] [51], están intrínsecamente limitadas por los antecedentes y las incertidumbres estadísticas y sistemáticas asociadas. En consecuencia, especialmente en el caso de $|V_{td}|$, no se espera que se acerquen ni siquiera al orden de magnitud de las predicciones del ME.

1.4 La fuerza

Cuando se estudian modelos de nueva física es muy frecuente analizar diferentes estados finales para encontrar algo que sea diferente del ME. Una posibilidad para lograr este objetivo es diseñar estrategias de búsqueda para cada uno de los estados finales y calcular el alcance de

exclusión/descubrimiento para cada estado final, de forma tal de concluir qué canal es el más sensible y qué luminosidad se requiere para poder excluir/descubrir cada punto del espacio de parámetros.

En esta tesis proponemos considerar un segundo y más práctico camino: usar las estrategias de búsqueda ya disponibles utilizadas por los experimentales. Las mismas tienen una sensibilidad que viene resumida en los límites de 95 % CL en la sección eficaz (σ) por la aceptancia (A) multiplicadas por las relaciones de ramificación (BR) de una nueva partícula hipotética. Usando estos resultados, se puede calcular en un canal dado la relación entre el valor de $\sigma \times A \times BR$ esperado en el caso de NF y el límite esperado correspondiente en esas estrategias de búsqueda. Esta relación es la fuerza (*strength*) del canal dado expresada de tal manera que se pueda comparar directamente con la misma relación en otros canales. Es decir que están en las mismas unidades de sensibilidad. Más precisamente, definimos la fuerza de un estado final dado como

$$S = \frac{\sigma^{NP} \times BR \times A}{\sigma^{lim} \times BR \times A}, \tag{1.23}$$

donde σ^{NF} es la sección eficaz de NF, y $\sigma^{lim} \times BR \times A$ es el límite experimental al 95 % C.L. esperado en el canal dado. Observar que para obtener una tasa genuina, los cortes aplicados a nivel partónico en el numerador deben coincidir con los cortes proporcionados por los resultados experimentales en el denominador luego de su correspondiente despliegue a nivel partónico. Observar también que al utilizar estos resultados experimentales, asumimos modelos de NF cuya dinámica, lluvia y hadronización no tienen diferencias significativas con los modelos utilizados en el análisis experimental. Esto sucede en general en los modelos de NF específicos presentados en esta tesis, sin embargo, podrían existir modelos de NF donde esto no fuese válido. En tal caso, la fuerza S debe calcularse analizando los límites en el estado final al reproducir la misma selección y los cortes a nivel de partícula o detector que el análisis experimental correspondiente.

A pesar del complejo compromiso entre la relación de ramificación teórica esperada y la limpieza de la señal experimental codificada en su definición, la fuerza S tiene una interpretación simple. Si para un canal dado vale que $S > 1$ para un punto determinado en el espacio de parámetros, entonces ese punto está excluído experimentalmente. Pero si $S < 1$ para todos los canales, el punto no solo no se excluye, sino que también se espera que el canal que tenga el S más grande sea el más sensible para la exclusión u observación de la partícula buscada.

Idealmente, para este análisis comparativo entre todos los posibles estados finales de una partícula, se espera que para una energía dada las mediciones experimentales para cada canal tengan la misma luminosidad, pero no siempre es así. Sin embargo, estas luminosidades tienden a estar casi siempre dentro del mismo orden de magnitud, por lo que asumiendo un régimen de incertidumbre estadística, la sensibilidad experimental se puede reescalar con la raíz cuadrada del cociente de las luminosidades [52].

$$\sigma^{(2)}_{lim} = \frac{\sigma^{(1)}_{lim}}{\sqrt{L_2/L_1}} \tag{1.24}$$

CHAPTER 2

INTRODUCTION

Since the Standard Model (SM) was coined 50 years ago, searches for New Physics (NP) were influenced by the yearn of a complete theory, where a complete theory means that in addition of solving many observational problems it also addresses theoretical issues such as ultraviolet (UV) divergences and the hierarchy problem, among others. Given the negative results in these searches insofar, it could be valuable to begin considering that at the next level of the energy frontier the NP may be hopefully seen only as a partial theory with many patches to be understood and solved in the forthcoming years. Pushing the possibility of a complete theory, as for instance Supersymmetry [1, 2] or Extra Dimensions [3] among others, for a higher energy level. This new scenario may lead to more phenomenological works.

All along this thesis we study simplified phenomenology theories and models and propose observables and ways of measuring them enhancing the features that distinguishes the new physics from the Standard Model, based on the idea that a new particle could be actually quite coupled to the top and even the bottom quarks. We found the third generation of quarks to be a nice doorway to the new physics world.

In the present section, we will review theoretical as well as experimental features of the heavy quarks related to possible clues of new physics. From the basic characteristics of the top quark and hints of new physics in LHC searches of heavy quarks final states, to the way these quarks mix with the others and the special features that appear. In the next chapter, we will study a simplified phenomenologic approach to a well known theory beyond the Standard Model, in which new bosons couple strongly to the top quark.

Next sections provide phenomenologic studies and searches for New Physics using previously results from the LHC, including a generic search analysis for new particles and proposal for a direct measurement of a parameter related to the top quark.

2.1 Why the third generation of quarks?

The bottom and top quarks are also known as the heavy quarks. They have the largest masses of all quarks and the top is actually the heaviest particle of the Standard Model. Its huge mass close to the EWSB scale implies a large coupling to the Higgs boson, what makes the top a privileged intermediate to the Higgs sector. This quark has also a lifetime so short that it decays before hadronization, what allows us to study its properties which are preserved in the decaying and transferred to the daughters particles. Due to these special features, the top quark plays an essential role when looking for New Physics. There are several models that predict the existence of new particles coupled to the top. This is usually because of the same reason it has a large coupling to the Higgs boson: its large mass provides a large Yukawa, and one can think of hidden particles in the Higgs sector with the same characteristics. In Sect. 3 we study one of those theories. Studying the top quark could give us some help to find new hidden particles.

The experimental study of final states with heavy flavors has always been an interesting sector where to search for deviations from the Standard Model (SM), and in particular at LHC, Tevatron and LEP this has been specially true for the third generation of quarks. The study of pairs of third generation of quarks has given SM-expected results for $t\bar{t}$ at the LHC [4, 5] and Tevatron [6], whereas $b\bar{b}$ is a difficult process to study in these hadronic machines because of the huge background and very few clean results are available at present time [7, 8]. However, at LEP the final state $b\bar{b}$ left one of its larger deviations in what is known as the LEP b-anomaly [9].

The study of final states with three or more third generation quarks at the LHC is a developing field which is generating an important set of new results lately. The four-bottom final state is usually studied in searches for heavy Higgs which are produced through $b\bar{b}$ fusion and decays to $b\bar{b}$ [10–12]. However, this final state has the difficulty of being hidden in QCD background as well as being hard to tag the bottoms. The four-top final state is many times analyzed as possible signatures of heavy resonances decaying to $t\bar{t}$ [13], and also lately in looking for the SM four-top process [14, 15], which may also hide non-resonant NP [16]. Notice, however, that four-top is a very heavy final state and usually its cross-section has important suppressions. Four-top is also a very populated final state which may yield difficulties in its reconstruction. The $t\bar{t}b\bar{b}$ [17, 18] final state is the mid-term between the previous two final states and is very interesting because most of the previously mentioned difficulties are reduced meanwhile still captures the attraction of NP effects.

2.1.1 Possible hints

Most of the mentioned final states have slight excesses which become larger as the number of b-tags increases. For instance –and not being exhaustive–, in ATLAS four-top search in Ref. [19], the comparison of prediction to data in all control and signal regions yields a systematic increasing deviation as the number of required b-tags goes from 2 to 4. In ATLAS $t\bar{t}b\bar{b}$ first study

[20], the measured fiducial cross-section was 2σ beyond the SM prediction. Later results [18] including more data and some re-analysis reduced this excess to 1.2σ. Ref. [18] dedicates a full section to discuss possible different tuning of the Montecarlo, mainly on the $g \to b\bar{b}$ splitting kernels whose tuning has an important effect on the data to prediction agreement. CMS study on $t\bar{t}b\bar{b}$ was from the beginning addressed to reduce the impact of eventual Montecarlo issues due to the b-pair in the final state. In their first work [17] they presented a comparison between $\sigma(t\bar{t}b\bar{b})$ and $\sigma(t\bar{t}jj)$ with a 1σ excess. In their second article [21] they have presented relevant differential measurements in kinematic variables such as $\Delta R_{b\bar{b}}$ and $m_{b\bar{b}}$, in which a resonant signal can be distinguished using side-band measurements. Interestingly, both measurements have $\sim 1.5\sigma$ excesses in the back-to-back bin in $\Delta R_{b\bar{b}}$ and in the large mass $m_{b\bar{b}} > 170$ GeV bin. These measurements are also performed in the $t\bar{t}jj$ final state under similar conditions and no excess is found neither in ΔR_{jj} nor m_{jj}. It is also interesting to note that they need to apply normalization factors of 2 and 4 for all the predictions on leading and subleading additional b jet quantities to reach agreement with data, reflecting some issue at least in the Montecarlo. In the last few months preliminary $t\bar{t}b\bar{b}$ results from ATLAS [22] and CMS [23] appeared on the 13 TeV data. ATLAS results, before fitting the Montecarlo to data, show again an excess which increases with the number of b tags. This excess disappears after performing a fitting to data in the background-only hypothesis. CMS [23] total ratio $\sigma(t\bar{t}b\bar{b})/\sigma(t\bar{t}jj)$ yields a 1.5σ excess compared to SM prediction. However, in this thesis we will restrict the main analysis to published data on $t\bar{t}b\bar{b}$ [17, 18], which corresponds to 7 and 8 TeV data. There are also many theoretical works which have addressed the $t\bar{t}b\bar{b}$ [24–29] and the $t\bar{t}t\bar{t}$ [30, 31] final states. More recent results published on 2020 on four tops and $t\bar{t}b\bar{b}$ searches do maintain some of the results in the previous experiments. On the work published by ATLAS [32] where they studied four tops final states at 13 TeV, it can still be found deviations of about $\sim 2\sigma$ specially when a large amount of b jets are tagged. The normalization factors are still present. On the other hand, the work published by CMS [33] also presents excesses and deviations. It is said on the paper that the cross section ratio measured is larger than the simulated prediction by a factor of 1.3, having a significance of 3σ, in the dilepton channel (see 2.1). It is mentioned that a larger cross section ratio with respect to the prediction by a factor of 1.8 with 2σ was also present on a previous measurement made by CMS at 13 TeV.

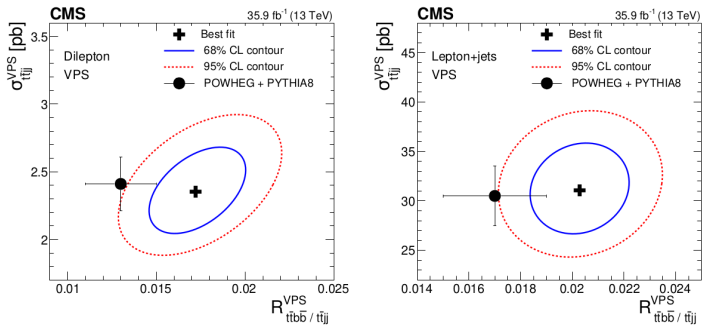

Figure 2.1: Simultaneous fit for the $R_{ttbb/ttjj}$ and σ_{ttjj} in the visible phase space (marked with a cross). The point represents the prediction. Plots extracted from the work published by CMS [33].

Although the results mentioned here are merely excesses and we are not suggesting that they represent an actual discovery, we consider them as an initial point and inspiration to study ways to find and measure hints that could be associated to the existence of new particles.

2.2 Simplified NP models

Because no real sign of a new particles has been found yet, we decided to perform a phenomenologic study in which we use simplified models of NP where a new particle couples to the third generation of quarks through generic couplings. These models should present the basic features of such a particle without the theoretical difficulties of a complete theory. We present four models with the new particle being a scalar, a pseudo-scalar, a vector, and a graviton. We restrict our study to electrically neutral NP, although charged NP could also provide interesting NP models. Depending on the magnitude of the parameters in the model, this kind of NP would be mainly manifest in final states as $t\bar{t}b\bar{b}$, $t\bar{t}t\bar{t}$, $b\bar{b}b\bar{b}$, $t\bar{t}$ and $b\bar{b}$. In particular, the relative sensitivity of these final states to the NP will change drastically depending if the new particle mass is heavier or lighter than $2m_t$.

To keep the discussion as general as possible, we make no assumptions in the underlying model, we focus on the phenomenology and present possible simplified NP Lagrangians which couple to top and bottom quarks.

2.2.1 Scalar ϕ

The case of a massive scalar field that couples exclusively to top and bottom is one of the simplest NP models. However, a scalar field has potential issues, since involves interactions with Left and Right quarks, which yields a vertex with a non-trivial SM EW gauge structure. Nevertheless, this kind of interacting terms can be achieved in a variety of models without stronger complications, since the effective vertex can be understood, for instance, as coming from higher dimensional

operators or from a spontaneously breaking of the symmetry. The parameters of such a model can be in general matched to UV complete models such as some of the many available Two Higgs Doublet Model (2HDM) (See for instance, and not being exhaustive, Refs. [34–36]). The main issue here may be how independent can be the top and bottom couplings. In a 2HDM this is addressed with the free parameter $\tan\beta$, although it could be the case that for given arbitrary values of the top and bottom couplings this particular UV completion scenario may be constrained in the parameter space from other experimental limits placed within the specific 2HDM case. In any case, we stress that the analysis in this work is focused in the phenomenological NP Lagrangians, rather than in UV complete theories. Another problem with this model is that for large couplings to bottom quarks and small masses, it could enter into conflict with LEP precision observables.

For the scalar case we study the following simplified Lagrangian

$$L_\phi^{tree} = c_{\phi t}\,\bar{t}_L \phi t_R + c_{\phi b}\,\bar{b}_L \phi b_R + h.c. \tag{2.1}$$

A one-loop effective coupling to gluons $gg\phi$ can be added to the Lagrangian due to a top and bottom loop. The extra Lagrangian in this case reads

$$L_\phi^{loop} = \frac{\alpha_s}{12\sqrt{2}\pi}\left[\frac{c_{\phi t}}{m_t}F(z_t) + \frac{c_{\phi b}}{m_b}F(z_b)\right]\phi G^a_{\mu\nu}G_a^{\mu\nu} \tag{2.2}$$

where

$$z_{t,b} = (2m_{t,b}/M)^2$$

with M the resonance mass (in this case $M = M_\phi$), and $F(z)$ is the loop function that can be found in the Appendix.

The NP interacting effective Lagrangian is therefore

$$L_\phi = L_\phi^{tree} + L_\phi^{loop}. \tag{2.3}$$

2.2.2 Pseudoscalar A

The pseudoscalar case, which could also be understood as a member of a 2HDM, has the following Lagrangian

$$L_A^{tree} = c_{At}\,\bar{t}_L A i\gamma^5 t_R + c_{Ab}\,\bar{b}_L A i\gamma^5 b_R + h.c. \tag{2.4}$$

The one-loop effective Lagrangian that couples ggA reads

$$L_A^{loop} = -\frac{\alpha_s}{8\sqrt{2}\pi}\left[\frac{c_{At}}{m_t}H(z_t) + \frac{c_{Ab}}{m_b}H(z_b)\right] A\, G^a_{\mu\nu}\tilde{G}_a^{\mu\nu}, \tag{2.5}$$

where the loop function $H(z)$ can be found in the Appendix. The full pseudoscalar Lagrangian reads $L_A = L_A^{tree} + L_A^{loop}$.

2.2.3 CP-violating scalar φ

The last case of spin one is a CP-violating scalar φ whose tree level Lagrangian reads

$$L_{\varphi}^{tree} = c_{\varphi t}\,\bar{t}_R\varphi(1+i\gamma^5)t_L + c_{\varphi b}\,\bar{b}_R\varphi(1+i\gamma^5)b_L + h.c. \tag{2.6}$$

The loop-level Lagrangian reads as the corresponding addition of Lagrangians in Eqs. 2.2 and 2.5 after replacing $\phi,\ A \to \varphi$.

2.2.4 Vector Z'

A spin one, colorless and neutral Z' with mass $M_{Z'}$ which couples exclusively to t and b ends up being the model with less potential issues. To keep the top and bottom couplings as free parameters independently of the SM EW gauge group, we keep only couplings to right handed quarks. This also helps to avoid conflicts with LEP precision measurements. The interaction of such a Z' with the SM particles reads

$$L_{Z'} = -c_{Z't}\,\bar{Z}'_{\mu}t_R\gamma^{\mu}t_R - c_{Z'b}\,Z'_{\mu}\bar{b}_R\gamma^{\mu}b_R. \tag{2.7}$$

Since Z' has spin one, it cannot couple at any order to a gg initial state.

2.2.5 Axial vector $\tilde{Z}'$

As an additional spin one case, we also study a vector whose coupling is pure axial and couples to the full fermion:

$$L_{\tilde{Z}'} = -c_{\tilde{Z}'t}\,\tilde{Z}'_{\mu}\bar{t}\gamma^5\gamma^{\mu}t - c_{\tilde{Z}'b}\,\tilde{Z}'_{\mu}\bar{b}\gamma^5\gamma^{\mu}b. \tag{2.8}$$

This particle cannot either couple to a gg initial state.

2.2.6 Graviton G

We consider an effective Lagrangian for a spin-2 graviton with field $\hat{G}_{\mu\nu}$. The tree-level interaction Lagrangian reads

$$L_G^{tree} = -\frac{i}{2\Lambda}\hat{G}^{\mu\nu}\left[c_{Gt}\left(\bar{t}_R\gamma_{\mu}\overleftrightarrow{D}_{\nu}t_R - \eta_{\mu\nu}\bar{t}_R\gamma^{\rho}\overleftrightarrow{D}_{\rho}t_R\right) + c_{Gb}\left(\bar{b}_R\gamma_{\mu}\overleftrightarrow{D}_{\nu}b_R - \eta_{\mu\nu}\bar{b}_R\gamma^{\rho}\overleftrightarrow{D}_{\rho}b_R\right)\right], \tag{2.9}$$

where $\bar{f}\gamma_{\mu}\overleftrightarrow{D}_{\nu}f = \bar{f}\gamma_{\mu}D_{\nu}f - D_{\nu}\bar{f}\gamma_{\mu}f$. For the purposes of this work, we only use the partial derivative term in the covariant derivative, since we neglect the 4-particle interaction contained in the other terms.

Contrary to the previous NP models, the spin-2 Lagrangian needs dimensional couplings, and this is why the dimensional constant Λ in the denominator. Along the remaining of this thesis we set

$$\Lambda = 1 \text{ TeV}.$$

This arbitrary choice matches the cross-sections $\sigma(b\bar{b} \to G) = \sigma(b\bar{b} \to \phi)$ for the same numerical values of the couplings $c_{\phi b} = c_{Xb} = 1$ and $M_G = M_\phi = 300$ GeV. Of course that this agreement is lost as the numerical values of the couplings or the mass of the resonance are modified, since both models have a different dynamic. This choice is just to have a contact point for the spin-2 NP model whose couplings are not dimensionless.

The one-loop effective Lagrangian that couples ggG reads

$$L_G^{loop} = -\frac{\alpha_s}{12\pi\Lambda}\left[c_{Gt}A_G(z_t,\mu_0) + c_{Gb}A_G(z_b,\mu_0)\right]\hat{G}_{\mu\nu}\left(\frac{\eta^{\mu\nu}}{4}G^a_{\rho\sigma}G^{\rho\sigma}_a - G^{a\mu}_\rho G^{\nu\rho}_a\right). \tag{2.10}$$

Here μ_0 is the renormalization scale and the loop function $A_G(z,\mu_0)$ can be found in the Appendix. The full spin-2 Lagrangian reads $L_G = L_G^{tree} + L_G^{loop}$.

2.3 Quark Mixing

Another interesting feature of the top quark is its mixing to light quarks. These are parameters which are currently known with a high percentage of uncertainty and they make a good place when looking for new couplings. In this section we made a short review of the quarks mixing.

Quarks, just like leptons, interacts electromagnetically through the weak force. So we can model the charged current just like

$$J^\mu_q = \overline{u}_u\gamma^\mu\frac{1}{2}(1-\gamma^5)u_d, \tag{2.11}$$

where u is the quark field. This current has a vectorial-axial structure, since its coupling involves a scalar and the γ^5 matrix. Therefore, it can couple only left handed u and d or right handed $\overline{u}$ and $\overline{d}$, and always quarks belonging to the same family. This current may couple to bosons giving as a result interactions just like in Fig. 2.2.

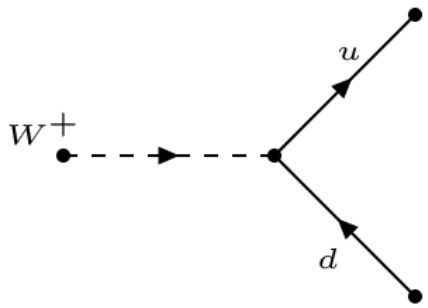

Figure 2.2: Feynman diagram for the quarks current coupled to the W^+ weak boson.

This worked fine for the first generation of quarks but in time physicists realized it could not explained the observed interactions with heavier quarks, just like the decay $K^+ \to \mu^+\nu_\mu$ with K^+

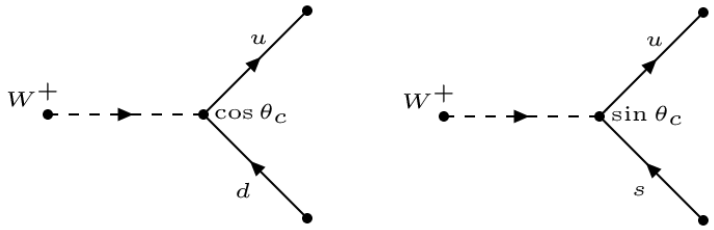

Figure 2.3: Feynman diagrams for the W^+ boson decaying to quarks processes. The one in the left is favored by the mixing, with a coupling proportional to $\cos\theta_c$, while the one in the right is suppressed because of the mixing, with coupling proportional to $\sin\theta_c$.

made of u and $\bar{s}$ quarks. To avoid the introduction of new coupling specialized on each interaction, Cabibbo proposed in 1963 [37] to rotate the quarks with a mixing angle, an arbitrary parameter known as the Cabibbo angle θ_c. In this manner, the doublets

$$\begin{pmatrix} u \\ d \end{pmatrix} \quad , \quad \begin{pmatrix} c \\ s \end{pmatrix} \tag{2.12}$$

in the interactions are changed into the new doublets

$$\begin{pmatrix} u \\ d' \end{pmatrix} \quad , \quad \begin{pmatrix} c \\ s' \end{pmatrix} \tag{2.13}$$

which are defined as

$$d' = d\cos\theta_c + s\sin\theta_c, \tag{2.14}$$
$$s' = -d\sin\theta_c + s\sin\theta_c. \tag{2.15}$$

The quark strange s introduces the quantum number strangeness S to the process. If there is a change of flavor in a decay, where a strange is created or destroyed, there is a change in the strangeness which can be determined. Cabibbo introduced his rotation in order to explain this phenomenom, since it allowed flavor changes, with $\Delta S = 1$. The experiments showed that transitions with $\Delta S = 1$ where suppressed by a factor of 20 with respect with transitions without flavor changing [38]. That gave as a result that the Cabibbo angle should be $\theta_c \approx 13°$. As a result, there are some favored transitions and some suppressed ones, see Figs. 2.3.

The current is written then as

$$J^\mu = (\bar{u} \quad \bar{c}) \frac{\gamma^\mu(1-\gamma^5)}{2} V \begin{pmatrix} d \\ s \end{pmatrix} \tag{2.16}$$

where V is the rotation matrix defined by

$$\begin{pmatrix} \cos\theta_c & \sin\theta_c \\ -\sin\theta_c & \cos\theta_c \end{pmatrix}. \tag{2.17}$$

The original d and s quarks are the so called mass states, or physical, because they are the quarks that appear in the mass term inside the lagrangian. The new states d' and s' are orthogonal combinations of the former and they appear in the interactions term. They are formally given by the Cabibbo-GIM mechanism

$$\begin{pmatrix} d' \\ s' \end{pmatrix} = \begin{pmatrix} \cos\theta_c & \sin\theta_c \\ -\sin\theta_c & \cos\theta_c \end{pmatrix} \begin{pmatrix} d \\ s \end{pmatrix} \tag{2.18}$$

This mechanism allows the change in strangeness in the final state but assures that there is no change in the electric charge of the quarks. Kobayashi and Maskawa generalized it to the three generations of quarks years later [39], where V is now a 3×3 matrix and the new current is given by

$$J^\mu = (\overline{u} \quad \overline{c}\overline{t}) \frac{\gamma^\mu(1-\gamma^5)}{2} V_{CKM} \begin{pmatrix} d \\ s \\ b \end{pmatrix} \tag{2.19}$$

where V_{CKM} is the Cabibbo-Kobayashi-Maskawa matrix. It can be parameterized by three mixing angles (equal to the Cabibbo angle) and a CP-violating KM phase. Each of the coefficients V_{ij} represents the mixing between the quark i and the quark j and so far we know them experimentally as

$$V_{CKM} = \begin{pmatrix} V_{ud} & V_{us} & V_{ub} \\ V_{cd} & V_{cs} & V_{cb} \\ V_{td} & V_{ts} & V_{tb} \end{pmatrix} \approx \begin{pmatrix} 0.974 & 0.225 & 0.004 \\ 0.224 & 0.974 & 0.042 \\ 0.009 & 0.041 & 0.999 \end{pmatrix}. \tag{2.20}$$

It can be seen that the elements in the diagonal are very close to unity while the others are much smaller. This is because, as already said, there are some transitions which are favored. They correspond to the interactions between quarks of the same generation, as if there were no mixing between them. The interactions due to the Cabibbo mixing are suppressed. From the unitarity of the matrix, we can derive conditions upon the elements, $\sum_i V_{ij} V_{ik}^* = \delta_{jk}$ and $\sum_j V_{ij} V_{kj}^* = \delta_{ik}$. These conditions give six vanishing combinations which can be interpreted graphically in terms of triangles in a complex plane.

The entries in the CKM matrix governing flavor transitions among quarks are fundamental parameters of the standard model (SM). As such they warrant intense experimental scrutiny. Currently the first two rows of the CKM are already being probed directly with ever improving precision using decays of nuclei, kaons, charmed mesons and B-hadrons [40]. On the other hand, few direct experimental handles exist on the third row of the CKM. In this thesis we will study

indirect ways of measuring V_{td} and therefore here we are only interested in the V_{tq} elements of the CKM matrix.

2.3.1 Measuring of the $|V_{tq}|$ elements

The SM predictions for V_{tq} matrix elements, with $q = d, s, b$ are currently derived from CKM unitarity considerations, as well as measurements of radiative decays and oscillations of B-mesons, where V_{tq} enter in loops involving virtual top quarks. A recent global CKM fit yields [41]

$$|V_{tb}^{SM}| = 1 - 8.81^{+0.12}_{-0.24} \times 10^{-3}, \quad |V_{ts}^{SM}| = 41.08^{+3.0}_{-5.7} \times 10^{-3}, \quad |V_{td}^{SM}| = 8.575^{+0.076}_{-0.098} \times 10^{-3}. \quad (2.21)$$

Measurements of b-jet fractions in top decays $t \to Wj$ currently put a bound on [42]

$$\frac{B(t \to bW)}{\sum_{q=d,s,b} B(t \to qW)} > 0.955 \ @ \ 95\% \ C.L., \quad (2.22)$$

which can be interpreted as $\sqrt{|V_{td}|^2 + |V_{ts}|^2} < 0.217 |V_{tb}|$. In addition, precise measurements of t-channel single top production and its charge asymmetry at the LHC [43–45] when compared with the accurate theoretical predictions [46–49] can be interpreted as measurements of $|V_{tq}|$. A recent ATLAS analysis neglecting $|V_{td,ts}|$ effects yields $|V_{tb}| = 1.07 \pm 0.09$ [43]. While such measurements are in principle also able to probe the $|V_{ts}|$ and $|V_{td}|$ matrix elements [50] [51], they are intrinsically limited by the overwhelming backgrounds and associated statistical and systematic uncertainties. Consequently, especially in the case of $|V_{td}|$ they are not expected to come even close to the magnitude of the SM predictions.

2.4 The strength

When someone is studying models of new physics, it is very frequent to analyze different final states in order to find something that is different from the SM. One possibility in order to achieve this goal is to design search strategies for each one of the final states, and compute the exclusion/discovery reach for each final state, to conclude which channel is the most sensitive and which luminosity is required to exclude/discover each point in parameter space.

In this thesis we propose to consider a second and more practical path: to use the already available search strategies used by the experimentalists whose sensitivity comes summarized in the 95% C.L. limits on the cross-section (σ) times acceptance (A) times branching ratios (BR) of an hypothetical new particle. Using these results, one can compute in a given channel the ratio of the expected NP $\sigma \times A \times BR$ to the corresponding expected limit in those search strategies. This ratio is the strength of the given channel expressed in such a way that it can be directly compared to the same ratio in other channels. That is, they are in the same units of corresponding sensitivity. More precisely, we define the strength of a given final state as

$$S = \frac{\sigma^{NP} \times BR \times A}{\sigma^{lim} \times BR \times A}, \quad (2.23)$$

where σ^{NP} is the NP cross-section, and $\sigma^{lim} \times BR \times A$ is the 95%C.L. experimental limit expected in the given channel. Observe that in order to get a genuine rate, the cuts applied at parton level in the numerator should agree with the cuts provided by the experimental results in the denominator after their corresponding unfolding to parton level. Also notice that in using the results unfolded to parton level by experimentalists, we assume NP models whose dynamics, showering and hadronization do not have significant differences to the one assumed in the experimental analysis. This is the case in general for the specific NP models presented in this work, however there could exist NP models where this would not be valid. In such a case, the strength S should be computed by analyzing the limits in the final state by reproducing the same selection and cuts at the particle or detector level as the corresponding experimental analysis.

Despite the complex compromise between the expected theoretical branching ratio and the cleanliness of the experimental signal coded in its definition, the strength S has a simple interpretation. If for a given channel $S > 1$ for a given point in the parameter space, the point is experimentally excluded. But if $S < 1$ for all channels, the point is not only not excluded but also the one with the largest S is expected to be the most sensitive channel for the exclusion or observation of the particle being sought.

Ideally, for this comparative analysis between all possible final states for a particle, it is expected that for a given energy the experimental measurements for each channel will be at the same luminosity, but this is not always the case. However, these luminosities tend to be almost within the same order of magnitude, so assuming a statistical uncertainty regime, the experimental sensitivity can be rescaled with the square root of the ratio of the luminosities [52].

$$\sigma^{(2)}_{lim} = \frac{\sigma^{(1)}_{lim}}{\sqrt{L_2/L_1}} \tag{2.24}$$

CHAPTER 3

A WARPED COMPOSITE THEORY

In this chapter we study the phenomenology of a warped extra dimension or composite model. We follow the simplified framework in the paper [53] by Contino as a partial compositeness four dimensional model. This model includes, beside the ones in the SM, new fermions and bosons with masses around the TeV scale. The composite sector contains vector excitations ρ_μ which respect a $SU(3)_C \otimes SU(2)_L \otimes SU(2)_R \otimes U(1)_X$ symmetry, fermions χ and $\tilde{\chi}$ and the Higgs field H. Our assumption that the composite sector corresponds to a strongly interacting theory, but still perturbative, is translated in assuming g_* , $Y_* \sim 1-4$. We follow the notation in Ref. [53].

3.1 Introduction

The theory, a simplified model of that of Randall Sundrum, has two sectors: the elementary (with all the SM particles except for the Higgs boson) and the composite (the new one). Following the notation by Contino [53], the SM electroweak doublet fermions are

$$\psi_L \equiv \{q_{Li} = (u_{Li}, d_{Li}), \ell_{Li} = (\nu_{Li}, e_{Li})\}\,, \qquad i = 1,2,3\,, \tag{3.1}$$

while the SM singlet fermions are denoted by

$$\tilde{\psi}_R \equiv \{u_{Ri}, d_{Ri}, \nu_{Ri}, e_{Ri}\}\,. \tag{3.2}$$

On the other side we have the SM bosons,

$$A_\mu \equiv \{G_\mu, W_\mu, B_\mu\}\,. \tag{3.3}$$

with the associated gauge couplings $g_{el\,1}$, $g_{el\,2}$, $g_{el\,3}$, which are approximately equal to the SM gauge couplings g_1, g_2, g_3. With these fields, we can write the elementary Lagrangian which

contains the gauge interactions and dynamics

$$L_{elementary} = -\frac{1}{4}F_{\mu\nu}^2 + \bar{\psi}_L i\not{D}\psi_L + \bar{\tilde{\psi}}_R i\not{D}\tilde{\psi}_R\,, \tag{3.4}$$

where the covariant derivative is $D_\mu = \partial_\mu - ig_{el}A_\mu$ and it must be understanded as the sum of all gauge fields with their respective generators.

Next we have the composite sector, that is in charge of providing the SM fields a composite component. It contains composite vector excitations ρ_μ which respect a $[SU(3)_c \otimes SU(2)_L \otimes SU(2)_R \otimes U(1)_X]$ symmetry, and composite fermions $\tilde{\chi}^u \equiv \{\tilde{U},\tilde{N}\}$, $\tilde{\chi}^d \equiv \{\tilde{D},\tilde{E}\}$ and

$$\chi \equiv \{Q_i = (U_i, D_i), L_i = (N_i, E_i)\}\,, \qquad i = 1,2,3\,. \tag{3.5}$$

So that the lagrangian is

$$\begin{aligned} L_{composite} = &-\frac{1}{4}\rho_{\mu\nu}^2 + \frac{M_*^2}{2}\rho_\mu^2 + |D_\mu H|^2 - V(H) \\ &+ \bar{\chi}(i\not{D} - m)\chi + \bar{\tilde{\chi}}(i\not{D} - \tilde{m})\tilde{\chi} - \bar{\chi}\left(Y_{*u}\tilde{H}\tilde{\chi}^u + Y_{*d}H\tilde{\chi}^d\right) + \text{h.c.}\,, \end{aligned} \tag{3.6}$$

where the composite covariant derivative is given by $D_\mu = \partial_\mu - g_*(\rho_\mu^* + \tilde{\rho})$. The Yukawa couplings break the gauge invariance, but with composite couplings large still on the perturbative range (this is, $g_*, Y_* \ll 4\pi$), the breaking is negligible for the purposes of this work. We will work with $2 < g_* < 4$. The SM Higgs is a composite field. The bidoublet transformation under $[(2)_L \otimes SU(2)_R]^{comp}$ are given by

$$(\tilde{H}, H) \to L(\tilde{H}, H)R^\dagger\,, \tag{3.7}$$

where $\tilde{H} = i\sigma^2 H^*$. The Higgs potential has the usual form

$$V(H) \equiv -\mu_H^2|H|^2 + \lambda_H|H|^4\,. \tag{3.8}$$

The field content and quantum numbers are given in table 3.1.

We divide the vector fields into those that will mix with the elementary gauge bosons, ρ_μ^* and those that will not, $\tilde{\rho}_\mu$,

$$\rho_\mu = \{\rho_\mu^*, \tilde{\rho}_\mu\}\,. \tag{3.9}$$

Originally, they were

$$\rho_\mu^* = \{G_\mu^*, W_\mu^*\}, \qquad \tilde{\rho}_\mu = \{\tilde{G}_\mu, \tilde{W}_\mu, X\}\,. \tag{3.10}$$

In the next section we will perform a rotation over $\tilde{W}_3$ and X, what will generate the new fields B and B^*.

Under the global symmetry $[SU(3) \otimes SU(2)_L \otimes U(1)_Y]$, ρ_μ^* transform as an adjoint. On the other side, $\tilde{\rho}_\mu$ form an orthogonal combination:

$$\rho_\mu^* = \{G_\mu^*, W_\mu^*, B_\mu^*\}, \qquad \tilde{\rho}_\mu = \left\{\tilde{W}_\mu^\pm \equiv \frac{\tilde{W}_1 \mp i\,\tilde{W}_2}{\sqrt{2}}, \tilde{B}_\mu\right\}. \tag{3.11}$$

		$SU(3)_c$	$SU(2)_L$	$SU(2)_R$	$U(1)_X$
ρ_μ		Gauge Fields			
$(\tilde{H},H)$		1	2	2	0
χ	Q	3	2	1	$\frac{1}{6}\cdot\sqrt{\frac{3}{2}}$
	L	1	2	1	$\left(-\frac{1}{2}\right)\cdot\sqrt{\frac{3}{2}}$
$\tilde{\chi}$	$\tilde{U}$	3	1	1	$\frac{2}{3}\cdot\sqrt{\frac{3}{2}}$
	$\tilde{D}$	3	1	1	$\left(-\frac{1}{3}\right)\cdot\sqrt{\frac{3}{2}}$
	$\tilde{N}$	1	1	1	0
	$\tilde{E}$	1	1	1	$(-1)\cdot\sqrt{\frac{3}{2}}$

Table 3.1: Fields and their quantum numbers.

These are the fields that appear after the rotations performed over the fields (see Sect.3.2 for details). The fields $\tilde{W}^1,\tilde{W}^2$ are associated to the $SU(2)_R$ generators T^{1R},T^{2R}, while B^* and $\tilde{B}$, being rotated fields, are associated to the mix of the third $SU(2)_R$ component and a hypercharge, $T_{B^*}\equiv Y_{GUT}=(T^{3R}+\xi T_X)/\sqrt{1+\xi^2}$, $T_{\tilde{B}}=(\xi T^{3R}-T_X)/\sqrt{1+\xi^2}$. The hypercharge in SO(10) is chosen to be the generator of the preserved $U(1)$ by setting $\xi=\sqrt{2/3}$, so that $Y_{GUT}=\sqrt{3/5}Y$.

The composite sector appears when we couple fermions and bosons to the elementary ones in a mass mixing term,

$$L_{mixing}=-M_*^2\frac{g_{el}}{g_*}A_\mu\rho_\mu^*+\frac{M_*^2}{2}\left(\frac{g_{el}}{g_*}A_\mu\right)^2+(\bar{\psi}_L\Delta\chi_R+\bar{\tilde{\psi}}_R\tilde{\Delta}\tilde{\chi}_L+h.c.). \tag{3.12}$$

Δ and $\tilde{\Delta}$ are responsible for the mixing, which is null if they are zero.

3.1.1 Fermions diagonalization

From Eq. 3.6 we have $-\bar{\chi}m\chi-\bar{\tilde{\chi}}\tilde{m}\tilde{\chi}$ and from Eq. 3.12 $\bar{\psi}_L\Delta\chi_R+\bar{\tilde{\psi}}_R\tilde{\Delta}\tilde{\chi}_L+h.c.$, which are all the terms we need in order to perform a diagonization. Taking $\chi=\chi_L+\chi_R$ (with $\bar{\chi}=\bar{\chi}_L+\bar{\chi}_R$) and the same for $\tilde{\chi}$, we can write both terms as

$$L_{fermix}=\bar{v}_L M_{LR}v_R+\bar{v}_R M_{RL}v_L, \tag{3.13}$$

with $v_i=(\psi_i,\chi_i,\tilde{\chi}_i)$, $i=L,R$, $M_{LR}=\begin{pmatrix}0 & \Delta & 0\\ 0 & -m & 0\\ \tilde{\Delta} & 0 & -\tilde{m}\end{pmatrix}$, and $M_{RL}=M_{LR}^T$. We need to have a system written as $\bar{v}Mv$ with M a diagonalizable matrix in order to proceed. So that we implement a little

trick. Let us write v as

$$\begin{aligned} v_L &= C_L v_L^{NB}, \\ v_R &= C_R v_R^{NB}, \end{aligned} \tag{3.14}$$

where C is a new matrix and v_i^{NB} is v written is this new base. Following, we have

$$\begin{aligned} L_{fermix} &= \bar{v}_L^{NB} C_L^T M_{LR} C_R v_R^{NB} \\ &+ \bar{v}_R^{NB} C_R^T M_{RL} C_L v_L^{NB}. \end{aligned} \tag{3.15}$$

We need $C_L^T M_{LR} C_R$ and its transposed to be diagonal, say M_D. Let's see this is actually true. Suppose

$$C_L^T M_{LR} C_R = M_D, \tag{3.16}$$
$$C_R^T M_{RL} C_L = M_D, \tag{3.17}$$

and let's multiply both equations, once from the left and once from the right. Using that C is unitary (its conjugate equal to its inverse) we have

$$C_L^T M_{LR} M_{RL} C_R = M_D^2, \tag{3.18}$$
$$C_R^T M_{RL} M_{LR} C_L = M_D^2, \tag{3.19}$$

which are diagonal matrix, and so, if M_D^2 is diagonal, so is M_D. If matrices C are unitary, then Eqs. 3.19 are eigenvalues and eigenvectors equations.

So now, we want to know who is M_D and C. Multiplying,

$$M_{LR} M_{RL} = \begin{pmatrix} \Delta^2 & -m\Delta & 0 \\ -m\Delta & m^2 & 0 \\ 0 & 0 & \tilde{\Delta}^2 + \tilde{m}^2 \end{pmatrix} \tag{3.20}$$

This matrix has three eigenvalues, $\lambda_0 = 0$, $\lambda_1 = \Delta^2 + m^2 \equiv m_*^2$ and $\lambda_2 = \tilde{\Delta}^2 + \tilde{m}^2 \equiv \tilde{m}_*^2$, whith their corresponding eigenvectors, $\bar{v}_0 = (1, \Delta/m, 0)$, $\bar{v}_1 = (1, -m/\Delta, 0)$ and $\bar{v}_2 = (0,0,1)$. By normalizing, we have

$$C_L = \begin{pmatrix} \frac{m}{\sqrt{\Delta^2+m^2}} & -\frac{\Delta}{\sqrt{\Delta^2+m^2}} & 0 \\ \frac{\Delta}{\sqrt{\Delta^2+m^2}} & \frac{m}{\sqrt{\Delta^2+m^2}} & 0 \\ 0 & 0 & 1 \end{pmatrix} = \begin{pmatrix} \cos(\phi_{\psi_L}) & -\sin(\phi_{\psi_L}) & 0 \\ \sin(\phi_{\psi_L}) & \cos(\phi_{\psi_L}) & 0 \\ 0 & 0 & 1 \end{pmatrix}, \tag{3.21}$$

with $\tan(\phi_{\psi_L}) = \frac{\Delta}{m}$. Remembering the inverse relation, $v_i = C_i v_i^{NB}$, we finally reach

$$\begin{pmatrix}\psi_L\\ \chi_L\end{pmatrix}=\begin{pmatrix}\cos(\phi_{\psi_L}) & -\sin(\phi_{\psi_L})\\ \sin(\phi_{\psi_L}) & \cos(\phi_{\psi_L})\end{pmatrix}\begin{pmatrix}\psi_L\\ \chi_L\end{pmatrix}_{NB}. \tag{3.22}$$

In the same way, we can get a relation for the right components, which gives

$$\begin{pmatrix}\tilde{\psi}_R\\ \tilde{\chi}_R\end{pmatrix}=\begin{pmatrix}\cos(\phi_{\tilde{\psi}_R}) & -\sin(\phi_{\tilde{\psi}_R})\\ \sin(\phi_{\tilde{\psi}_R}) & \cos(\phi_{\tilde{\psi}_R})\end{pmatrix}\begin{pmatrix}\tilde{\psi}_R\\ \tilde{\chi}_R\end{pmatrix}_{NB}, \tag{3.23}$$

with $\tan(\phi_{\psi_R})=\frac{\tilde{\Lambda}}{\tilde{m}}$.

3.1.2 Bosons diagonalization

In this section, we will take the relevant parts for the diagonalization of the bosons from 3.6 and 3.12, giving

$$L_{bosmix}=\frac{M_*^2}{2}\left(\rho_\mu^{*2}+\tilde{\rho}_\mu^2\right)-\frac{M_*^2}{2}\frac{g_{el}}{g_*}A^\mu\rho_\mu^*+\frac{M_*^2}{2}\left(\frac{g_{el}}{g_*}A_\mu\right)^2 \tag{3.24}$$

Written in a matricial way, we have

$$\left(A_\mu\rho_\mu^*\right)\begin{pmatrix}\frac{M_*^2}{2}\left(\frac{g_{el}}{g_*}\right)^2 & -\frac{M_*^2}{2}\frac{g_{el}}{g_*}\\ -\frac{M_*^2}{2}\frac{g_{el}}{g_*} & \frac{M_*^2}{2}\end{pmatrix}\begin{pmatrix}A_\mu\\ \rho_\mu^*\end{pmatrix}. \tag{3.25}$$

This diagonalization is straight forward and it gives two eigenvalues, $\lambda_0=0$ and $\lambda_1=1+\left(\frac{g_{el}}{g_*}\right)^2$, with eigenvectors $v_0=(1,\frac{g_{el}}{g_*})$ and $v_1=(-\frac{g_{el}}{g_*},1)$. The normalized basis change matrix is

$$K=\begin{pmatrix}\frac{g_*}{\sqrt{g_*^2+g_{el}^2}} & -\frac{g_{el}}{\sqrt{g_*^2+g_{el}^2}}\\ \frac{g_{el}}{\sqrt{g_*^2+g_{el}^2}} & \frac{g_*}{\sqrt{g_*^2+g_{el}^2}}\end{pmatrix}. \tag{3.26}$$

Finally, we have the new fields on the mass base

$$\begin{pmatrix}A_\mu\\ \rho_\mu^*\end{pmatrix}_{NB}=\begin{pmatrix}\cos(\theta) & -\sin(\theta)\\ \sin(\theta) & \cos(\theta)\end{pmatrix}\begin{pmatrix}A_\mu\\ \rho_\mu^*\end{pmatrix}, \tag{3.27}$$

with $\tan(\theta)=\frac{g_{el}}{g_*}$.

3.1.3 Diagonalized Lagrangian

We want an expression for the entire Lagrangian, written as a function of the mass eigenstates, before electroweak symmetry breaking (EWSB). In order to do this, we need to replace the relations obtained for the old fields as a functions of the mass eigenstates when it is explicit and also when they appear inside the covariant derivatives. Following the notation by Contino, the fields "$A_\mu,\psi_L,\tilde{\psi}_R$" are to be understood as the elementary fields before the digonalization and as the SM fields after it. The boson fields "$\rho_\mu^*,\tilde{\rho}_\mu,\chi,\tilde{\chi}$" are the composite fields before and represents the new-physics mass eigenstates after the diagonalization.

Taking into account the fermion Lagrangian, and performing the replaces given by Eqs. 3.22, 3.23 and 3.27, this last in the covariant derivatives, and using $g = g_* \sin\theta = g_{el} \cos\theta$, we arrive to

$$\begin{aligned}
L_{fermion} =& \bar{\psi}_L i\not{D}\psi_L + \bar{\chi}(i\not{D} - m_*)\chi \\
&+ \bar{\psi}_L \left[g\left(\sin^2\varphi_{\psi_L}\cot\theta - \cos^2\varphi_{\psi_L}\tan\theta\right)\rho_\mu^* + \frac{g_1}{\sin\theta_1}\sin^2\varphi_{\psi_L}\tilde{\rho}_\mu \right]\gamma^\mu\psi_L \\
&+ \bar{\psi}_L \left(g\frac{\sin\varphi_{\psi_L}\cos\varphi_{\psi_L}}{\sin\theta\cos\theta}\rho_\mu^* + \frac{g_1}{\sin\theta_1}\sin\varphi_{\psi_L}\cos\varphi_{\psi_L}\tilde{\rho}_\mu \right)\gamma^\mu\chi_L + h.c. \\
&+ \bar{\chi}_L \left[g\left(\cos^2\varphi_{\psi_L}\cot\theta - \sin^2\varphi_{\psi_L}\tan\theta\right)\rho_\mu^* + \frac{g_1}{\sin\theta_1}\cos^2\varphi_{\psi_L}\tilde{\rho}_\mu \right]\gamma^\mu\chi_L \\
&+ \bar{\chi}_R \left(g\cot\theta\,\rho_\mu^* + \frac{g_1}{\sin\theta_1}\tilde{\rho}_\mu \right)\gamma^\mu\chi_R \\
&+ \{L \leftrightarrow R\,;\, \chi \to \tilde{\chi}\,;\, \varphi_{\psi_L} \to \varphi_{\tilde{\psi}_R}\,;\, m_* \to \tilde{m}_*\}.
\end{aligned} \tag{3.28}$$

Following with the same procedure, we can replace the old fields for the mass ones in the bosons Lagrangian, which gives

$$\begin{aligned}
L_{gauge} =& -\frac{1}{4}F_{\mu\nu}^2 \\
&+ \frac{1}{2}\left(D_\mu\rho_\nu D_\nu\rho_\mu - D_\mu\rho_\nu D_\mu\rho_\nu\right) + \frac{M_{*1}^2}{2}\tilde{\rho}_\mu^2 + \frac{M_*^2}{2\cos^2\theta}\rho_\mu^{*2} + \frac{ig}{2}F_{\mu\nu}[\rho_\mu,\rho_\nu] \\
&+ 2ig\cot 2\theta D_\mu\rho_\nu^*[\rho_\mu^*,\rho_\nu^*] + \frac{ig_1}{\sin\theta_1}D_\mu\tilde{\rho}_\nu[\tilde{\rho}_\mu,\tilde{\rho}_\nu] \\
&+ ig_1\cot\theta_1 D_\mu\rho_\nu^*[\tilde{\rho}_\mu,\tilde{\rho}_\nu] + ig_1\cot\theta_1 D_\mu\tilde{\rho}_\nu\left([\rho_\mu^*,\tilde{\rho}_\nu] + [\tilde{\rho}_\mu,\rho_\nu^*]\right) \\
&+ \frac{g^2}{4}\left(\frac{\sin^4\theta}{\cos^2\theta} + \frac{\cos^4\theta}{\sin^2\theta}\right)[\rho_\mu^*,\rho_\nu^*]^2 + \frac{g_1^2}{4\sin^2\theta_1}[\tilde{\rho}_\mu,\tilde{\rho}_\nu]^2 \\
&+ \frac{g_1^2}{4}\cot^2\theta_1\left([\rho_\mu^*,\tilde{\rho}_\nu] + [\tilde{\rho}_\mu,\rho_\nu^*]\right)^2 + g_1^2\frac{\cos\theta_1}{\sin^2\theta_1}[\tilde{\rho}_\mu,\tilde{\rho}_\nu][\rho_\mu^*,\tilde{\rho}_\nu].
\end{aligned} \tag{3.29}$$

The new covariant derivative is defined by $D_\mu = \partial_\mu - igA_\mu$, where A_μ is the eigenmass state and is, again, the sum of the fields with their respective generator.

Finally, the Higgs Lagrangian is given by

$$\begin{aligned}
L_{Higgs} =& |D_\mu H|^2 - V(H) \\
&+ H^\dagger i\, g \cot\theta\, \rho^*_\mu D_\mu H + h.c. \\
&- i \frac{g_1}{2\sin\theta_1}\left(\frac{1}{\sqrt{2}}\tilde{H}^\dagger \tilde{W}^-_\mu D_\mu H + \frac{1}{\sqrt{2}} H^\dagger \tilde{W}^+_\mu D_\mu \tilde{H} - \sqrt{\frac{2}{5}} H^\dagger \tilde{B}_\mu D_\mu H\right) + h.c. \\
&- g_1 g \frac{\cot\theta}{\sin\theta_1}\left(\frac{1}{\sqrt{2}}\tilde{H}^\dagger \rho^*_\mu \tilde{W}^-_\mu H + \frac{1}{\sqrt{2}} H^\dagger \rho^*_\mu \tilde{W}^+_\mu \tilde{H} - \sqrt{\frac{2}{5}} H^\dagger \rho^*_\mu \tilde{B}_\mu H\right) \\
&+ H^\dagger \left\{\left(g\cot\theta\,\rho^*_\mu\right)^2 + \frac{g_1^2}{\sin^2\theta_1}\left(\frac{1}{2}\tilde{W}^+_\mu \tilde{W}^-_\mu + \frac{1}{10}\tilde{B}^2_\mu\right)\right\} H \\
&- \left(\sin\varphi_{\psi_L}\bar{\psi}_L + \cos\varphi_{\psi_L}\bar{\chi}_L\right)\Big[Y_{*u}\tilde{H}\Big(\sin\varphi_{\tilde{\psi}^u_R}\tilde{\psi}^u_R + \cos\varphi_{\tilde{\psi}^u_R}\tilde{\chi}^u_R\Big) \\
&\qquad + Y_{*d} H\Big(\sin\varphi_{\tilde{\psi}^d_R}\tilde{\psi}^d_R + \cos\varphi_{\tilde{\psi}^d_R}\tilde{\chi}^d_R\Big)\Big] + h.c. \\
&- \bar{\chi}_R Y_{*u}\tilde{H}\tilde{\chi}^u_L - \bar{\chi}_R Y_{*d} H \tilde{\chi}^d_L + h.c.,
\end{aligned} \tag{3.30}$$

where the covariant derivative applied to the Higgs is simply

$$D_\mu \sigma = \partial_\mu \sigma - i g_* \rho^*_\mu \sigma + i g_* \sigma \tilde{\rho}_\mu, \tag{3.31}$$

with $\sigma = (\tilde{H} H)$, a 2×2 matrix.

3.2 Rotation of the fields

In this section we describe in precision the rotations which are performed over the fields. Initially, we have three groups, the elementary bosons A, which contains the gluon fields G and the weak W, and two composite, the ρ^*, with G^* and W^* which corresponds to the same kind of symmetries than the elementary ones, and $\tilde{\rho}$, with $\tilde{G}$, $\tilde{W}$ and X, of symmetries $SU(3)$, $SU(2)_R$ and $U(1)_X$ respectively. Note that there is only one $U(1)$ field by now, later on will appear others.

As mentioned before, we will mix $\tilde{W}_3$ with X in the following manner

$$\begin{pmatrix}\tilde{W}_3 \\ X\end{pmatrix} = \begin{pmatrix}\cos(\phi) & -\sin(\phi) \\ \sin(\phi) & \cos(\phi)\end{pmatrix}\begin{pmatrix}\tilde{B} \\ B^*\end{pmatrix}, \tag{3.32}$$

with $\sin(\phi) = \frac{1}{\sqrt{1+\xi^2}} = \sqrt{\frac{3}{5}}$ and $\cos(\phi) = \frac{\xi}{\sqrt{1+\xi^2}} = \sqrt{\frac{2}{5}}$, $\xi = \sqrt{\frac{2}{3}}$. The value for ξ is chosen to normalize the Y_{GUT} generator.

3.2.1 Higgs derivative

Going back to Eq. 3.31 and writing explicitly the fields and generators, and performing the first rotation given in Eq. 3.27, we have

$$D_\mu \sigma = \partial_\mu \sigma - i g \frac{1}{2}(\bar{\sigma}\cdot\bar{W})\sigma - i g \cot(\theta)\frac{1}{2}(\bar{\sigma}\cdot\bar{W}^*)\sigma + i\frac{g}{\sin(\theta)}\frac{1}{2}\sigma(\bar{\sigma}\cdot\bar{\tilde{W}}), \tag{3.33}$$

where $\bar{\sigma} = (\sigma_1, \sigma_2, \sigma_3)$ are the Pauli matrices. Here we mixed the star bosons with the SM ones, W_1 with W_1^*, etc.

The next step is to perform the rotation over $\tilde{W}_3$, given in Eq. 3.32. Notice that X is not present in this derivative. This is due to the fact that the Higgs is not charged under $U(1)_X$. So that we have

$$D_\mu \sigma = \partial_\mu \sigma - ig\frac{1}{2}(\bar{\sigma}\cdot\bar{W})\sigma - ig\cot(\theta)\frac{1}{2}(\bar{\sigma}\cdot\bar{W}^*)\sigma + i\frac{g}{\sin(\theta)}\frac{1}{2}\sigma\left((\tilde{W}_1,\tilde{W}_2)\cdot(\sigma_1,\sigma_2) + (c\phi\tilde{B} + s\phi B^*)\sigma_3\right), \tag{3.34}$$

where $c\phi = \cos(\phi)$ and $s\phi = \sin(\phi)$. Now since there is a new star field, B^*, we need to do one last rotation, again the one given in Eq. 3.27, which in this case means to replace $B^* \to s\theta B + c\theta B^*$, giving as a result

$$\begin{aligned} D_\mu\sigma \;=\; & \partial_\mu\sigma - ig\frac{1}{2}(\bar{\sigma}\cdot\bar{W})\sigma - ig\cot(\theta)\frac{1}{2}(\bar{\sigma}\cdot\bar{W}^*)\sigma \\ & + i\frac{g}{s\theta}\frac{1}{2}(s\phi s\theta\sigma\sigma_3 B + s\phi c\theta\sigma\sigma_3 B^* + \sigma(\tilde{W}_1,\tilde{W}_2)\cdot(\sigma_1,\sigma_2) + c\phi\sigma_3\tilde{B})). \end{aligned} \tag{3.36}$$

3.2.2 Fermions derivative

Next we will write explicitly the fermions derivative. First we will take the composite derivative, $D_\mu = \partial_\mu - ig_*(\rho_\mu^* + \tilde{\rho})$. In this case,

$$\rho_\mu^* + \tilde{\rho} = \bar{T}_L\cdot\bar{W}^* - \bar{T}_R\cdot\bar{\tilde{W}} + T_X X, \tag{3.37}$$

which replacing Eqs. 3.27 and 3.32

$$\rho_\mu^* + \tilde{\rho} = \bar{T}_L\cdot(\bar{W}^* c\theta + \bar{W} s\theta) - T_{R1}\tilde{W}_1 - T_{R2}\tilde{W}_2 - \tilde{B}T_{\tilde{B}} + T_{B^*}(s\theta B + c\theta B^*). \tag{3.38}$$

Finally, using that $g = g_* s\theta = g_{el} c\theta$, we arrive to

$$\begin{aligned} D_\mu \;&=\; \partial_\mu + ig(\bar{T}_L\cdot\bar{W} + BT_B) + ig\cot\theta(\bar{T}_L\cdot\bar{W}^* + B^*T_B) - ig_*(T_{R1}\tilde{W}_1 + T_{R2}\tilde{W}_2 + \tilde{B}T_{\tilde{B}}) \\ &=\; igA_\mu + ig\cot\theta\rho_\mu^* - ig_*\tilde{\rho}_\mu. \end{aligned} \tag{3.39}$$

In the same fashion, we can obtain the elementary derivative for fermions

$$D_\mu = \partial_\mu + igA_\mu - ig\tan\theta\rho_\mu^*, \tag{3.40}$$

with $T_{B^*} = T_B$.

Now we are left with the hypercharges. In the SM we have

$$\begin{aligned} T_Y\begin{pmatrix}u_L\\ d_L\end{pmatrix} &= \frac{1}{6}\begin{pmatrix}u_L\\ d_L\end{pmatrix}, \qquad T_Y\begin{pmatrix}\nu_L\\ e_L\end{pmatrix} = -\frac{1}{2}\begin{pmatrix}\nu_L\\ e_L\end{pmatrix}, \\ T_Y u_R &= \frac{2}{3}u_R, \qquad T_Y e_R = -1 e_R, \\ T_Y d_R &= -\frac{1}{3}d_R. \end{aligned} \tag{3.41}$$

	ψ	χ	$\tilde{\chi}$
T_B	$\sqrt{\frac{3}{5}}Y$	0	0
T_{B^*}	0	$\sqrt{\frac{2}{5}}\sqrt{\frac{3}{2}}Y$	$\sqrt{\frac{2}{5}}\sqrt{\frac{3}{2}}Y$
$T_{\tilde{B}}$	0	$-\sqrt{\frac{3}{5}}\sqrt{\frac{3}{2}}Y$	$-\sqrt{\frac{3}{5}}\sqrt{\frac{3}{2}}Y$

Table 3.2: Table with the fermion hypercharges of the $U(1)$ generators symmetries

Remember that the fields ψ transforms as SM ones, while χ and $\tilde{\chi}$ are different. To know the value of the hypercharges, we need to ask invariance of Y_{GUT} in the lagrangian. We can check the mixing terms, $\bar{\psi}_L \Delta \chi_R + \bar{\tilde{\psi}}_R \tilde{\Delta} \tilde{\chi}_L + h.c.$. The three $U(1)$ generators are given by

$$\begin{aligned} T_{B^*} &= Y_{GUT} = -\frac{T_{3R} + \xi T_X}{\sqrt{1+\xi^2}}, \\ T_{\tilde{B}} &= \frac{\xi T_{3R} - T_X}{\sqrt{1+\xi^2}}, \\ T_B &= \frac{5}{3} Y_{GUT} = \frac{5}{3} T_{B^*}. \end{aligned} \tag{3.42}$$

In the case of fermions, $T_{3R} = 0$ and so

$$\begin{aligned} T_{B^*} &= -\sqrt{\frac{2}{5}} T_X, \\ T_{\tilde{B}} &= -\sqrt{\frac{3}{5}} T_X, \\ T_B &= \sqrt{\frac{2}{3}} T_X. \end{aligned} \tag{3.43}$$

If we return to the mixing term, we need to keep the invariance of all the terms. We take $\bar{\psi}_L \chi_R$ as an example,

$$\begin{aligned} \bar{\psi}'_L \chi'_R &= \bar{\psi}_L e^{-i\overleftarrow{Y}_{GUT}} e^{i\overrightarrow{Y}_{GUT}} \chi_R, \\ &= \bar{\psi}_L e^{-i\sqrt{\frac{3}{5}}Y} e^{i\sqrt{\frac{2}{5}}T_X} \chi_R, \\ &= \bar{\psi}_L e^{-i\sqrt{\frac{3}{5}}Y} e^{i\sqrt{\frac{2}{5}}\sqrt{\frac{3}{2}}Y} \chi_R, \\ &= \bar{\psi}_L \chi_R, \end{aligned} \tag{3.44}$$

where Y is the hypercharge of the corresponding fermion in the SM and Y_{GUT} acts over each field following Eqs. 3.43.

In Table 3.2.2 we can find the hypercharges corresponding to each of the T_B's generators, following the descriptions given above.

3.3 EWSB

During the EWSB the Higgs boson takes the usual vacuum expectation value $v = 246$ GeV and there appears new masses for the bosons and fermions and also new mixings. The new diagonalized fermions are the SM quarks and leptons and their corresponding physical composite partners (which we do not consider here). The new diagonalized bosons correspond to the photon A, the Z, W^+ , W^- and the new heavy resonances which are the neutral Z_1 , Z_2 and Z_3 (combination of $\tilde{B}$, B^* and W_3^*) and the new charged $\tilde{W}$, W^* . For the purposes in this thesis, we need the neutral boson and SM fermions mass eigenstates and their interaction, therefore we require to perform another diagonalization because of the new terms coming from the EWSB.

The mixings between the neutral bosons are

$$M_0^2 = \frac{v^2}{4}\begin{array}{c} \begin{matrix} W_\mu^3 & B_\mu & W_\mu^{*3} & B_\mu^* & \tilde{B}_\mu \end{matrix} \\ \begin{pmatrix} g_2^2 & -g_Y g_2 & g_2^2\frac{c_2}{s_2} & -g_Y g_2\frac{c_1}{s_1} & -g_Y g_2\frac{1}{s_1}\sqrt{\frac{2}{3}} \\ -g_Y g_2 & g_Y^2 & -g_Y g_2\frac{c_2}{s_2} & g_Y^2\frac{c_1}{s_1} & g_Y^2\frac{1}{s_1}\sqrt{\frac{2}{3}} \\ g_2^2\frac{c_2}{s_2} & -g_Y g_2\frac{c_2}{s_2} & \frac{4M_{*2}^2}{c_2^2 v^2}+g_2^2\frac{c_2^2}{s_2^2} & -g_Y g_2\frac{c_1 c_2}{s_1 s_2} & -g_Y g_2\frac{c_2}{s_1 s_2}\sqrt{\frac{2}{3}} \\ -g_Y g_2\frac{c_1}{s_1} & g_Y^2\frac{c_1}{s_1} & -g_Y g_2\frac{c_1 c_2}{s_1 s_2} & \frac{4M_{*1}^2}{c_1^2 v^2}+g_Y^2\frac{c_1^2}{s_1^2} & g_Y^2\frac{c_1}{s_1^2}\sqrt{\frac{2}{3}} \\ -g_Y g_2\frac{1}{s_1}\sqrt{\frac{2}{3}} & g_Y^2\frac{1}{s_1}\sqrt{\frac{2}{3}} & -g_Y g_2\frac{c_2}{s_1 s_2}\sqrt{\frac{2}{3}} & g_Y^2\frac{c_1}{s_1^2}\sqrt{\frac{2}{3}} & \frac{4M_{*1}^2}{v^2}+g_Y^2\frac{1}{s_1^2}\frac{2}{3} \end{pmatrix} \begin{matrix} W_\mu^3 \\ B_\mu \\ W_\mu^{*3} \\ B_\mu^* \\ \tilde{B}_\mu \end{matrix} \end{array} \tag{3.45}$$

where $v = 246$GeV, $s_{1,2} \equiv \sin\theta_{1,2}$, $c_{1,2} \equiv \cos\theta_{1,2}$, and we are using $g_Y = \sqrt{3/5}\,g_1$. The rotation matrices for the fermions are given by

$$M_U = \begin{array}{c} \begin{matrix} u_L & U_L & \tilde{U}_L \end{matrix} \\ \begin{pmatrix} Y_u\frac{v}{\sqrt{2}} & \frac{c_L}{s_L}Y_u\frac{v}{\sqrt{2}} & 0 \\ 0 & m_*^Q & s_L^{-1}Y_u\, s_{R,u}^{-1}\frac{v}{\sqrt{2}} \\ Y_u\frac{c_{R,u}}{s_{R,u}}\frac{v}{\sqrt{2}} & \frac{c_L}{s_L}Y_u\frac{c_{R,u}}{s_{R,u}}\frac{v}{\sqrt{2}} & \tilde{m}_*^U \end{pmatrix} \begin{matrix} u_R \\ U_R \\ \tilde{U}_R \end{matrix} \end{array} \tag{3.46}$$

where $s_L \equiv \sin\varphi_{u_L}$, $c_L \equiv \cos\varphi_{u_L}$; $s_{R,u,d} \equiv \sin\varphi_{u_R,d_R}$, $c_{R,u,d} \equiv \cos\varphi_{u_R,d_R}$, and Y_u, Y_d (see Eq. 6.4 below).

The next step, in order to get the definitive Lagrangian, would be to diagonalized these matrices and replace the old fields by the new ones in the Lagrangian. To do this work analytically, is almost impossible, since the neutral boson mixing matrix is 5×5, so we are going to perform a decomposition in terms of powers of v. This should be taken cautiously and the results must be

checked in order to assure that they are consistent at a given scale and parameters. In the next subsections, we present these results for the diagonalization of the fermions and also the neutral bosons.

3.3.1 Fermions diagonalization after EWSB

Notice that the fermions mass matrices are given in terms of right and left fields. To be able to get the new mass states, we need to reproduce the method given in Sect. 3.1.1, where $M_i = M_{LR}$, $i = U, D$. From now on we will proceed with $i = U$ but it is exactly the same with the down. We take $M_f = M_{LR} M_{LR}^T$ and we diagonalize it. Once this is done, we will get the matrix C_L which contains the eigenvalue of M_f in columns and remembering Eq. 3.15 we replace old fields v_L with the mass ones v_L^{NB}. The same goes for v_R.

Now we will describe the diagonalization of M_f in powers of v.

We write the generic eigenvalues as

$$\lambda = \lambda_0 + \lambda_1 v + \lambda_2 v^2 + ... \tag{3.47}$$

where we will stay at second order. It is supposed that each order is smaller than the previous one, and that this will be enough for our purposes. Notice that M_f does not have contribution from v and so $\lambda_1 = 0$. The equation for eigenvalues is $\det(M_f - \lambda I) = 0$, so we expand λ and each order to be nule. In the first step, we ask order zero to be equal to zero, which gives us values for λ_0. We should get three of them since there are three eigenvalues. Next we take the first order, replace the λ_0 and equal to zero, to find λ_1. We can go to infinite order replacing the previous ones. The eigenvalues at second order are

$$\begin{aligned}
m_u^2 &= \lambda^1 = \frac{Y^2}{2} v^2, \\
m_\chi^2 &= \lambda^2 = m_*^2 + \frac{v^2}{2(m_*^2 - \tilde{m}_*^2)} \left(m_*^2 Y^2 \cot(\phi_L)^2 - \tilde{m}_*^2 Y^2 \cot(\phi_L)^2 + m_*^2 Y^2 \cot(\phi_L)^2 \cot(\phi_R)^2 \right. \\
&\quad \left. + 2 m_* \tilde{m}_* Y^2 \cot(\phi_L) \cot(\phi_R) \csc(\phi_L) \csc(\phi_R) + m_*^2 Y^2 \csc(\phi_L)^2 \csc(\phi_R)^2 \right), \\
m_{\tilde{\chi}}^2 &= \lambda^3 = \tilde{m}_*^2 + \frac{v^2}{2(m_*^2 - \tilde{m}_*^2)} \left(m_*^2 Y^2 \cot(\phi_R)^2 - \tilde{m}_*^2 Y^2 \cot(\phi_R)^2 - \tilde{m}_*^2 Y^2 \cot(\phi_L)^2 \cot(\phi_R)^2 \right. \\
&\quad \left. - 2 m_* \tilde{m}_* Y^2 \cot(\phi_L) \cot(\phi_R) \csc(\phi_L) \csc(\phi_R) - \tilde{m}_*^2 Y^2 \csc(\phi_L)^2 \csc(\phi_R)^2 \right).
\end{aligned} \tag{3.48}$$

These values are the square of the mass of each fermion. It can be checked replacing the fields and the diagonalized matrix in the lagrangian and using that $\bar{\phi}_L \phi_R + \bar{\phi}_R \phi_L = \bar{\phi} \phi$, since the left eigenvalues are equal to the right ones.

In the same fashion, we write the generic eigenvectors as

$$b = \begin{pmatrix} b_{01} \\ b_{02} \\ b_{03} \end{pmatrix} + \begin{pmatrix} b_{11} \\ b_{12} \\ b_{13} \end{pmatrix} v + \begin{pmatrix} b_{21} \\ b_{22} \\ b_{23} \end{pmatrix} v^2. \tag{3.49}$$

We will solve the equation for eigenvectors for each eigenvalue, $(M_f - \lambda^i I)b^i = 0$, in powers of v. We solve each power at a time, exactly as before. After this process, we will get all the b_{ij} in each eigenvector with some values still free. Remember that if w is an eigenvector, then cw with c a scalar is also an eigenvector, so we expect this free parameters to appear. Actually, we need them to normalize the eigenvectors. We will calculate the norm of the eigenvector taking into account all powers computed and then equal to one, so that first order should equal zero while all the others should be zero. Once this is done, we have all the normalized eigenvectors and we should check that the ortogonalization still holds order by order, neglecting higher orders. In this case the result is

$$b^1 = \left(1, -\frac{vY\cot(\phi_L)}{\sqrt{2}m_*}, 0\right), \tag{3.50}$$

$$b^2 = \left(\frac{vY\cot(\phi_L)}{\sqrt{2}m_*}, 1, \frac{vY(m_*\cot(\phi_L)\cot(\phi_R) + \tilde{m}_*\csc(\phi_L)\csc(\phi_R))}{\sqrt{2}(m_*^2 - \tilde{m}_*^2)}\right), \tag{3.51}$$

$$b^3 = \left(0, \frac{vY(m_*\cot(\phi_L)\cot(\phi_R)) + (\tilde{m}_*\csc(\phi_L)\csc(\phi_R))}{\sqrt{2}(m_*^2 - \tilde{m}_*^2)}, 1\right). \tag{3.52}$$

Using 3.15, we finally arrive to the new form of the fields as a function of the mass fields,

$$u_L = u_L^{NB} + \frac{vY\cot(\phi_L)}{\sqrt{2}m_*}\chi_L^{NB}, \tag{3.53}$$

$$\chi_L = \chi_L^{NB} - \frac{vY\cot(\phi_L)}{\sqrt{2}m_*}u_L^{NB} - \frac{vY(m_*\cot(\phi_L)\cot(\phi_R) + \tilde{m}_*\csc(\phi_L)\csc(\phi_R))}{\sqrt{2}(m_*^2 - \tilde{m}_*^2)}\tilde{\chi}_L, \tag{3.54}$$

$$\tilde{\chi}_L = \tilde{\chi}_L^{NB} + \frac{vY(m_*\cot(\phi_L)\cot(\phi_R) + \tilde{m}_*\csc(\phi_L)\csc(\phi_R))}{\sqrt{2}(m_*^2 - \tilde{m}_*^2)}\chi_L. \tag{3.55}$$

In the same way, working with $M_f f = M_{LR}^T M_{LR}$, we can get the right mass states,

$$u_R = u_R^{NB} + \frac{vY\cot(\phi_R)}{\sqrt{2}m_*}\tilde{\chi}_R^{NB}, \tag{3.56}$$

$$\chi_R = \chi_R^{NB} - \frac{vY(\tilde{m}_*\cot(\phi_R)\cot(\phi_L) + m_*\csc(\phi_R)\csc(\phi_L))}{\sqrt{2}(m_*^2 - \tilde{m}_*^2)}\tilde{\chi}_R, \tag{3.57}$$

$$\tilde{\chi}_R = \tilde{\chi}_R^{NB} - \frac{vY\cot(\phi_R)}{\sqrt{2}m_*}u_R^{NB} - \frac{vY(\tilde{m}_*\cot(\phi_R)\cot(\phi_L) + m_*\csc(\phi_R)\csc(\phi_L))}{\sqrt{2}(m_*^2 - \tilde{m}_*^2)}\chi_R. \tag{3.58}$$

Notice that we only have only two orders in the expansion of the eigenvectors. This is due, again, to the fact that the diagonalization comes from the left-right matrix times its transposed. We should then go to the next order, λ_3, which is zero. So we need the fourth order of the expansion. The eigenvalues are easily computed but have lots of terms and the eigenvectors are really tedious to work with, so for the sake of the lecture of this work and considering it mostly qualitative, we leave that for a future work.

3.3.2 Neutral bosons diagonalization after EWSB

Now it is time for the bosons. This case is much simpler since we do not need to use the trick of the right-left matrices, we simply diagonalize. As we expected, we find a zero mass boson and

another one with a mass equivalent to the Z boson of the SM, and three other masses with the original M_* as a first order approximation,

$$\begin{aligned} m_A^2 &= 0, \\ m_Z^2 &= \frac{v^2}{4}\left(g_2^2+g_Y^2\right), \\ m_{Z_1}^2 &= \frac{M_*^2}{c_2^2}+\frac{c_2^2 g_2^2 v^2}{4s_2^2}, \\ m_{Z_2}^2 &= \frac{M_*^2}{c_1^2}+\frac{c_1^2 g_Y^2 v^2}{4s_1^2}, \\ m_{Z_3}^2 &= M_*^2+\frac{g_Y^2 v^2}{6s_1^2}. \end{aligned} \tag{3.59}$$

Notice that in this case, the first order is also zero, but this time it is because the matrix that we diagonalized, in Eq. 3.45, is a square and the *vev* already there appears quadratic. The old boson fields, written as function of the new mass states, will be

$$\begin{aligned} W_3 &= \frac{g_Y}{\sqrt{g_2^2+g_Y^2}}A+\frac{g_2}{\sqrt{g_2^2+g_Y^2}}Z, \\ B &= \frac{g_2}{\sqrt{g_2^2+g_Y^2}}A-\frac{g_Y}{\sqrt{g_2^2+g_Y^2}}Z-\frac{c_2^3 g_2(g_2^2+g_Y^2)v^2}{4M_*^2 s_2\sqrt{g_2^2+g_Y^2}}Z_1+\frac{c_1^3 g_Y(g_2^2+g_Y^2)v^2}{4M_*^2 s_1\sqrt{g_2^2+g_Y^2}}Z_2+\frac{g_Y(g_2^2+g_Y^2)v^2}{2\sqrt{6}M_*^2 s_1\sqrt{g_2^2+g_Y^2}}Z_3, \\ \tilde{B} &= \frac{g_2 g_Y v^2}{2\sqrt{6}M_*^2 s_1}A-\frac{g_Y^2 v^2}{2\sqrt{6}M_*^2 s_1}Z-\frac{c_2^3 g_2 g_Y v^2}{2\sqrt{6}M_*^2 s_1 s_2(1-c_2^2)}Z_1+\frac{c_1^3 g_Y^2 v^2}{2\sqrt{6}M_*^2 s_1(1-c_2^2)}Z_2-Z_3, \\ B^* &= \frac{c_1^3 g_2 g_Y v^2}{4M_*^2 s_1}A-\frac{c_1^3 g_Y^2 v^2}{4M_*^2 s_1}Z-\frac{c_1^3 c_2^3 g_2 g_Y v^2}{4M_*^2 s_1 s_2(c_1^2-c_2^2)}Z_1-Z_2+\frac{c_1^3 g_Y^2 v^2}{2\sqrt{6}M_*^2 s_1^2(c_1^2-1)}Z_3, \\ W_3^* &= -\frac{c_2^3 g_2^2 v^2}{4M_*^2 s_2}A+\frac{c_2^3 g_2 g_Y v^2}{4M_*^2 s_2}Z-Z_1+\frac{c_1^3 c_2^3 g_2 g_Y v^2}{4M_*^2 s_1 s_2(c_1^2-c_2^2)}Z_2+\frac{c_1^3 g_2 g_Y v^2}{2\sqrt{6}M_*^2 s_1 s_2(1-c_2^2)}Z_3. \end{aligned} \tag{3.60}$$

In what follows, we will be interested in these new Z's, Z_1, Z_2 and Z_3. All these new Z,Äôs could be in principle easily tested through Z,Äô*orro* once the corresponding couplings are explicitly written.

3.3.3 Widths

Giving the following Lagrangian for the coupling of the new Z's to fermions,

$$Z'_\mu\left(g_u^L\bar{u}_L\gamma^\mu u_L+g_d^L\bar{d}_L\gamma^\mu d_L+g_u^R\bar{u}_R\gamma^\mu u_R+g_d^R\bar{d}_R\gamma^\mu d_R+g_e^L\bar{e}_L\gamma^\mu e_L+g_e^R\bar{e}_R\gamma^\mu e_R\right), \tag{3.61}$$

we can calculate the decay widths for the Z's (see appendix A),

$$\begin{aligned}
\Gamma_{qq}(Z' \to \bar{q}q) &= \frac{3M_{Z'}}{24\pi}\left(\left(g_q^L\right)^2 + \left(g_q^R\right)^2\right), \\
\Gamma_{ee}(Z' \to \bar{e}e) &= \frac{M_{Z'}}{24\pi}\left(\left(g_e^L\right)^2 + \left(g_e^R\right)^2\right), \\
\Gamma_{tt}(Z' \to \bar{t}t) &= \frac{3M_{Z'}}{48\pi}\sqrt{1-4\left(\frac{m_t}{M_{Z'}}\right)^2}\left(\left(g_t^R - g_t^L\right)^2\left(1-4\left(\frac{m_t}{M_{Z'}}\right)^2\right) + \left(g_t^R + g_t^L\right)^2\left(1+2\left(\frac{m_t}{M_{Z'}}\right)^2\right)\right).
\end{aligned} \tag{3.62}$$

The coupling of the neutral bosons to the W weak bosons and Higgs is non trivial to calculate and needs a little bit of development. It can be extracted in the unphysical basis, from the term $H^\dagger i\, g \cot\theta\, \rho_\mu^* D_\mu H + h.c.$ in the lagrangian of Eq. 3.30, and use the Equivalence Theorem [54]. According to it, the longitudinal W and Z are equivalent to the corresponding Goldstone Bosons in the high energy limit. Namely, the theorem states that if we parametrize the Higgs doublet as

$$H = \begin{pmatrix} \frac{w_1+iw_2}{\sqrt{2}} \\ \frac{v+h-iw_3}{\sqrt{2}} \end{pmatrix} \equiv \begin{pmatrix} w^+ \\ \frac{v+h+iw^0}{\sqrt{2}} \end{pmatrix}, \tag{3.63}$$

the longitudinal weak bosons will be described by w^+ and w^0 with h being the physical Higgs boson and the vector SM weak fields W and Z can be safely neglected [55]. The relevant part of the Lagrangian then takes the form

$$\frac{g\cot\theta_2}{2} W_3^{*a}{}_\mu(\partial^\mu h w^a - h\partial^\mu w^a + \epsilon^{abc} w^b \partial^\mu w^c). \tag{3.64}$$

Now we can compute the width we are interested on, which are

$$\Gamma(W_3^* \to Zh) = \Gamma(W_3^* \to W^+W^-) = \frac{g_2^2 M_*}{192\pi}\cot(\theta_2)^2. \tag{3.65}$$

Notice that these widths corresponds to the decay of the W_3^*, and not the new mass states Z'. To get the width corresponding to those states, we need to perform the diagonalization and extract the couplings of the new Z' to the SM bosons. This is not an easy task, since we should also consider the gauge Lagrangian and besides, we should include the rotations of the charged bosons. For the sake of simplicity, we use an approximation that works really fine at high masses. It goes as follows.

Eqs. 3.60 give the mixing between the neutral bosons after diagonalization at second order in v/M_*. In the original mixing matrix it can be seen that W_3^* has only one component at first order and it is diagonal, so there should be one mass state which is, at first order, only compound by W_3^*. We see from 3.60, in the line that shows the combination of bosons for the W_3^*, that the factor that goes with the so called Z_1 is one. So we expect W_3^* to be formed mainly by Z_1 and so that both have the same decay width to bosons. Fig. 3.1 shows the composition of the linear combination of the W_3^* as a function of the mass states for $M_* = 5$ TeV. It can be seen that the contribution from Z_2 and Z_3 quickly decays to zero as function of the θ_2 angle and that from the

A and the Z are practically zero all the way. A larger M_* assures that v/M_* is small and so the power series converges. For $M_* \sim 1$TeV we have for small angles, contribution of order one and we do not recommend going below 1TeV since the diagonalization may not be valid anymore.

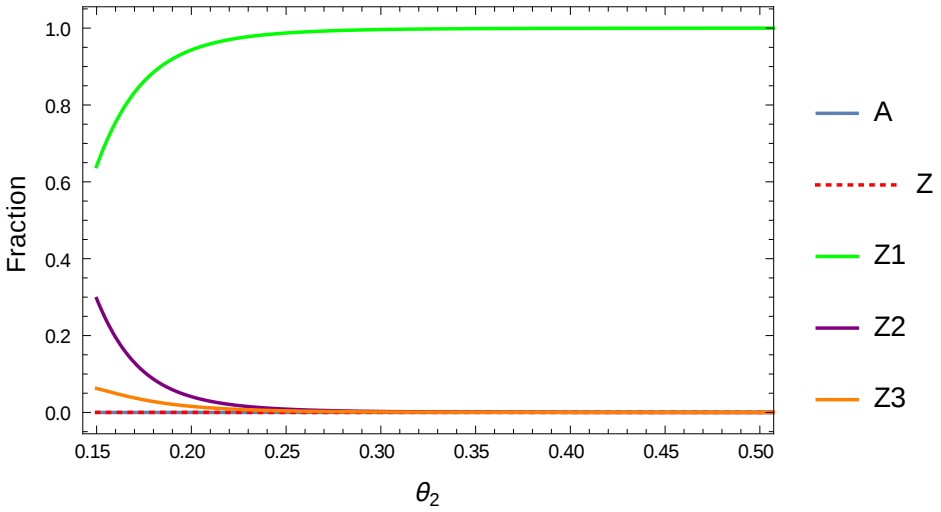

Figure 3.1: Factors as a function of θ_2 of the mixing between W_3^* and the mass state bosons for $M_* = 5$ TeV.

Now we may take a look to the masses of the new neutral bosons in order to seek the one with small mass, because this has the best chances to be found at the LHC and so it represents the most interesting one. Taking into account Eqs. 3.60, we can analyze the behavior of the masses in different ranges of the parameters. We found that for small angles and any considered value of M_*, the three masses are of the same order, see Figs. 3.2 and 3.3.

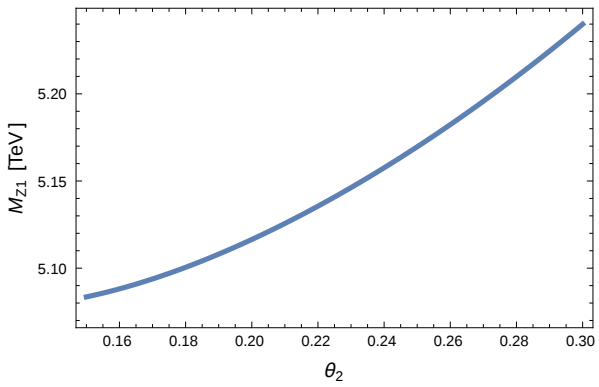

Figure 3.2: Mass of the Z_1 neutral boson as a function of θ_2 for $M_* = 5$TeV.

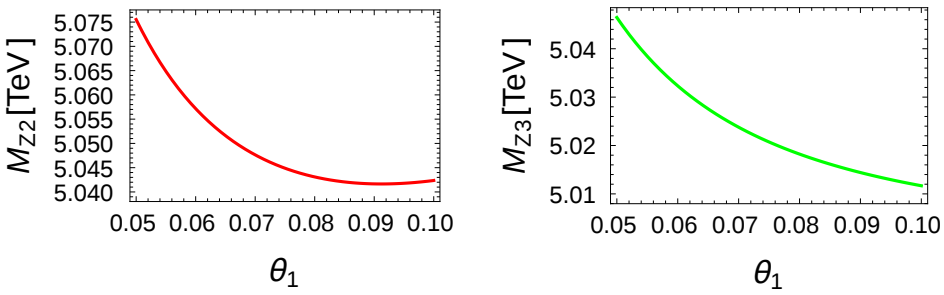

Figure 3.3: Mass of the Z_2 and Z_3 neutral bosons as a function of θ_1 for $M_* = 5$TeV.

Giving these results, we shall be working with the Z_1 neutral boson. Now we may question ourselves if this boson is or not representative of the whole pack. Is its phenomenology similar to that of the others? We think that this is true giving that the couplings g_* of the different forces are the same because the couplings and the widths will be of the same order.

This already mentioned, we approximate the decay width of the Z_1 to charged bosons as

$$\Gamma(Z_1 \to Zh) = \Gamma(Z_1 \to W^+W^-) = \frac{g_2^2 M_{Z1}}{192\pi} \cot(\theta_2)^2. \tag{3.66}$$

We need the couplings of the Z_1 boson to the fermions. This can be done substituting the old bosons for the mass states after the diagonalization in Eq. 3.28. We extract the couplings at second order in v. We considered $Y_f = 0$ except $Y_t = 1$ and $\phi_{bR} = 0$. See Appendix D for details. We have chosen $m = \tilde{m} = 2$TeV since we suppose that composite fermions are heavy and do consider to be able to detect them in this low energy phenomenology.

So far we have studied a simplification of the warped composite model by Contino [53] and performed power law approximations to obtain the couplings and widths of a chosen Z' to SM particles at second order in v. In Chapter 6 we will use the software Z'-explorer developed in this thesis to estimate the strengths and signals of the interaction of this Z' and find the parameter space where it is most sensitive.

CHAPTER 4

PROBING NEW PHYSICS AT THE LHC WITH $t\bar{t}b\bar{b}$

Within this chapter we study the $t\bar{t}b\bar{b}$ final state at the LHC as a probe of New Physics that couples mainly to third generation of quarks. We analyze New Physics simplified models with resonances of spin 0, 1 and 2. The sensitivity of the final states $t\bar{t}b\bar{b}$, $t\bar{t}t\bar{t}$, $b\bar{b}b\bar{b}$ and $t\bar{t}$ on each of these models is used to identify an important region in parameter space that is still not excluded and where $t\bar{t}b\bar{b}$ is the most sensitive final state. We discuss potential issues of observables that rely mainly in Montecarlo predictions. A new observable is proposed that, at the price of requiring more statistics, reduces the impact of Montecarlo predictions. We use preliminary 13 TeV results to give a raw estimate on the discovery reach and propose simple improvements on the observables.

4.1 Introduction

Motivated by a possible involvement of the third generation of quarks in the Electroweak Symmetry Breaking (EWSB), the large top mass and the small bottom mass, and some experimental hints in final states involving bottom and tops, we propose in this chapter to further study the final state $t\bar{t}b\bar{b}$ as a probe of NP at the LHC.

We pursue the question of what kind of NP would affect mainly this final state and, once this is stated, which region in parameter space is not yet discarded and how this and other observables would affect it. The answer to the first question requires a new particle that couples mainly –if not exclusively– to the third generation of quarks, the second part of the question is addressed in the following sections. The new particle should be singlet in color to avoid interaction with gluons. If the particle has spin 0, then a Two Higgs Doublet Model (2HDM) [36] would seem a good theoretical framework; however a 2HDM is a UV-complete framework that pays the price of imposing further conditions for the top and bottom couplings, which is what we want to

avoid at this level to keep the analysis as general as possible. Therefore, we consider scalar or pseudo-scalars 'boson-phobic' [56] whose top and bottom couplings have not *a priori* restrictions and allows for a more detailed exploration of the parameter space. A colorless spin 1 particle is what is known as a Z' [57] an has less theoretical issues, since it can only couple to right handed fermions. A spin 2 particle can also couple to only right handed fermions and, as it is shown in this thesis, it has many other attractive features. All these effective models are described in Sect.2.2 in the Introduction Chapter.

In this chapter we perform a qualitative analysis on the expected behavior of the simplify NP scenarios on the heavy flavour final states presented on the Introduction. In Sect. 4.2 we present our main results, the region in parameter space which has not been probed yet and in which $t\bar{t}b\bar{b}$ is expected to be the most sensitive final state. We discuss some relevant points in Sect. 4.3, including potential Montecarlo issues present in the $t\bar{t}b\bar{b}$ final state. We also propose a new observable which could be useful to reduce the impact of Montecarlo in the distinction of a NP signal, and we perform a raw estimate of the reach of existing observables.

4.1.1 General features

In this section we study the phenomenology of the models presented on Sect. 2.2 in the Introduction chapter and analyze their special features. All four simplified models have essentially the same Feynman diagrams. Depending on the point in parameter space under study, each diagram will have different importance as a function of the available energy in the proton PDF's and the phase space available for the possible decays.

Notice that for simplicity we have included in the loop only top and bottom quarks, and we will restrict to real and same-sign couplings. In principle, complex combination of these couplings and/or new heavy NP resonances in the loop function, can modify the effective vertex of the NP to two gluons.

We show in Fig. 4.1 the NP relevant diagrams. We call Y to any of the possible new particles in the previous sections (ϕ, A, φ, Z', $\tilde{Z}'$ or G) and M to any of their masses; except where explicitly stated different.

Diagrams D1, D3 and D4 –which are in general the most important production mechanism for Y–, are essentially the same diagram when the internal line in D1 is a b, with the only difference of whether the initial b quark is assumed in the proton, or not. As a matter of fact, the real difference in assuming the b in the PDF or not in each one of these processes depends on the factorization scale and the momentum of the b quark. For the phenomenological analysis that follows, we refer to these diagrams as whether the other b that comes from the corresponding gluon splitting is detected or not. In this sense, in addition to the Y decay products, we consider diagrams D1, D3 and D4 to have 2, 1 and none extra b's, respectively. This would make an important effect, since integrating out a b yields an inclusive cross-section larger than the exclusive one; specially because of the forward ($\eta > 2.5$) integration. Although in principle D4

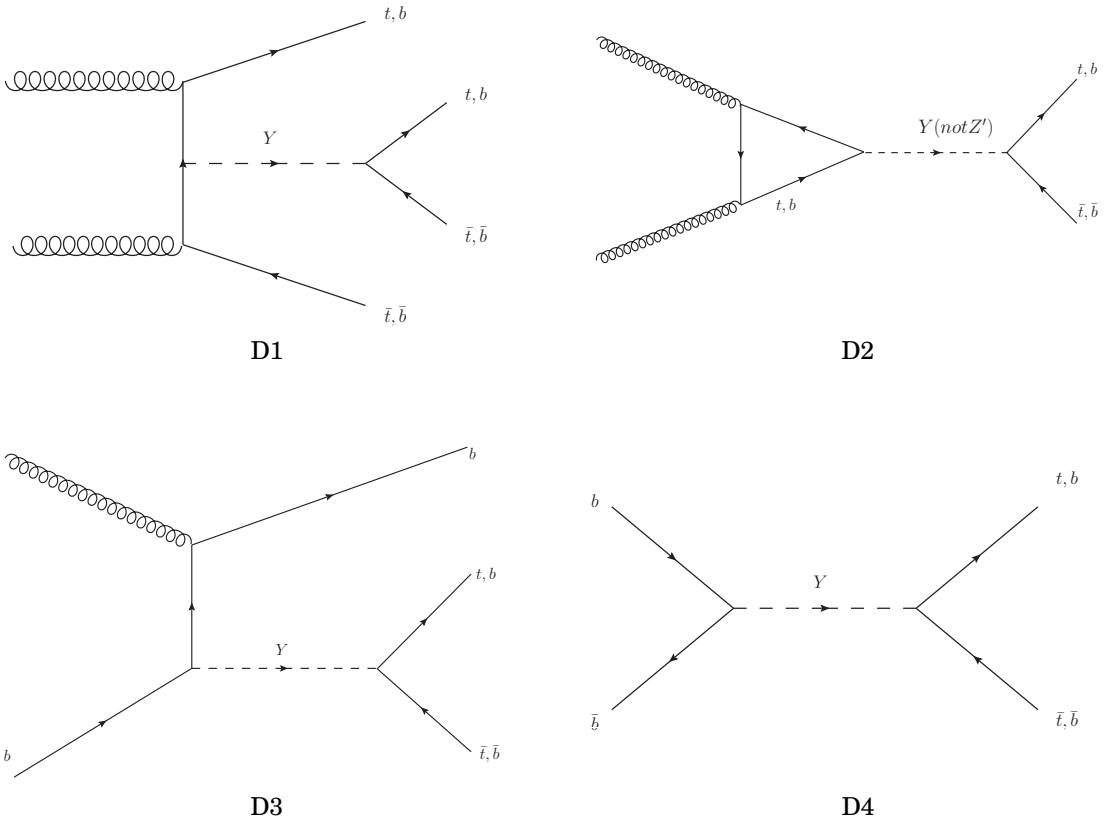

Figure 4.1: Relevant Feynman diagrams for processes in which NP that couples to the third generation of quarks could have an important effect in final states with 2 or more heavy quarks. Y refers schematically to any of the possible new particles described in text: ϕ, A, Z' or G; except in D2 where Z' is forbidden because of Yang's theorem.

would be the process with the more inclusive cross-section, its background $pp \to t\bar{t}$ is the largest of all and therefore its relevance is diminished. However, when comparing D1 and D3, they share the same main background, but D3 is more inclusive. This yields the important conclusion that, if the full final state is not required to be reconstructed, is in general better to look for the final states[1] $t\bar{t}bX$ and $b\bar{b}bX$ rather than $t\bar{t}b\bar{b}$ and $b\bar{b}b\bar{b}$, respectively; where X refers to the inclusiveness of the process. This last statement is however not totally true for $M < 2m_t$, since in that case we do not expect an improvement in $t\bar{t}bX$ with respect to $t\bar{t}b\bar{b}$, although we do in $b\bar{b}bX$ with respect to $b\bar{b}b\bar{b}$. This is because Y cannot decay to $t\bar{t}$ ($Y \not\to t\bar{t}$) and therefore the $b\bar{b}$-pair in $t\bar{t}b\bar{b}$ must come from Y, thus integrating out one b which is not expected forward should not make an important difference. This observation has important consequences in the phenomenology studied in the following sections: for $M < 2m_t$ the final state $b\bar{b}bX$ will be the

[1] Along this work we refer indistinctly to $t\bar{t}bX$ or $t\bar{t}\bar{b}X$. Analogously for $b\bar{b}bX$ and $b\bar{b}\bar{b}X$.

most sensitive channel in a larger region in parameter space.

An important observation regarding diagram D1 and conservation of angular momentum is to be noticed depending whether Y has spin 0, 1 or 2. Assuming null orbital angular momentum in final state, the case $Y = \phi$ or A yields a final state whose total angular momentum can only be 0 (since the initial state cannot have total angular momentum 1). Whether the case $Y = Z'$ yields a final state whose total angular momentum can be either 0 or 2. Since the initial state can couple in total angular momentum 0 or 2, one concludes that the case $Y = \phi$ or A is suppressed because of conservation of angular momentum in comparison to the $Y = Z'$ case[2]. In a similar way, for $Y = G$ the final state can only have total angular momentum 2, and therefore cannot come from an initial state with total angular momentum 0. We conclude from these observations that $Y = Z'$ is relatively much easier to discard, whereas $Y = \phi, A$ and G are harder to explore. This is explicitly seen in next section.

Diagrams D2 and D4 (with no extra b) in Fig. 4.1 yield a resonant final state in $t\bar{t}$ or $b\bar{b}$. Diagram D2 interferes destructively with the SM process $gg \to t\bar{t}/b\bar{b}$ [58] and therefore its usefulness needs to be explored carefully. The $t\bar{t}$ final state is the only one studied with relevant accuracy, but only for resonances up to Γ_Y/M larger than a few percents (and not much more, since wide $t\bar{t}$ resonance searches have not been explored in depth [58]). Given the precision in the results in $t\bar{t}$ invariant mass spectrum bump searches [59], this diagram could in principle be relevant for our purposes. On the other hand, diagram D4 is in general explored in extra scalar SUSY searches [10, 11], however always an extra b is required and one finishes in diagrams D1 and D3. It is interesting to notice that a $b\bar{b}$ resonance search with no extra b –which would correspond to D2– is a difficult task due to large background for small M and to the difficulty in tagging b-jets for large M [7, 8]. It is worth observing that a new resonance with $M < 2m_t$ and large couplings to tops would be detectable through processes as D1 and D2, in both cases with $Y \to b\bar{b}$. D1 would be suppressed due to phase space and D2 due to the loop.

The limit of a heavy Y ($M \gtrsim 1$ TeV) it is interesting for the $t\bar{t}bX$ final state. In fact, since very hard b's have a small tagging efficiency [7, 8], in this limit it is convenient to have the b quarks coming from the gluon-splitting in D1 and the new particle decaying to top quarks, $Y \to t\bar{t}$. Moreover, very hard tops are easy to tag using boosted top tagging techniques. Notice also that in this limit the $b\bar{b}bX$ final state will not be as useful because of the same issue in tagging hard b's.

In addition to the above discussion, there are other diagrams which could be important in special cases. For instance, a light ($M < 2m_t$) NP that couples exclusively to top quark would be visible in a $t\bar{t}t\bar{t}$ final state and t-channel diagrams would affect the total cross-section with no other special features, as studied in Ref. [16]. Also, for large coupling to b-quarks and $M \gtrsim 2m_t$, the t-channel $b\bar{b} \to YY$ diagram is important, and some times more important than gg-fusion.

[2] A similar and interesting situation holds in $pp \to t\bar{t}h$, which is so angular-momentum-suppressed that adding a final gluon, $pp \to t\bar{t}hg$ ($p_T(g) > 20$ GeV and $|\eta(g)| < 5$), yields a similar cross-section because of the extra angular momentum channel. As a matter of fact, $pp \to t\bar{t}h$ ends up having a considerable fraction of $q\bar{q}$ initial state collision to relieve this angular momentum tension.

At larger M this diagram becomes suppressed because of the PDF's.

A curiosity

There is a strange behaviour in the scalar case at around $M_\phi \sim 500GeV$. The major diference is found to be in the four top cross section. The $pp \to \phi t\bar{t}$ process seems to be benefited at high $C_{\phi b}$, while at first sight we would have said that b is not envolved in it and so it would be independent of that coupling.

The main contribution to the cross section is given by the Feynman diagram in Fig. 4.1, d1. But there is also a second diagram that contributes quite a lot, see Fig. 4.2. When the $C_{\phi b}$ coupling is big, the scalar couples so tightly to the bottoms that it is necessary to consider the b in the sea of the proton, since although the probability of finding these quarks is really small, the coupling enhances the probability of generating a scalar. In particular we can consider the process $bb \to \phi t\bar{t}$. At $M_\phi \sim 500$GeV, its probability is even an order of magnitude greater than the one given by the $gg \to \phi t\bar{t}$ process. But why this happens only for this mass? Well, this is because at $M_\phi \sim 350$GeV there is not enough phase space for the scalar to create two tops, while at high M_ϕ, the bottoms from the sea must carry a really big momentum to create two ϕ and so the process is suppresed (two orders of magnitude below the other for $M_\phi \sim 2000$GeV). This behaviour can be understood in a very clear way taking a look at Fig. 4.3.

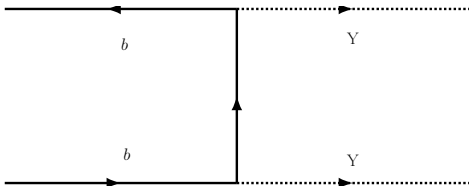

Figure 4.2: Feynmann diagram for the $bb \to \phi t\bar{t}$ process.

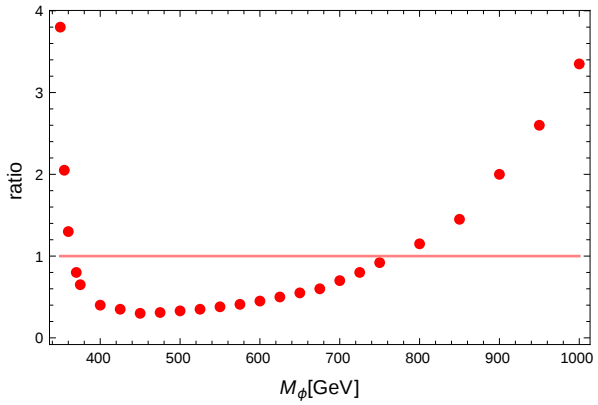

Figure 4.3: Ratio between the cross section production of the processes $gg \to \phi t\bar{t}$ and $bb \to \phi t\bar{t}$. The line indicates the ratio equal to unity, where both cross sections are identical. Below this line, the bottom produced diagram is the dominating.

4.2 ttbb sensitivity to NP

In this section we perform a quantitative comparison of the sensitivity of different channels to the NP presented in Sect. 2.2. We compare the process $pp \to t\bar{t}b\bar{b}$ to the other processes where this NP would manifest itself: $pp \to t\bar{t}t\bar{t}$, $b\bar{b}b\bar{b}$ and $t\bar{t}$. We do not consider $pp \to gg/\gamma\gamma$ since they are doubly loop-suppressed in production and decay, however other final states such as $\gamma\gamma t\bar{t}/b\bar{b}$ could be interesting to study in the future even though they are loop-suppressed in the decay.

When the experimental limit is differential in some variables, σ^{lim} results dependent on the given point in parameter space. To compare the strength S of the different channels, one should take experimental limits with the same center of mass energy and luminosity. In this case, we have unified the limits to a center of mass energy of $\sqrt{s} = 8$ TeV and a luminosity of 20 fb^{-1}. This procedure has been used in Refs.[52, 60], and is explained in full detail in Ref. [52]. In this last work it is discussed and shown that the analysis of the most sensitive final state in a given point in parameter space is approximately equally valid for different center of mass energies as long as the search strategy is not drastically changed and the production processes are not significantly modified due to changes in the PDF's. In this sense, we adopt in this thesis this second option: we study the most sensitive final state in available search strategies and propose that this relationship is approximately valid for LHC Run II. If one assumes that experimental limits in the studied final states have a similar scaling with luminosity, then the channel with larger S would be the first one to observe or exclude the postulated NP.

We have selected the most sensitive available published searches for 8 TeV and 20 fb^{-1} in the final states $t\bar{t}bX$, $b\bar{b}bX$, $t\bar{t}t\bar{t}$ and $t\bar{t}$, and compare the sensitivity in these searches to the proposed NP as a function of the parameter space.

In all cases we have predicted the excess due to NP using `MadGraph5_aMC@NLO` [61, 62]. In order to consistently compute the NP NLO effects a full gauge invariant theory is required, which is not the case in the presented models. However, to include an estimation of these effects, we can work under the assumption that a k-factor similar to their corresponding SM process would be a valid approximation. Using the available references [63, 64] and `MadGraph5_aMC@NLO`, we obtain that for the LHC running at 8 TeV all processes have a k-factor relating the cross-section between NLO and LO in the range $k \approx 1 - 1.5$, for renormalization and factorization scales going from $\mu_{R,F} = 0.5\mu_0$ to $\mu_{R,F} = 2\mu_0$. Where μ_0 is defined as half the sum of the transverse masses of all final particles. Along this work we use the strength S (Eq. 2.23) to either compare a ratio of strengths of two processes to test which process is more sensitive, or we compare its absolute value to 1 to see whether the NP is discarded. In the first case, if both processes have a k-factor that lies in $1 - 1.5$, but are approximately the same in both cases, then the k-factors cancel and the result agrees with the LO. We use this approximation when comparing the sensitivity of $b\bar{b}b\bar{b}$ and $t\bar{t}t\bar{t}$ to $t\bar{t}b\bar{b}$ ($k_{b\bar{b}b\bar{b}} \approx k_{t\bar{t}b\bar{b}} \approx k_{t\bar{t}t\bar{t}}$). If, on the contrary, both k-factors would vary independently, then one should expect a smearing of the lines dividing the most sensitive regions in the following results. This effect could shift the dividing lines, in the worst case scenario, up to approximately

~ 0.4 in term of the dimensionless couplings c_b and c_t. In the second case, when S should be compared to 1, a definite choice of the scales should be taken. We have adopted $\mu_{R,F} = \mu_0$ which yields $k_{t\bar{t}b\bar{b}} = 1.11$ and $k_{t\bar{t}} = 1.47$, for the relevant processes where an absolute value is required to limit regions.

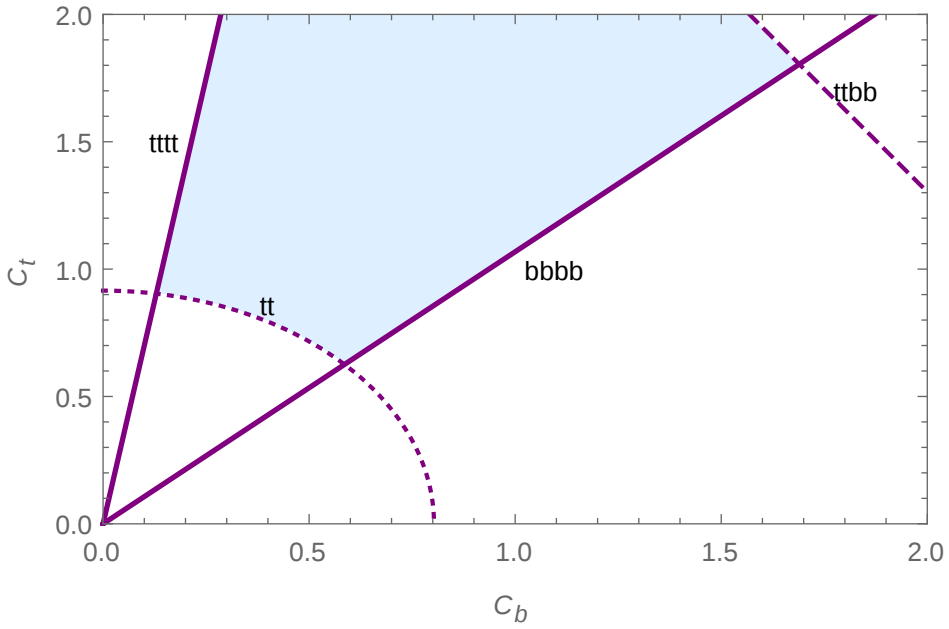

Figure 4.4: Reference plot for region in parameter space most sensitive to $t\bar{t}bX$. Solid lines represent borders in which another observable is more sensitive, although those points are not discarded. Long-dashed represents regions where $S(t\bar{t}bX) = 1$ and therefore points beyond that limit are discarded. Short-dashed represents the $t\bar{t}$ limit in which the resonance width goes above 8% of its mass and the $t\bar{t}$ resonance search looses validity [58].

For the final state $t\bar{t}bX$ we have worked with the search reported by ATLAS in Ref. [18]. To enhance the sensitivity to our NP we have chosen the reported measurement in $t\bar{t}$ with at least one additional b-jet, since this allows the other b-jet to be forward and not necessarily detected. This measurement, as all $t\bar{t}bX$ results, contain large systematic uncertainties due to the difficulties in modeling QCD effects and in tagging the bottom quarks. Following Ref. [18] and assuming no NP contributions in their measurement, we get that a 95% C.L. sensitivity corresponds to a cross-section 53% of the SM expected in the defined fiducial cross-section. An improvement in the sensitivity of this final state is expected to be achieved when differential measurements use data driven methods. CMS results in Ref. [21] work in that direction, however their sensitivity does not improve ATLAS yet because of the still little number of reconstructed events.

One of the most sensitive final states for the proposed NP is $b\bar{b}bX$. We extract the 95% C.L. sensitivity limits in this final state from Ref. [12]. This work looks for an excess in the invariant mass of the leading b's. Since the binning in the invariant mass ranges from $\sim 15\% - 50\%$ of the

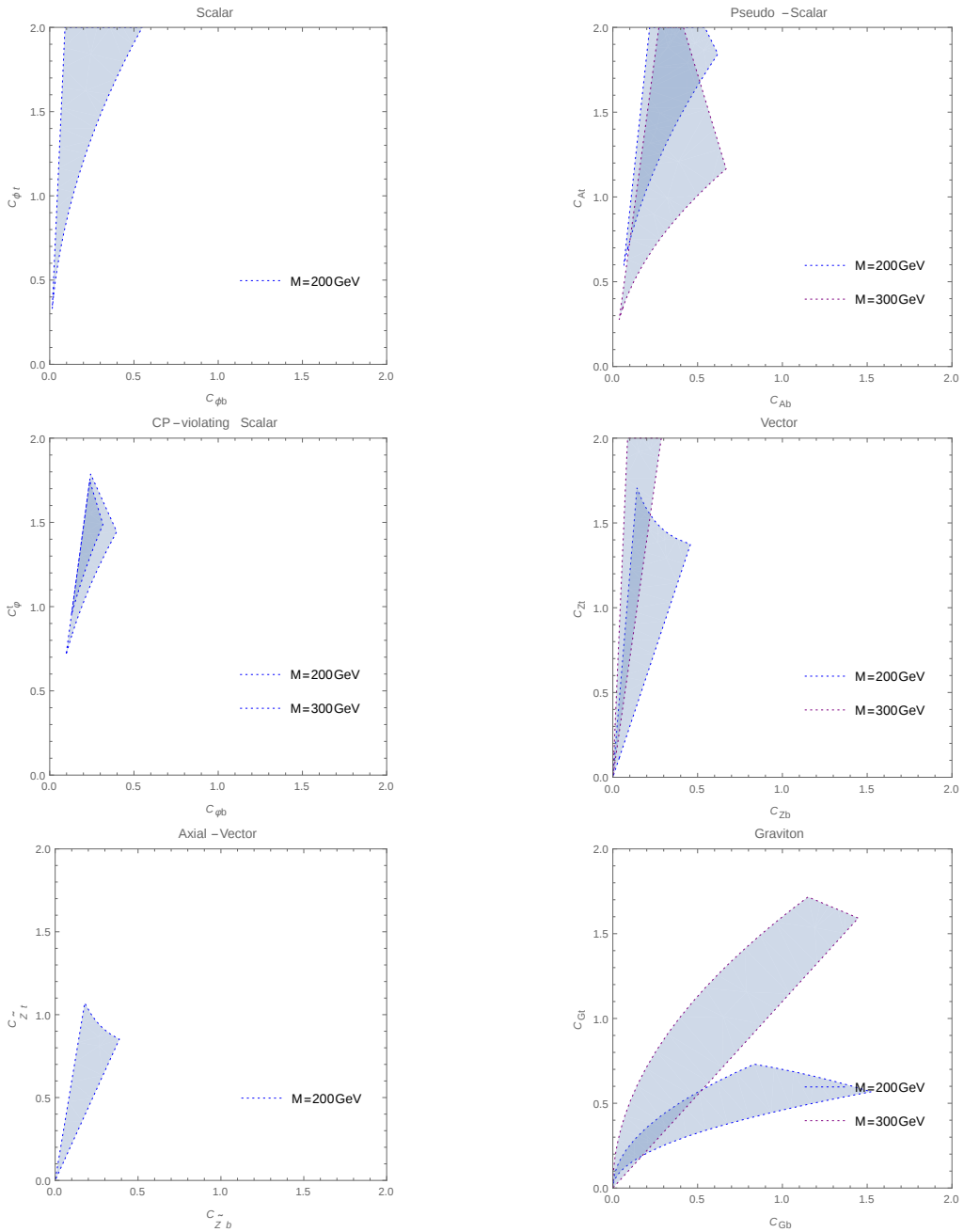

Figure 4.5: $t\bar{t}bX$ most sensitive region for small masses $M < 2m_t$. Since the $gg \to b\bar{b}Y$, $y \to t\bar{t}$ process is not allowed in this region, the $b\bar{b}bX$ final state has a large domination in sensitivity. See text for details.

sought mass, and we have verified numerically that NP-SM interference effects are not important, we take the limits from this work regardless of the resulting width of the resonance.

The sensitivity in the final state $t\bar{t}t\bar{t}$ should be extracted from a search that does not assume resonance production other than through interaction with top quark. According to [16], the closer to this is the SM $t\bar{t}t\bar{t}$ production. We therefore use the 95% C.L. limits found in Ref. [65] of 32 fb

as the limit cross-section for this final state.

The sensitivity in the channel $t\bar{t}$ has been extracted from Ref. [59], however we have followed Ref. [58] in what respects to signal-background interference in $t\bar{t}$ resonance searches. In particular, following their procedure, we have discarded this limit for points in parameter space where $\Gamma/M > 8\%$. We have simulated SM+NP to take into account the interference effects and, where comparable, we reproduce the results in Ref. [58].

Using the σ^{lim} extracted from the searches described above, unified to $\sqrt{s} = 8$ TeV and $L = 20$ fb^{-1} (see [52]), and using the predicted signal cross-section times branching ratios times acceptance for each one of these searches, we have computed the strength S for all the cases and compare in which points in parameter space is $S(t\bar{t}bX)$ greater than all others. In these points we expect the $t\bar{t}bX$ final state to be the most sensitive channel to the NP described in Sect. 2.2. Also, in the points in parameter space in which any $S > 1$, we consider that point to be discarded.

We have scanned the NP parameter space in different masses going from $M = 200$ GeV to $M = 3$ TeV, and for the numerical couplings $c_{ij} \in [0,2]$ ($i = \phi, A, Z', G$ and $j = t, b$). We present the results of the regions in parameter space in which $t\bar{t}bX$ is the most sensitive final state, and understand which is the most sensitive final state in each border.

In Fig. 4.4 we plot in detail for an arbitrary NP case how the $t\bar{t}bX$ most sensitive region looks, and which are the observable that constrain this region. As expected, the right side of the most sensitive region is usually constrained by the $b\bar{b}b\bar{b}$ observable, which becomes sensitive as the bottom coupling increases; here $S(b\bar{b}bX) > S(t\bar{t}bX)$. Analogously, the upper left side is constrained by the $t\bar{t}t\bar{t}$ final state: $S(t\bar{t}t\bar{t}) > S(t\bar{t}bX)$. On the up right side, there is a constraint that corresponds to direct exclusion by the $t\bar{t}bX$ observable, meaning that in this border $S(t\bar{t}bX) = 1$. On the down left side there is a constraint by direct $t\bar{t}$ resonance searches: $S(t\bar{t}) > S(t\bar{t}bX)$. Notice that Fig. 4.4 is just pictorial, and in many cases in the forthcoming figures some of these limits are not present.

Finally, it is important to observe that the shape of the $t\bar{t}bX$ most sensitive region is the outcome of a non-trivial process that includes the different channel cross-sections, the sensitivity of each one of these channels, and the relative magnitudes of their ratio, for each point in parameter space. Therefore its qualitative understanding could be not simple.

We plot in Fig. 4.5 the region in parameter space in which $t\bar{t}bX$ is the most sensitive channel for the cases $M < 2m_t$. As discussed in the previous section, the $b\bar{b}bX$ channel covers most of the parameter space because of its enhancement due to the inclusiveness that is not present in $t\bar{t}bX$ because $M < 2m_t$ and Y must decay to $b\bar{b}$. We also notice an important coverage of the $t\bar{t}t\bar{t}$ in the graviton case, as its coupling to fermions includes a derivative term that gets enhanced with the top mass, and suppressed with the bottom mass when fermions are on shell.

In Fig. 4.6 we plot the intermediate mass regions, $2m_t < M < 1$ TeV. Contrary to the previous case, now the $t\bar{t}bX$ process is enhanced because the missing b may come from the gluon splitting of diagram D3 in Fig. 4.1 and the resonance decay to $t\bar{t}$. Therefore, $t\bar{t}bX$ gains region against the

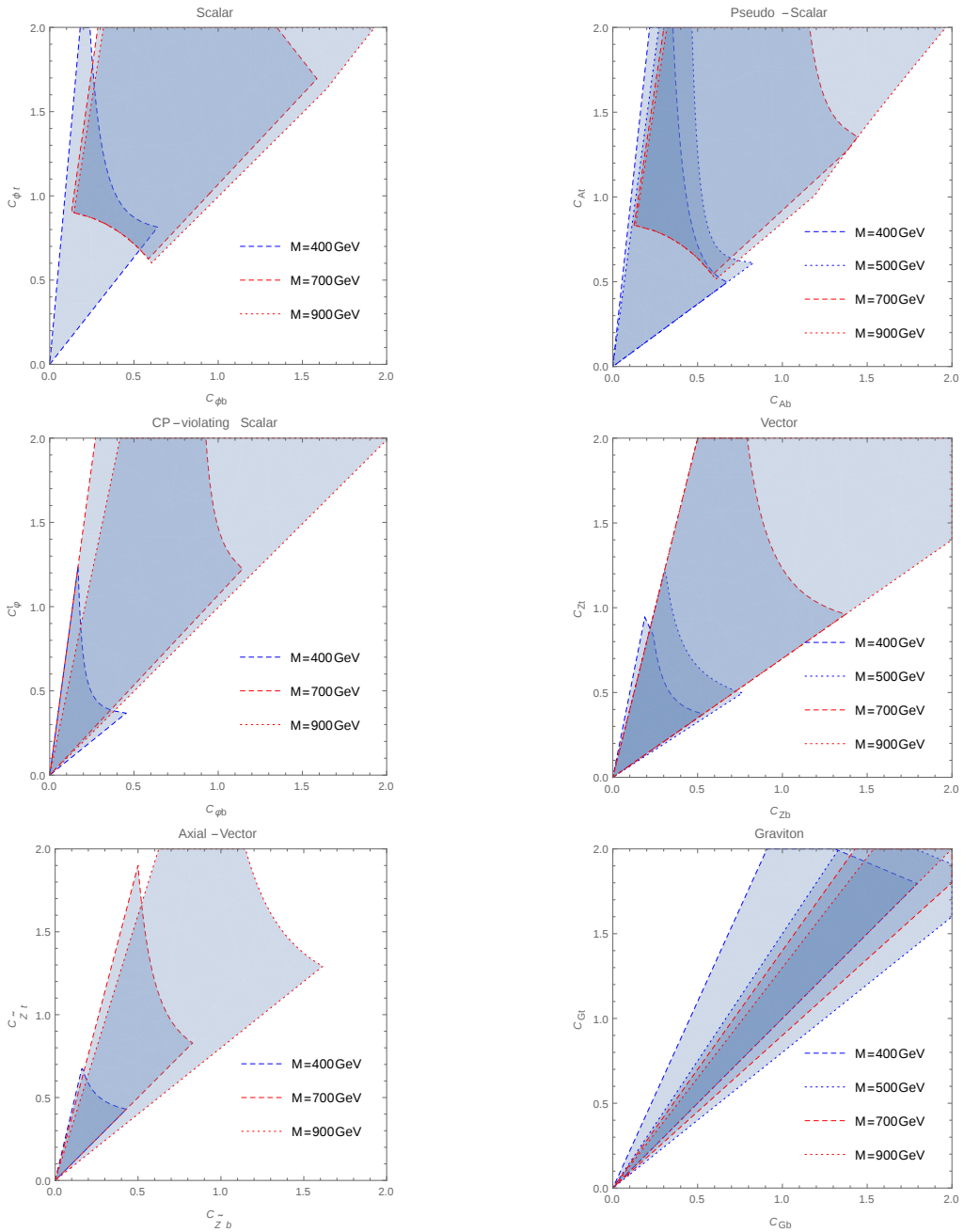

Figure 4.6: $t\bar{t}bX$ most sensitive region for intermediate masses $2m_t < M < 1$ TeV. In this case the $b\bar{b}bX$ domination gets balanced by the $t\bar{t}bX$ final state. Also a large region is discarded for the spin-1 Z' resonance due to angular momentum considerations. See text for details.

$b\bar{b}bX$ final state as it is easily seen in the figure. Another important feature is that the spin-1 Z' and $\tilde{Z}'$ are slightly more discarded than the spin-0 and spin-2 cases. This should be because, as discussed in previous section, the final state with a spin-1 resonance can match, for orbital angular momentum $\ell = 0$, both initial states of two gluons with total angular momentum 0 and 2,

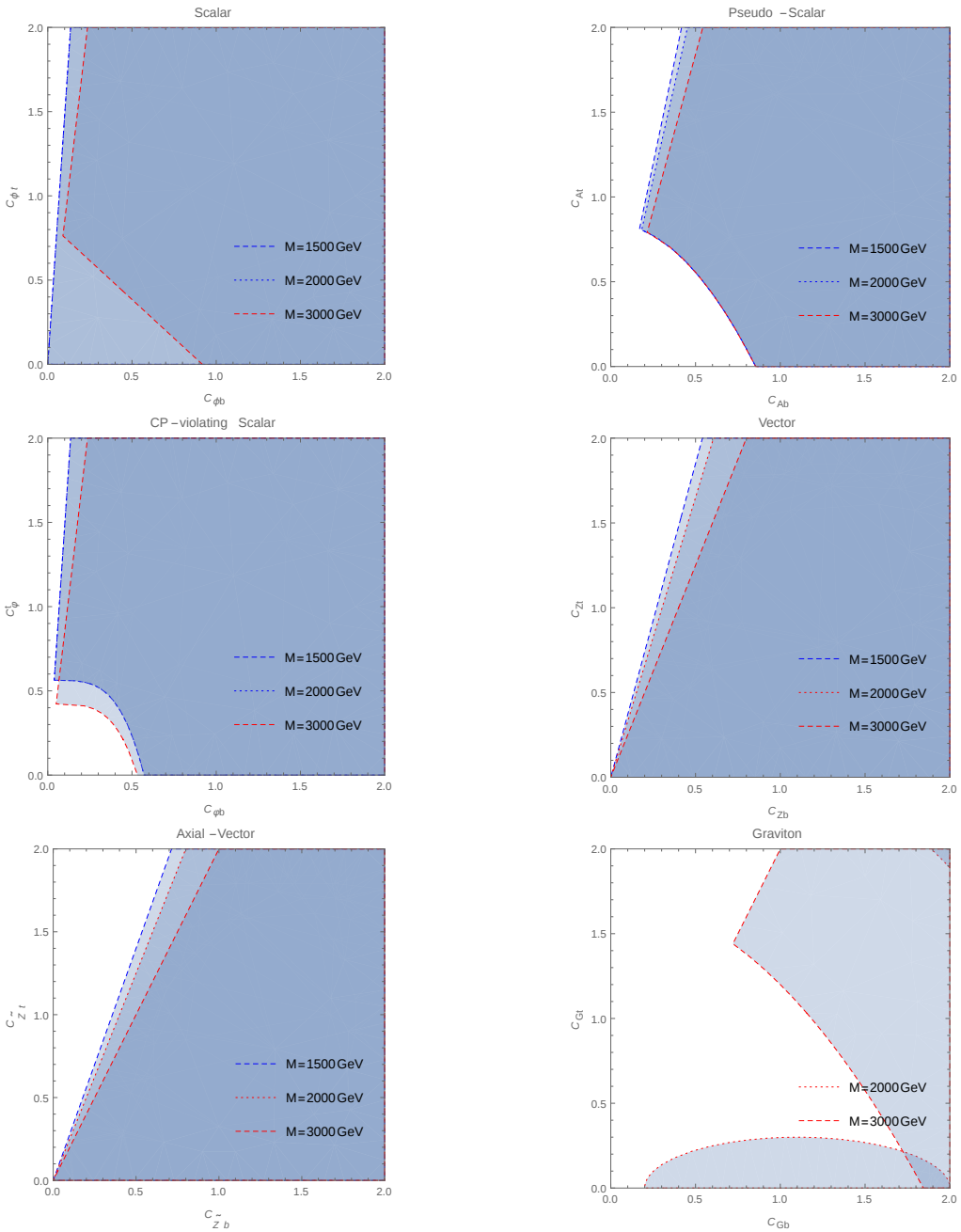

Figure 4.7: $t\bar{t}bX$ most sensitive region for large masses $M > 1$ TeV. See text for details.

and therefore is easier to explore/discard. Finally, we notice again that the $t\bar{t}t\bar{t}$ final state has larger impact on the graviton NP model.

The results for the large mass region $M > 1$ TeV are found in Fig. 4.7. The most important feature of this region is that the $b\bar{b}bX$ observable has no results due to the difficulty of tagging hard bottoms. This enlarges the $t\bar{t}bX$ most sensitive region all the way through the bottom right side, although of course the strength is expected to be quite small in regions where the

top coupling is very small. As a special feature in this mass region, we found that the graviton case has its most important constraint coming from $t\bar{t}$ resonance searches. In fact, for $M = 1.5$ TeV the whole parameter space in the figure is covered by $t\bar{t}$ searches (this cannot be seen from the figure), whereas for 2 and 3 TeV the sensitivity in $t\bar{t}$ is stagnant (see [59]) and $t\bar{t}bX$ gains relevance.

4.3 Discussion

Along the previous section we have shown that with the available experimental searches the final state $t\bar{t}bX$ is expected to be more sensitive than all other relevant final states in a considerable region in parameter space for the NP Lagrangians proposed in Sect. 2.2. However, many features in the study of the final state $t\bar{t}bX$ are still in the process of being further understood, and many points should be discussed in this sense. In this section we address some of this points and also propose some other new items which are relevant for the discussion of this final state.

4.3.1 Montecarlo in ttbb

The first measurements for $t\bar{t}b\bar{b}$ at the LHC performed in Refs. [17, 20] had both an excess of about twice the predicted cross-section, with a significance ranging approximately $\sim 1-2\,\sigma$. In this excess the Montecarlo simulation of the SM process, its hadronization, and the expected cross-section are a crucial input. In particular, it is well known that the treatment of the gluon splitting $g \to b\bar{b}$ is decisive for the 4 versus 5 flavor scheme [66], the factorization scale and the collinear divergences, yielding an important source of uncertainty [67] and also an eventual bias.

In the revision of the above cited references both collaborations ATLAS and CMS have taken different paths in addressing this issue with the Montecarlo prediction. The ATLAS collaboration has published in Ref. [18] a work with special focus on the Montecarlo simulations, in particular they discuss on how to tune Pythia variables that model the $g \to b\bar{b}$ splitting. Yielding a better agreement than in their previous work in Ref. [20]. However, one should be cautious, because also NP effects could be hidden in disagreements in the $b\bar{b}$ distribution of events. On the other hand, CMS collaboration published in Ref. [21] a continuation of Ref. [17], but now including differential measurements in $b\bar{b}$ which could contribute to distinguish NP effects observable such as $m_{b\bar{b}}$ and $\Delta R_{b\bar{b}}$ among others.

At this level it is suitable to distinguish observables such as the cross-section, whose prediction has a strong dependence in Montecarlo simulations, to other differential observables such as $m_{b\bar{b}}$ or $\Delta R_{b\bar{b}}$ in which the kinematic itself can predict a bump in the presence of NP. These bumps can in principle be distinguished by using the data in the side bands (in $m_{b\bar{b}}$ or $\Delta R_{b\bar{b}}$ distributions for instance) and, therefore, we consider these observables to have less Montecarlo impact when compared to others as for instance a fiducial cross-section. These observables are more reliable at the price of requiring more statistics.

In the previous discussion, the CMS approach seems more solid in their conclusions, however the ATLAS path requires less statistics. In fact, the CMS approach needs in most of the cases to fully reconstruct the $t\bar{t}b\bar{b}$ final state, which yields a great reduction in the number of events. Given the difficulties in generating a predictable distribution using Montecarlo simulations, we consider that a fully reconstruction of the $t\bar{t}b\bar{b}$ event and the search for observables with a reduced impact of Montecarlo generators is a better approach to look for NP in this particular final state, even though the lack of statistics would be one of the main issues.

4.3.2 Proposed observables

In addition to the well studied observables $m_{b\bar{b}}$ and $\Delta R_{b\bar{b}}$, which would respectively yield a bump or an excess in back to back events in case of a resonance, we propose different observables which can also be understood using kinematics.

We consider the general case of a resonance decaying to two particles and study the angle between these two particles 3-momentum (for simplicity we consider these particles of equal mass (m), however it could be adapted for different mass case). In the resonance frame of reference the decay products are back to back, but in the lab reference frame, the decay products get closer due to a Lorentz boost in the direction of the new particle momentum. From simple kinematics one can see that in the lab frame there is a minimum angle between the 3-momentum of these particles as a function of the resonance momentum and mass. This minimum angle occurs when the resonance momentum is orthogonal to the decay products direction in the resonance reference frame,

$$\Delta\theta_{min} = 2\arctan\left(\frac{M}{|\vec{p}|}\sqrt{1-\left(\frac{2m}{M}\right)^2}\right) \tag{4.1}$$

$$\approx 2\arctan\left(\frac{M}{|\vec{p}|}\right) \qquad \text{(massless case)}, \tag{4.2}$$

where $\vec{p}$ is the resonance momentum in the Lab Frame, or equivalently the added momentum of the 2 decay products.

Fig. 4.8 shows this minimun for the angle between the momentum of the two daughter particles $\Delta\theta$ as a function of the initial angle ϕ between the decay product direction and the boost direction.

We have also considered a random distribution for the initial angle ϕ and for the boost velocity, and plotted a histogram for $p\tan(\Delta\theta/2)$, where $p = |\vec{p}|$, which should correspond to the mass of the mother scalar particle. As seen in Fig. 4.9a, the histogram has a maximun for $M_\phi = 300GeV$, which is in fact the scalar mass in this case. We also took a distribution function of the form $f(x) = \cos^2(x)$ to simulate the effect that could produce a mother particle with spin 1. In this case, the maximun is shifted to the right (see Fig. 4.9b).

In the case of the $t\bar{t}b\bar{b}$ final state, if one of the quark pairs comes from a new resonance, then is likely that this new resonance has some transverse momentum since it has been produced in

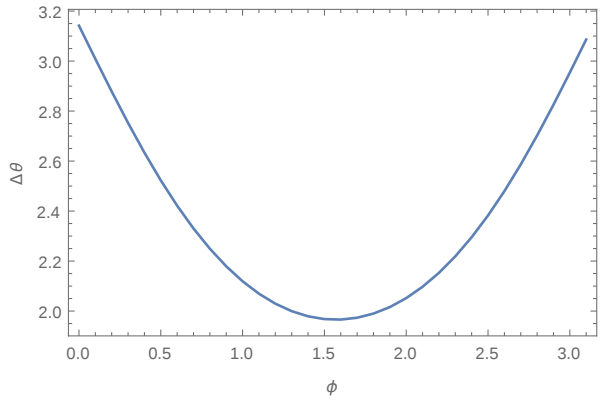

Figure 4.8: Angle $\Delta\theta$ between the two daughter particles as a function of the initial angle ϕ between boost and decay direction. There is a minimun at $\phi = \pi/2$, which means that the decay direction of both of the particles form an angle of $\pi/2$ with respect to the boost.

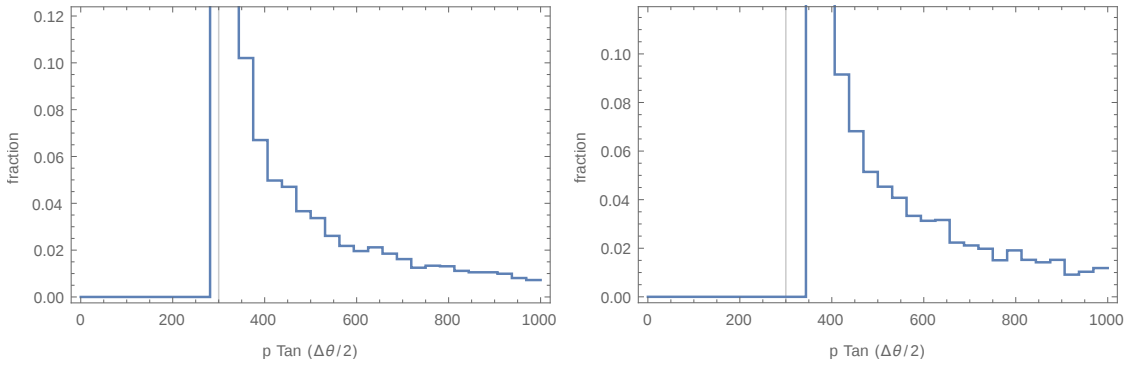

(a) (b)

Figure 4.9: Histograms for $p\tan(\Delta\theta/2)$, (a) with random distribution (scalar case) (b) squared cosine distribution (1-spin case).

association with other particles. In this case, we can adapt the above formulae for variables more suitable for colliders, in particular for the massless case we propose

$$\Delta R_{min} \approx 2\arctan\left(\frac{M}{p_T}\right) \qquad \text{(massless case)}. \tag{4.3}$$

Given the above observation, it is interesting to discuss which variables should be measured and compared to enhance the visibility of a possible signal. It is immediate to realize that the new particle decaying to, for instance $Y \to b\bar{b}$, would yield an accumulation of events in the $p_T(Y) - \Delta R_{b\bar{b}}$ plane, since the SM background is not expected to have such a kinematic constraint as in Eq. 4.3.

In Figs. 4.10 we see the scatterplot of $pT(tt)$ vs $\Delta R(bb)$ for the same final state, generated in two different ways, with $pp \to t\bar{t}Y, Y \to b\bar{b}$, and $pp \to b\bar{b}Y, Y \to t\bar{t}$. These processes are shown in Fig. 4.1, D1. There is a substantial difference that comes from the fact that when Y decays to bottom quarks, this are considered massless so we consider valid the relation given in Eq. 4.1,

while in the other case, when Y decays to top quarks, and when $m_Y \sim 2m_t$ we should consider Eq. 4.2. In this case, we can see that the limit is not really accurate.

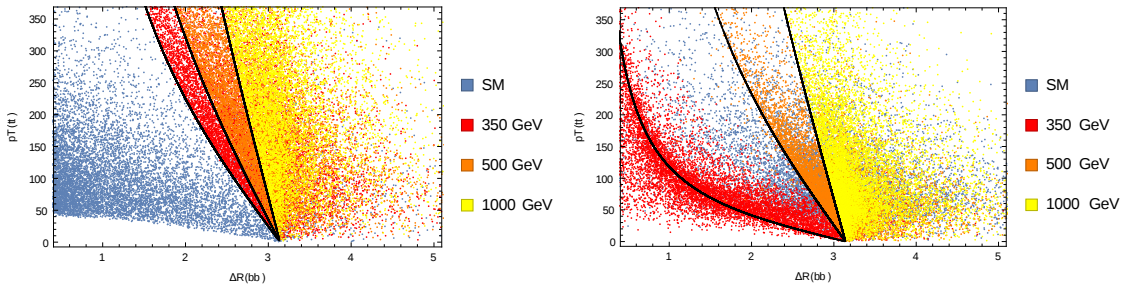

(a) (b)

Figure 4.10: Scatterplot of $pT(tt)$ vs $\Delta R(bb)$ for two different processes, (a) generation of $pp \to t\bar{t}Y, Y \to b\bar{b}$, (b) generation of $pp \to b\bar{b}Y, Y \to t\bar{t}$. In this last case, it can be seen that the limit is not so accurate for lower masses.

We show in Fig. 4.11a the distribution of events in the given plane for a case of SM+NP production in $pp \to t\bar{t}b\bar{b}$. Since the accumulation of events follows the curve predicted in Eq. 4.3, it is suitable to collect the events in the plane $p_T(Y) - \Delta R_{b\bar{b}}$ accordingly for different resonance mass. This is depicted in Fig. 4.11b. The 2-dimensional plot in this figure has not only the information of an eventual resonance if one looks at each collection of points between the plotted lines, but also the distribution of these points provides additional information. For instance, if these points would have a preference for high $p_T(Y)$, then it could mean that the production process would prefer energetic valence-quarks than gluons[3].

By defining the new variable

$$M_{boosted} = p_T \tan\left(\frac{\Delta R}{2}\right) \tag{4.4}$$

we can visualize some of the relevant information of Fig. 4.11a as in Fig. 4.11b, and then create a 1-dimensional binned plot where the resonance can be easily distinguished, as in Fig. 4.12. Observe that in this process we are producing a simpler-to-visualize plot at the price of loosing some of the information contained in the 2-dimensional plot. In this figure the events in between the curves in Fig. 4.11b have been collected in definite bins in $M_{boosted}$. A bump in this new variable, would be a NP signal with reduced impact of Montecarlo simulations; similarly to what happens with the $m_{b\bar{b}}$ and $\Delta R_{b\bar{b}}$ observables.

Some considerations on $M_{boosted}$ should be discussed at this point. The first thing to notice is that, as it can be easily seen, $M_{boosted}$ is neither not equivalent to the invariant mass $m_{b\bar{b}}$ nor the transverse mass m_T [40] of the decay products. In fact, to reconstruct $M_{boosted}$ are required the decay products direction and transverse momentum, which is not enough to reconstruct the invariant mass. Analogously, it is not the transverse mass m_T, since $M_{boosted}$ requires the

[3]This specific example is not valid for our model where the resonance only couples to third generation of quarks, but is depicted as a generic example on the usefulness of this kind of 2-dimensional plot.

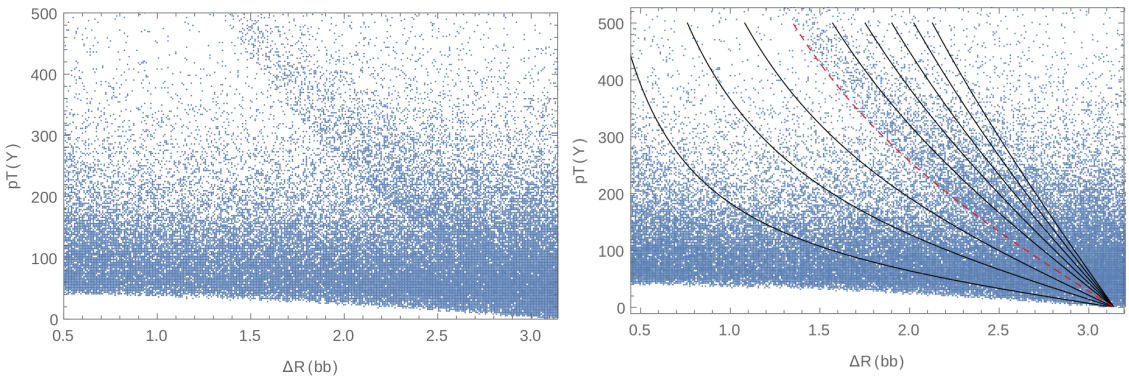

Figure 4.11: (a) Distribution of events in $pp \to t\bar{t}b\bar{b}$ for SM+NP. The NP produces $pp \to t\bar{t}Y$, $Y \to b\bar{b}$ events which, according to the discussion in text, generates an accumulation of events as it can be seen in the figure. (b) The same as in the left panel, but with superimposed contour curves of $M_{boosted}$ every 100 GeV (see Eq. 4.4). In red-dashed is the contour curve that corresponds to the resonance mass $M = 400$ GeV.

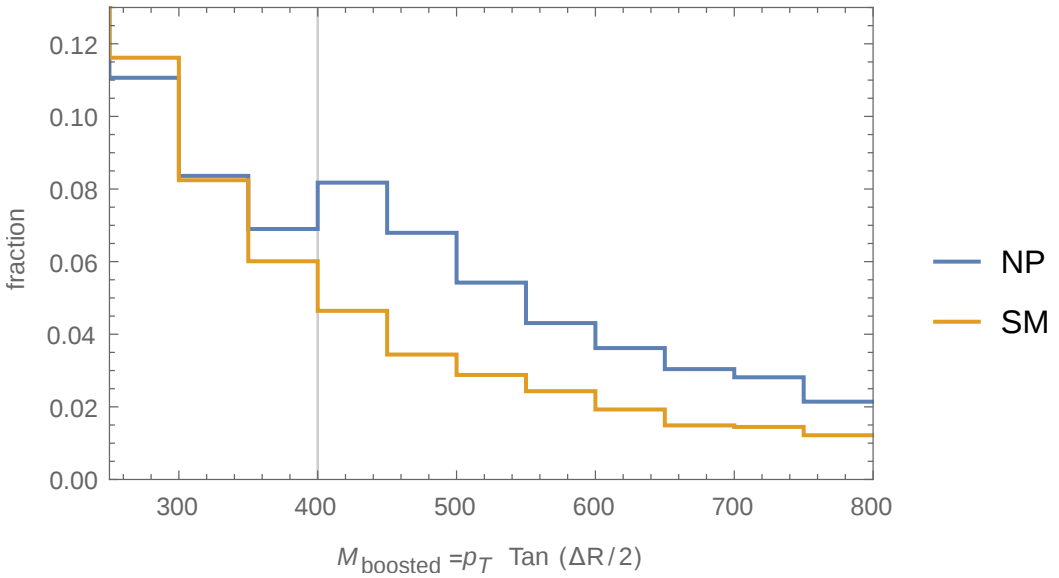

Figure 4.12: Binning of Fig. 4.11b. The correct binning using $M_{boosted}$ in the $p_T(Y) - \Delta R_{b\bar{b}}$ plane enhances a peak if resonant NP is present in the distribution of events. The shape of the peak contains information of the angular distribution of the resonance decay products as a function of the resonance momentum in the Lab Frame. (For better visualization the binning is every 50 GeV instead of 100 GeV as in Fig. 4.11b.)

longitudinal angular separation $\Delta\eta$ of the decay products and does not have an upper end-point. It should also be noticed that the $M_{boosted}$-distribution has information on the angle between the decay product directions in the CM frame and the resonance momentum in the lab frame. It can be shown that scenarios where this angle tends to be orthogonal have a sharper peak in the $M_{boosted}$-distribution. On the contrary, if this angle tends to be 0 or π, then the peak in the $M_{boosted}$-distribution is spread.

It would be interesting to investigate whether $M_{boosted}$ could have experimental advantages

over other observables as for instance $m_{b\bar{b}}$ and/or $\Delta R_{b\bar{b}}$. In fact, since it requires only the direction and transverse momentum of the decay products, it could have less uncertainty than $m_{b\bar{b}}$. From Fig. 4.11b one can understand $M_{boosted}$ as the extension of $\Delta R_{b\bar{b}}$ to the plane for the case of associate resonance production. Moreover, in this plot it is clearly seen that the use of $\Delta R_{b\bar{b}}$ in the search of NP in the $t\bar{t}b\bar{b}$ final state as in Ref. [21] is not optimal and should be improved.

Summarizing, we have proposed two related new observables, one is a 2-dimensional plot in the $p_T(Y)$-$\Delta R_{b\bar{b}}$ plane, and the other is its reduction to a 1-dimensional plot using the $M_{boosted}$ variable. Further analysis in both directions and including experimental aspects are beyond the scope of this work and should be addressed in a separate study. These could provide valuable information in the recognition of resonances produced in association with other particles.

4.3.3 Reach estimate using preliminary 13 TeV results

As a final point to discuss, we include preliminary results in $t\bar{t}t\bar{t}$ and $t\bar{t}b\bar{b}$ at 13 TeV, and do a raw estimation of the reach of these observables in the insofar explored NP parameter space.

In Ref. [22] a 95% C.L. limit is presented in the production cross-section times branching ratio of $pp \to t\bar{t}Y$, $Y \to t\bar{t}$ and $pp \to b\bar{b}Y$, $Y \to t\bar{t}$ for the intermediate mass region. These results have still large statistical uncertainties due to the little number of reconstructed events. We can therefore approximate the scaling of the strength with the luminosity as $S \propto \sqrt{L}$ [52] and obtain a raw estimate of the reach at larger luminosities by finding the $S = 1$ contour levels after the scaling.

We present in Fig. 4.13 the estimated reach for the 13 TeV observables for the $M = 500$ GeV case and for the four different NP models presented in Sect. 2.2. As expected, the $pp \to t\bar{t}Y$, $Y \to t\bar{t}$ limit has a better constraint for large top couplings and the $pp \to b\bar{b}Y$, $Y \to t\bar{t}$ observable for large top and bottom couplings. Notice that, as discussed in Sect. 2.2, the Z' model is the easiest to explore/discard due to its spin. Also notice in the figure how the graviton derivative coupling produces an interplay with the final state fermion masses: there is more sensitivity to tops, and less to bottoms.

The observables as proposed in Ref. [22] have a reduced impact of Montecarlo generators, requiring in this way more statistics. This is why their reach is not as restrictive as one would expect due to the energy upgrade.

It is worth pointing out that according to our discussion in Sect. 2.2, confirmed in the results in Sect. 4.2, the limit in $pp \to b\bar{b}Y$, $Y \to t\bar{t}$ would be considerably improved if the experimental analysis would not require to identify and tag both bottom quarks. That is, if the limit would be imposed in $pp \to bXY$, $Y \to t\bar{t}$. Since in this way there would be an enhancement in the signal due to the integration of a b jet beyond the $|\eta| = 2.5$ experimental limit. We consider that in doing this the limit in this observable would have an important improvement.

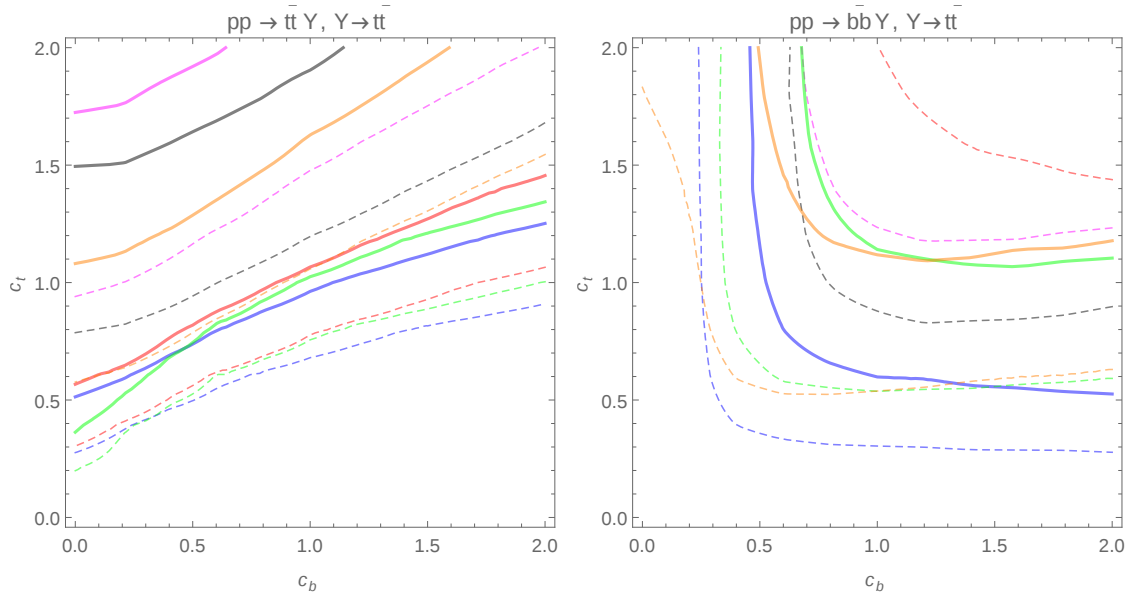

(a) (b)

Figure 4.13: (a) Reach estimate for the limits in $pp \to t\bar{t}Y$, $Y \to t\bar{t}$ in the different NP models of spin 0 scalar (magenta), pseudoscalar (black), CP-violating scalar (orange), vector (blue), axial-vector (green) and graviton (red), for $M = 500$ GeV. Solid and dashed lines corresponds to 300 fb^{-1} and 3000 fb^{-1}, respectively. Notice that as c_b increases, the branching ratio $Y \to t\bar{t}$ decreases and therefore also the reach of this observable. (b) Similar to left panel, but for the process $pp \to b\bar{b}Y$, $Y \to t\bar{t}$. These limits come from a preliminary result and are expected to improve in many aspects, as discussed in text.

CHAPTER 5

DIRECT V_{td} MEASUREMENT

This chapter contains three different works concerning the possible measurements of V_{td} coefficient. In the first part of the chapter, we propose a direct measurement of the CKM element V_{td} at the LHC. Taking profit of the imbalance between d and $\bar{d}$ quark content in the proton, we show that a non-zero V_{td} induces a charge asymmetry in the tW associated production. The main backgrounds to this process, $t\bar{t}$ production, and tW associated production mediated by V_{tb}, give charge symmetric contributions at leading order in QCD. Therefore, using specific kinematic features of the signal, we construct a charge asymmetry in the di-lepton final state which, due also to a reduction of systematic uncertainties in the asymmetry, is potentially sensitive to V_{td} suppressed effects. In particular, using signal and background simulations up to detector level, we show that this new observable could improve the current direct upper bound on $|V_{td}|$ already with existing LHC data. We project that $|V_{td}|$ values down to ~ 10 times the Standard Model prediction could be probed in the high luminosity phase of the LHC.
In the second part, we project these results to the HE(LHC) at 27TeV, in which case the significance did not improve, and find that actually for 7TeV the significance does increase.
In the third part of the chapter, we study the possible measurement of V_{td} using the former tj background as the new signal. The kinematical features gives tj and its conjugate $\bar{t}j$ different cross sections. The idea is to use this asymmetry to get rid of the symmetric backgrounds without relaying on charge asymmetry, thus diminishing the systematic uncertainties. We estimate V_{td}/V_{tb} using template fits. The results show that, at the same conditions as the previous proposal, the significance is actually smaller.

5.1 Measuring V_{td} using charge asymmetry

As discussed in Chap.2, there exist very few direct experimental handles on the third row of the CKM. The assumptions of CKM unitarity and dominance of SM contributions in loop-suppressed rare flavor processes, which allow for the precise third row CKM moduli determinations in Eqs.2.21, are in general not valid once one considers physics beyond the SM (see e.g. Ref. [68]). One possibility to approach such scenarios is to consider the mass decoupling limit, where the dominant new physics (NP) effects are captured by the SM effective field theory (SMEFT) [69, 70]. Unfortunately a completely general model independent analysis of constraints on Wtd_i interactions within the SMEFT framework has not yet been performed, and we can at present only relate to studies in more specific NP frameworks. For example, a comprehensive analysis of direct and indirect constraints on the Wtd_i (as well as Ztu_i, and Htu_i) interactions in models of heavy vector-like quarks [71] found that the strongest constraints on the Wtd_i couplings in such scenarios actually come from studies of top quark decays.

The aim of this chapter is thus to confront the SM predictions of $|V_{tq}|$ (as determined from indirect probes) using direct measurements of processes involving on-shell top quarks. The LHC, as currently the only top-quark production machine, can probe V_{tq} directly by studying top production as well as decays. In the present work we outline an experimental strategy to probe the $|V_{td}|$ matrix element directly at the LHC using single top production associated with a W boson ($pp \to tW$).[1] Our proposal exploits the production cross-section enhancement as well as boosts of the top quarks coming from initial state valence d-partons. In addition, and contrary to t-channel single top production, the main backgrounds have vanishing or very small charge asymmetries. This opens a path towards direct $|V_{td}|$ determination at the high luminosity (HL)LHC within an order of magnitude of the SM prediction.

This section is structured as follows. In SubSec. 5.1.1 we review the main effects of non-vanishing V_{td} on top quark production processes at hadron colliders. In SubSecs. 5.1.2, 5.1.3 and 5.1.4 we focus on the charge asymmetry in Wt production analyzing the dominant backgrounds and proposing an analysis strategy to reduce these while preserving most of the signal. The main results of this work are presented in SubSec. 5.1.5.

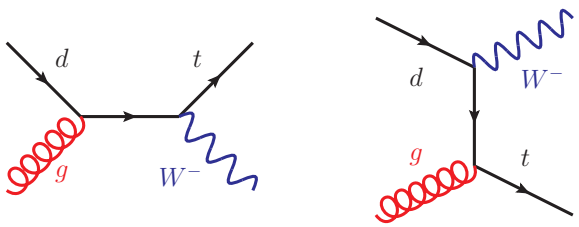

Figure 5.1: Feynman diagrams contributing to $pp \to tW$ production proportional to V_{td} at LO in QCD.

[1] For a previous study of possible NP effects in this mode see Ref. [72].

5.1.1 LHC processes and observables sensitive to V_{td}

Production of the top quark from an initial down quark in the proton is highly suppressed because of the expected smallness of $|V_{td}| \sim O(10^{-2})$. Any relevant process mediated via the tWd coupling is expected to produce a tiny signal, and thus would be difficult to measure directly at the LHC, both because of the small expected statistics and large backgrounds, but especially because of systematic uncertainties inherent to a hadronic machine. Therefore, observability of V_{td}-sensitive processes at the LHC is closely related to the capability of finding associated observables with reduced experimental systematic uncertainties. Common approaches to taming systematics include data-driven methods and asymmetries. Since the d-quark is a valence constituent of the proton, its imbalance with the $\bar{d}$-quark together with the charge self-tagging of leptonically decaying W bosons and top quarks motivates to explore V_{td}-sensitive observables in the form of charge asymmetries. In the following we will parameterize eventual departures from SM in V_{td} through the ratio

$$r \equiv \left| \frac{V_{td}}{V_{td}^{SM}} \right|, \tag{5.1}$$

in order to classify processes according to their leading power in r.

As a first process, we discuss the tW associated production mediated by the partonic process $gd \to tW^-$ (see Fig. 5.1 for the relevant leading order (LO) Feynman diagrams), whose cross-section is proportional to $|V_{td}|^2$ (and thus r^2). At LO in the SM $\sigma(tW^-) = 20$ fb [61] at the 13 TeV LHC, while for the CP-conjugate final state $\sigma(\bar{t}W^+) = 6$ fb. This process is interesting both because of its sizeable charge asymmetry but also because its kinematics predicts a characteristic angular distribution. In fact, the dominant diagram has a virtual top quark exchanged in the t-channel. Because of the relatively large incoming momentum expected on average from a valence d-quark, it consequently prefers a forward W^- in the lab frame. This special feature allows to consider the interesting di-lepton final state, which permits a relatively clean search strategy. In fact, this forward preference of the W^- is translated in having a preferably forward ℓ^- in signal events. The two main backgrounds to this $\ell^+\ell^- b$ final state would be the di-leptonic $t\bar{t}$ production (missing one of the b-jets from top decays) and tW associated production proportional to $|V_{tb}|^2$ (also in the leptonic decay channel of both the t and the W). Since this process features a collinear b coming from initial state gluon splitting (either re-summed as in the five-flavor PDF scheme, or explicit as in the four-flavor PDF scheme), in the following we denote is as $tW(b)$ production. Importantly, both backgrounds have very small charge asymmetries, and we expect a charge asymmetry constructed with this final state to exhibit promising sensitivity to V_{td}. Other reducible backgrounds and their relevance are discussed in more detail in the next subsection.

Another potentially important V_{td}-sensitive process is $pp \to tj$, where partonic processes such as $dq \to tq'$ and $d\bar{q}' \to t\bar{q}$ yield contributions that go as $|V_{td}|^2$, see Fig. 5.2. (Here $q = u, c$ and $q' = d, s, b$.) This process has a contribution where both initial quarks are valence quarks, $du \to td$, and therefore it is enhanced with respect to the contribution of its CP conjugate,

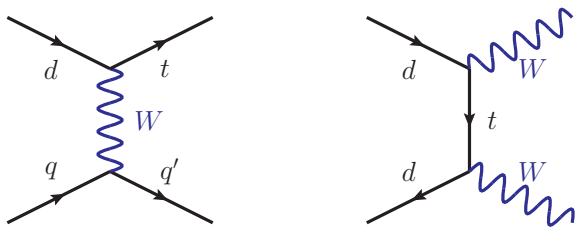

Figure 5.2: Examples of Feynman diagrams contributing to further V_{td}-sensitive processes at the LHC.

producing a charge asymmetry. However, its main background, the t-channel single top production ($pp \to tj(b)$) proportional to $|V_{tb}|^2$ is also significantly charge asymmetric. The sensitivity in this channel is thus limited by both the theoretical knowledge of its SM prediction and experimental systematics in its measurement, and we do not pursue it further.

So far we have discussed signals whose cross-sections are proportional to $|V_{td}|^2$ (r^2). One could however also consider (tree-level) processes contributing at higher orders in V_{td}. For instance, the contribution to WW production coming from $d\bar{d} \to W^+W^-$ with a top quark exchanged in the t-channel is asymmetric in the angular distribution of the final state particles and has a term proportional to $|V_{td}|^4$ (r^4). (See Fig. 5.2 for the relevant LO Feynman diagram on the right-hand side.) However, one of the main backgrounds to this signal would be the W^+W^- production mediated through the t-channel exchange of an up- or charm-quark, which has a similar asymmetry as the signal. Again in this case the usefulness of the asymmetry is reduced because one would need to compare it to a non-negligible reference number of the background. However, there are two features of this process that should be mentioned and which may deserve further exploration. One is that its cross-section has a term proportional to r^4, and although this contribution is suppressed by V_{td}^4, it is doubly enhanced compared to previous ones for $r > 1$. The second feature is that this process would affect both the angular and invariant mass distributions of the WW final state, and a sensitive observable could be constructed using side-band fitting.

There exist further V_{td}-sensitive processes which we do not discuss here. Instead in the remainder of the section, we focus on $pp \to tW$ and study the prospects of measuring or constraining V_{td} through a suitably defined charge asymmetry in the di-lepton final state channel.

5.1.2 Asymmetry sensitive to V_{td}

In this subsection we explore potential direct experimental sensitivity to V_{td} through the process $pp \to tW$ at the LHC. As discussed in the previous subsection, the kinematics of the signal offers the opportunity to distinguish the leptons coming from the W and the top decay, and therefore allows for a search strategy using a charge asymmetry in the $\ell^+\ell^- b$ final state. In the following sub-sections we first analyze the relevant backgrounds before constructing a suitable V_{td}-sensitive charge asymmetry. We end by discussing other charge asymmetries which could

provide further valuable observables in other contexts.

5.1.2.1 Backgrounds

In the following we discuss the main backgrounds and give an estimate of their size. The actual numbers used in our results are obtained through simulations described in the next subsection. We first note that the ATLAS and CMS collaborations have analyzed this process in both 8TeV and 13TeV LHC data [73–75]. Here we roughly follow Ref. [73] in the detailed characterization of the backgrounds, considering the final state with two leptons and a b-jet. We start by discussing the main backgrounds first.

The $t\bar{t}$ production in the fully leptonic channel with a missed b-jet leads to the same final state as the signal. Being produced by QCD interactions, this is the dominant background, with a LO cross-section of order $\sigma(t\bar{t}) \sim 500$ pb and at NLO $\sigma(t\bar{t}) \sim 680$ pb (both estimated through `MadGraph5_aMC@NLO` [61]). Requiring exactly one b-jet within the typical detector acceptance ($|\eta_b| < 2.5$ and $p_T(b) > 20$ GeV) and no other jet with $|\eta| < 5$ and $p_T > 20$ GeV, leads to a considerable reduction of this background, suppressing it by a factor $\sim 10^{-2}$ at parton level (details are discussed below). At LO $t\bar{t}$ arises from gluon fusion or from $q\bar{q}$ with a gluon in an s-channel, and so is completely charge symmetric. However, having a large cross section, it suppresses any net charge asymmetry by contributing to its denominator. At NLO this background does give a small asymmetric contribution, its size depending on the specific definition of the charge asymmetry, as described in the next subsection.

Another important background is given by the $tW^-(\bar{b})$ and $\bar{t}W^+(b)$ final states, without intermediate on-shell t or $\bar{t}$. [2] The LO production cross-section is $\sigma(tW(b)) \sim 28$ pb [61]. At NLO this background is expected to develop a small charge asymmetry, but since its cross-section is considerably smaller than $t\bar{t}$, in practice we can safely neglect it.

The Drell-Yan dominated $\ell^+\ell^- j$ production, with j misidentified as a b-jet, is in principle an important background. Since the lepton pair arises from an intermediate Z or γ, ℓ^+ and ℓ^- have the same flavor. The LO cross-section is of the order $\sigma(\ell\ell j) \sim 440$ pb. The presence of the jet induces a charge asymmetric distribution. This background can be drastically reduced by demanding different flavors of the final-state leptons at the expense of loosing half of the the signal. A significant reduction is instead obtained by demanding $m_{\ell\ell}$ larger than 25 GeV and excluding a region around the Z mass, that we choose between 75 and 105 GeV. Besides, since the signal has missing energy from the undetected neutrino arising from the leptonic decay of the top and W, whereas there is no missing energy for this background, we demand $E_T^{miss} > 30$ GeV. These cuts, in addition to a rejection factor of mis-tagging the light jet as a b, make the final contribution of this background to the cross-section negligible.

[2] In a four-flavor PDF scheme, this background is dominated by gluon fusion similar to $t\bar{t}$, whereas in the five-flavor PDF scheme the LO partonic process is $gb \to tW$ and the final state matches the signal exactly. See e.g. Ref. [76] for details on separating this process from $t\bar{t}$ production in simulations.

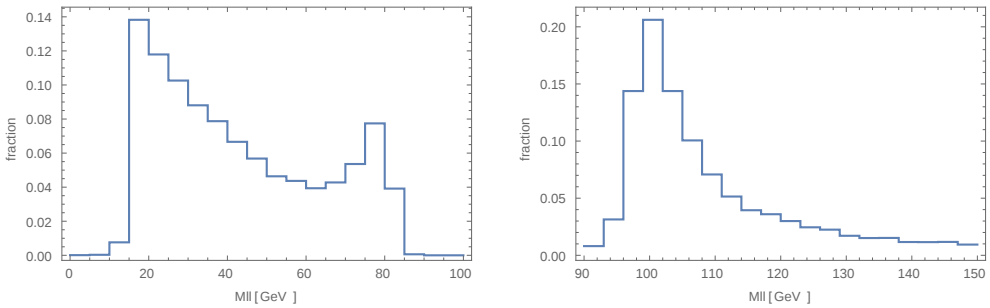

Figure 5.3: Fraction of events as a function of the invariant mass of the two leptons. The events were simulated for the $\ell\ell j$ process. On the left panel we have the small invariant mass, where $m_{\ell\ell} < 75$ and in the right one we have the large invariant mass, where $m_{\ell\ell} > 105$.

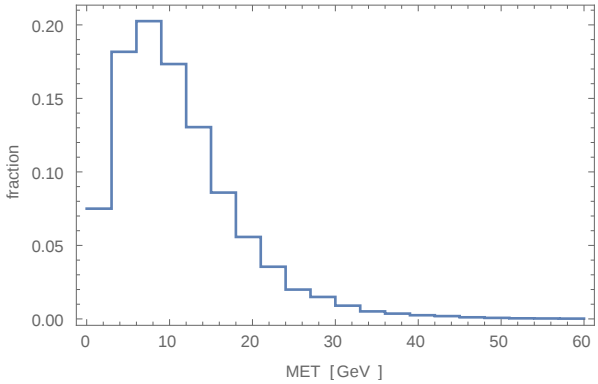

Figure 5.4: Fraction of events as a function of the missing energy. The events were simulated for the $\ell\ell j$ process. We can see that there is no missing energy above 30GeV.

There is also a background similar to the previous one, but with a $b/\bar{b}$ pair in the final state: $\ell^+\ell^- b/\bar{b}$. The LO cross-section is of the order $\sigma(\ell\ell b) \sim 32$ pb, but cuts in $m_{\ell\ell}$ and E_T^{miss} reduce this background as in the case of $\ell^+\ell^- j$. Although in the present case there is no significant rejection-factor associated with the jet(s), the asymmetry in $\ell^+\ell^- b$ is much smaller than the one of $\ell^+\ell^- j$, as can be expected since the b-quark is not a valence quark.

The t-channel single top production ($tj(b)$ and $\bar{t}j(b)$), with the j misidentified as a lepton, gives a large asymmetric background: $\sigma(tj(b)) \simeq 52$ pb and $\sigma(\bar{t}j(b)) \simeq 35$ pb, at LO. A lepton mis-identification rate of the order $\sim 10^{-4}$ [16] suppresses this background, leading to a negligible cross-section.

Other backgrounds include WWj, with j being either a light or heavy (b or c) jet flavor. The first case has a sizable charge asymmetry, although also a large rejection factor. The second case has a small rejection factor, but a tiny charge asymmetry. We have verified that both of these backgrounds are unimportant.

We note that some of the backgrounds listed above have contributions that depend on V_{td}, and could be enhanced for $r > 1$. However, even for $r \sim O(10)$, the size of the backgrounds does

not change significantly. In particular, the $t\bar{t}$ production is overwhelmingly dominated by QCD interactions, an increase of the very small V_{td} by a factor $O(10)$ has no discernible effect on this background. For the backgrounds $\ell\ell j$ and $\ell\ell b$, the di-lepton pair arises from an intermediate Z or γ^*, thus they are independent of V_{td} at LO. The t-channel single top background on the other hand includes contributions sensitive to V_{td} already at LO, but they are again very small for $|V_{td}| \lesssim O(10^{-1})$. As an example: for $r = 10$ ($r = 20$) the production cross-section increases by 5% (20%). Therefore, for moderate values of r this background does not have a significant growth. For WWj, there are Feynman diagrams depending on V_{td}, however, similar to the case of $t\bar{t}$, their contribution is tiny compared to the dominant contributions that are proportional to the diagonal elements of the CKM matrix. Thus, even for $r \sim O(10)$ the impact on this background can be neglected.

At last it should be mentioned that the partonic initial states gs and $g\bar{s}$ can generate an irreducible background controlled by V_{ts}, namely $gs \to tW$. However, this background has a cross-section suppressed by both the smallness of $|V_{ts}|$ and the strange quark PDF, plus a negligible charge asymmetry, therefore we can safely neglect it even for values of $|V_{ts}|$ at the current experimental upper bound.

Since the signal results in a $\ell^+\ell^- b\, p_T^{miss}$ final state, we enhance our signal over the main backgrounds $tW(b)$ and $t\bar{t}$ by requiring in the latter that only one of the b's falls into the acceptance region defined by $|\eta(b_1)| < 2.5$ and $p_T(b_1) > 20$ GeV while the second b is restricted to the regions $|\eta(b_2)| > 5$ or $p_T(b_2) < 20\ GeV$, mimicking a jet-veto aimed predominantly at suppressing the $t\bar{t}$ background (more sophisticated methods for dealing with this overwhelming background are discussed in the next sections).

5.1.3 tt suppression and extra jets study

We generate the process $pp \to t\bar{t}$ at parton level in `MadGraph5_aMC@NLO` [61] using $pp \to t\bar{t}, t \to bl_+\nu_l, \bar{t} \to \bar{b}l_-\bar{\nu}_l$, with $l = e, \mu$ and using sm-ckm package to have flavour mixing. For the process $pp \to tWb$, we use $gg \to tW^-\bar{b}/\bar{t}, t \to bl_+\nu_l, W^- \to l_-\bar{\nu}_l$ and also $gg \to \bar{t}W^+b/t, \bar{t} \to \bar{b}l_-\bar{\nu}_l, W^+ \to l_+\nu_l$, with the same conditions as above. This is to avoid useless diagrams with $q, \bar{q}$ in the mother particles because their contribution can be neglected. So we are left with backgrounds with two leptons and two jets.

To generate the signal $pp \to tW$, we use $gd \to tW^-, t \to bl_+\nu_l, W^- \to l_-\bar{\nu}_l$ and $g\bar{d} \to \bar{t}W^+, \bar{t} \to \bar{b}l_-\bar{\nu}_l, W^+ \to l_+\nu_l$. We also included the processes with dg and $\bar{d}g$ because they count in separate ways. Again, this are produced in the same conditions as the previous ones. Here we are neglecting the processes with strange quark because their contribution is much smaller than the one with down quark. The signal has two leptons and only one jet.

We perform a first study at partonic level for this three processes. We generated one hundred thousand of events for each one, and did some scatter plots of η vs p_T, for the leading and also the subleading jet (both b tagged). The idea is to compare these results with the following ones

at detector level. If the subleading jet p_T is less than a few GeV, then it won't be detected so the background will look like the signal, with one plus lepton, one minus lepton and only one b jet. We can see the plots in Fig. 5.5 that tt background has many more events with subleading jets in regions with high p_T than lower, so if we ask for a cut, and stay only with events which has subleading jet $p_T < 15$GeV, this background is very reduced (it survives only 5%). This does not happen with the twb background, where it is only reduced by 50%. Fig. 5.5 shows that tWb background has a great number of events with subleading jet with $p_T < 15$ GeV.

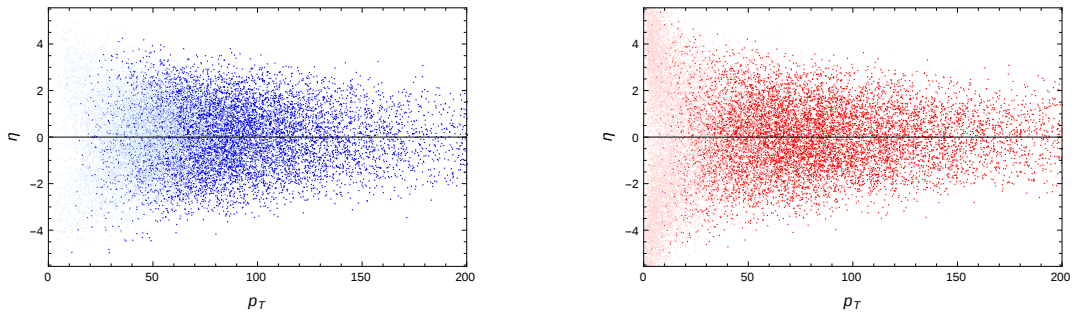

Figure 5.5: Leading (strong coloured) and subleading (light coloured) jets scatter plots, for tt (left) and tWb (right) backgrounds, at partonic level

We also performed simulations using Delphes to generate process at detector level the two mentioned backgrounds. Fig. 5.6 shows the plots for η vs p_T for both of them. In this case, the region with $p_T < 20$ GeV has already been cut.

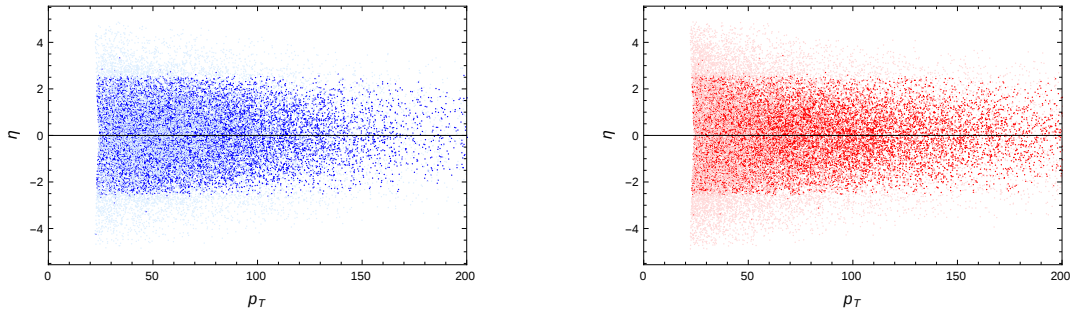

Figure 5.6: Leading (strong coloured) and subleading (light coloured) jets scatter plots, for tt (left) and tWb (right) backgrounds, at detector level.

Extra jets

We found that a high significance is achieved when asking for one l_+, one l_- and only one b-jet, the three of them having $\eta < 2.5$. We are comparing the asymmetry in $\Delta\eta$ and Δp_T. This reaches $S = 3.5 \cdot 10^{-5}$, or 3.5 per thousand if $V_{td} \sim 10$.

Fig. 5.7 shows a histogram of the number of jets n_j not b-tagged for each processes, in events which contains one l_+, one l_- and only one b-jet, and found that the signal has indeed more

events with $n_j = 0$, while the backgrounds have more events in $n_j > 0$. This means that asking for $n_j = 0$ is a good cut.

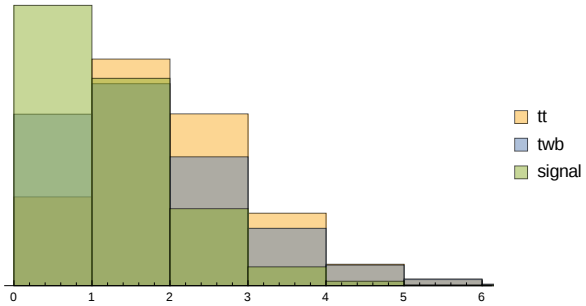

Figure 5.7: Histogram for number of extra jets. Most of the signal events have no extra jets, while the opposite is true for the tt and the tWb backgrounds.

We studied if a change in the R of the b-jet changes significantly the results. We reduced it from $R = 0.5$ to $R = 0.3$, leaving the rests of the conditions exactly as before. We found that the significance is reduced by an 9%.

Extra jets undetected

Although asking for no extra jets appears to be a fine cut, if a jet has a lower p_T value, it can be undetected and so, an event with lower p_T jets can be mistaken by a signal event. We studied how this affects the significance. We ask for the same conditions as before but allowing events with extra jets only if those jets have a p_T value below some specified threshold. In Fig. 5.8 we plotted the significance against p_T. There appears to be constant until the 20 GeV $< p_T <$ 45 GeV range, where it seems to be some kind of a linear behavior. We can conclude that asking for $p_T < 20$ GeV for the extra jets is a good cut. Taking a smaller value doesn't improve the significance, while taking a larger value will eventually take the significance to zero.

5.1.4 Selected cuts

In this way, we find that main backgrounds are suppressed through the following selection of events:

- Basic cut: Select events with $\ell^+\ell^- b$, all with $|\eta| < 2.5$ and $p_T > 20$ GeV.
- $t\bar{t}$ suppression cut: Veto events with additional jets within $|\eta| < 5$.
- $Z/\gamma^* j$ suppression cut: Veto events with $E_T^{miss} < 30$ GeV or $m_{\ell\ell} < 25$ GeV or $|m_{\ell\ell} - m_Z| < 15$ GeV.

In Table 5.1 we show how signal and main backgrounds are affected by these selection cuts.

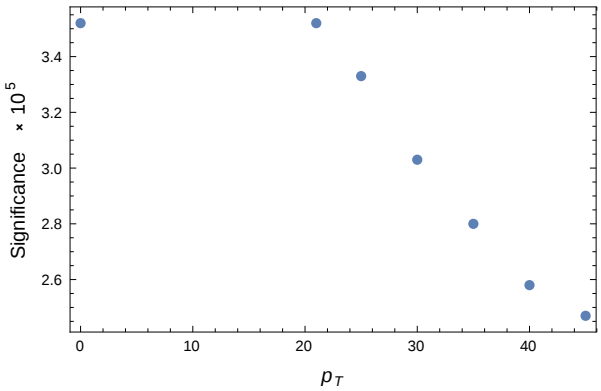

Figure 5.8: Loss in significance due to mistaken events with a subleading jet, as a function of the selected p_T cut for the subleading jet.

process	$\sigma \cdot B$ [fb]	basic [fb]	$t\bar{t}$ suppression [fb]	$Z/\gamma^* j$ suppression [fb]
signal	$1.2\,r^2$	$0.59\,r^2$	$0.53\,r^2$	$0.35\,r^2$
$t\bar{t}$	3.1×10^4	3.4×10^3	1.4×10^3	9.6×10^2
$tW(b)$	1.8×10^3	7.4×10^2	6.3×10^2	4.1×10^2

Table 5.1: Cut flow for the signal process and for the main backgrounds $t\bar{t}$ and $tW(b)$ at parton level as described in the text. Each column adds a new cut to the previous columns. As it can be seen, this selection of events is not enough to elevate the signal over the backgrounds; this is achieved in the next paragraphs where we construct an asymmetry that takes profit of the different distributions in the signal and backgrounds. Simulation details are described in SubSect. 5.1.5.

5.1.4.1 Enhancing a charge asymmetric signal over a (mostly) symmetric background

Given the above discussion we are left with a charge asymmetric signal in $pp \to tW$, and the approximately symmetric main backgrounds $pp \to t\bar{t}$ and $pp \to tW(b)$. Other backgrounds are negligible or become negligible after a cut in E_T^{miss} and $m_{\ell\ell}$, such as $pp \to Z/\gamma^* j$.

In order to quantify the different signal and background features expected from the previous qualitative analysis, we first consider the relevant parton level distributions of the signal and the main backgrounds. For this purpose, we have simulated at parton level the signal and $tW(b)$ at LO and $t\bar{t}$ at NLO in QCD, as explained in Sect. 5.1.5. We have simulated the events at parton level using `MadGraph5_aMC@NLO`. The $tW(b)$ background has been simulated in the four-flavor PDF scheme with $m_b = 4.7$ GeV, resulting in a tWb final state.[3] Thus, for both backgrounds we

[3] See Ref. [66] for discussion on the appropriate use of this scheme.

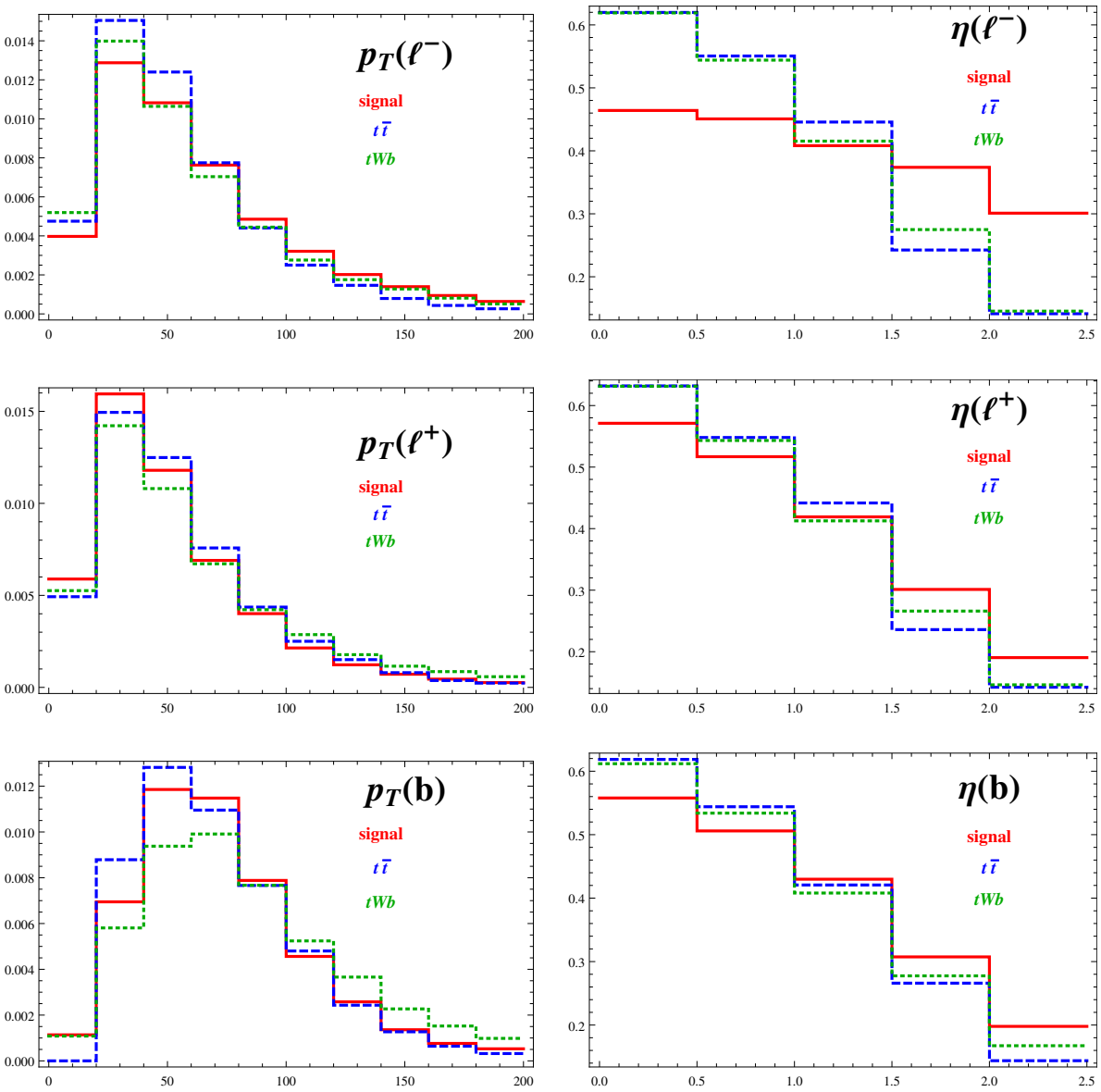

Figure 5.9: Distributions of p_T and η of the final particles at parton level for the signal (red and continuous) and the main backgrounds $t\bar{t}$ (blue and dashed) and $tW(b)$ (green and dotted). Each sample contains the corresponding process and its charge-conjugate, since on an event-by-event basis one cannot distinguish which lepton comes from the t decay and which from the associatively produced W decay.

have required that only one of the b's falls into the acceptance region defined by $|\eta(b_1)| < 2.5$ and $p_T(b_1) > 20$ GeV while the second b is restricted to the regions $|\eta(b_2)| > 5$ or $p_T(b_2) < 20\ GeV$, mimicking a jet-veto aimed predominantly at suppressing the $t\bar{t}$ background (more sophisticated methods for dealing with this overwhelming background are discussed in the next subsection). The results are shown Fig. 5.9. We observe that the most important difference comes from

the $\eta(\ell^-)$ distribution, where the signal clearly prefers forward negatively charged leptons, as expected from the qualitative discussion in SubSect. 5.1.1. A similar preference is also present in the $\eta(\ell^+)$ and $\eta(b)$ distributions, although much less pronounced. On the other hand, the p_T-distributions of the signal and the backgrounds do not offer as clear a differentiation as in the η case. For example, the $p_T(b)$ ($p_T(\ell^-)$) distributions could only be used to distinguish the signal from $tW(b)$ ($t\bar{t}$), respectively.

Given these distinctions between the signal and backgrounds in one-variable distributions, we next study distributions of pairs of variables in order to construct the most sensitive observables that could enhance the signal over the background. With this purpose, and motivated by the results in Fig. 5.9, we plot in Fig. 5.10 the simultaneous (normalized) distributions of the signal and the main ($t\bar{t}$) background in the $\Delta|\eta(\ell)|/\Sigma|\eta(\ell)| - \Delta p_T(\ell)/\Sigma p_T(\ell)$ plane, where

$$\begin{aligned} \Delta|\eta(\ell)| &= |\eta(\ell^+)| - |\eta(\ell^-)|\,, & \Sigma|\eta(\ell)| &= |\eta(\ell^+)| + |\eta(\ell^-)|\,, \\ \Delta p_T(\ell) &= p_T(\ell^+) - p_T(\ell^-)\,, & \Sigma p_T(\ell) &= p_T(\ell^+) + p_T(\ell^-)\,. \end{aligned} \tag{5.2}$$

As it can be seen in the figure, a sizable asymmetry in the signal can be constructed by comparing events in the first and third quadrants. Thus we propose the following asymmetry

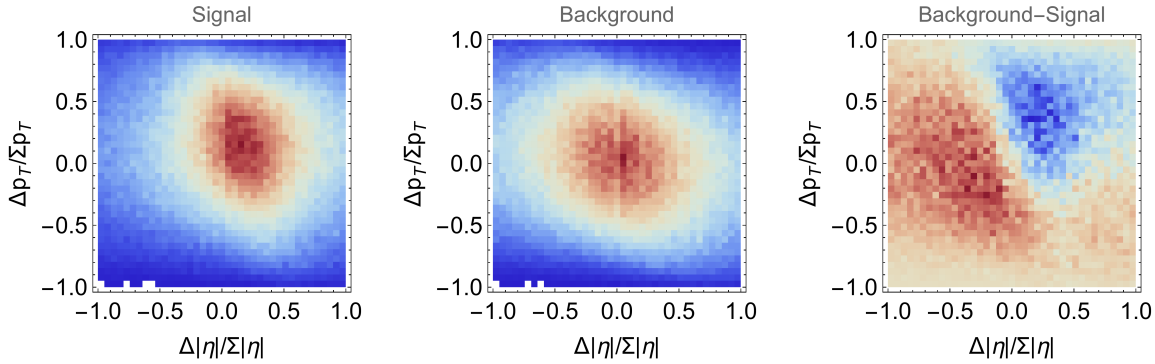

Figure 5.10: Density plot of normalized event distributions of the signal (left) and the main background $t\bar{t}$ (center) in the $\Delta|\eta(\ell)|/\Sigma|\eta(\ell)|$ versus $\Delta p_T(\ell)/\Sigma p_T(\ell)$ plane. In the right panel we show the difference between the two distributions, which demonstrates that (compared to the almost symmetric background) signal events are predominantly in the 3rd quadrant of the plot, whereas they are missing in the 1st quadrant. This correlation between the plotted variables points out that an asymmetry between these quadrants would be useful to enhance signal over background.

$$A(\eta, p_T) = \frac{N^+ - N^-}{N^+ + N^-}, \tag{5.3}$$

where

$$N^{\pm} = N\left(\Delta|\eta(\ell)| \gtrless 0 \,\&\, \Delta p_T(\ell) \gtrless 0\right), \tag{5.4}$$

as a $|V_{td}|$ sensitive observable.

It is interesting to understand how the different processes contribute in $A(\eta, p_T)$. It is clear that the denominator is dominated by $t\bar{t}$, whose cross-section is considerably larger than the others, even after the selection cuts. On the other hand, the numerator is more involved because each i-th process contributes with

$$N_i^+ - N_i^- = \sigma_i \cdot A_i \cdot \epsilon_i \cdot A_i(\eta, p_T), \tag{5.5}$$

where the factors in the RHS are the cross-section, acceptance, selection efficiency[4] and asymmetry, respectively, all restricted exclusively to the i-th process. Since $t\bar{t}$ has a small NLO charge-asymmetry, but a large cross-section, it ends up being important for the $r \approx 1$ region, but becomes sub-leading as $r \gtrsim 10$. We expect a similar NLO asymmetry for $tW(b)$, but since its cross-section is much smaller than $t\bar{t}$ we can neglect it in the numerator. Other backgrounds such as WWj, tj and $Z/\gamma^* j$ have a non-negligible asymmetry, but their product $\sigma_i \cdot A_i \cdot \epsilon_i$ suppresses any contribution to the numerator.

5.1.4.2 Other asymmetries

Given the distributions in Fig. 5.9 one could consider alternative definitions of asymmetries to enhance the signal over the backgrounds. We have tested many of them bearing in mind that we need to exploit the lepton charge asymmetry present in the signal. In the following paragraphs, we explain the main ones and why they do not improve the significance of the asymmetry defined in Eq. 5.3.

The most interesting attempt consists of taking the asymmetry $A(\eta, p_T)$ with a cut in $|\eta_{\ell^-}| \gtrsim 1.5$ since we expect to have an enhanced asymmetry in the forward region. Indeed this selection increases the absolute value of the asymmetry, but reduces the acceptance due to the additional cut. Moreover, this also creates an artificial asymmetry in the backgrounds which reduces the sensitivity to the signal. Together, this results in larger statistical (and also presumed systematic) uncertainties and consequently reduced significance when compared to $A(\eta, p_T)$. On the other hand, imposing a symmetric cut on $|\eta_{\ell^-}|$ and $|\eta_{\ell^+}|$ keeps the backgrounds symmetric but does not increase the signal asymmetry sufficiently to offset the reduction in the acceptance.

The last case we discuss is the asymmetry based solely on $|\Delta\eta|$, with and without cuts on η, that is

$$A(\eta) = \frac{N\left(\Delta|\eta(\ell)| > 0\right) - N\left(\Delta|\eta(\ell)| < 0\right)}{N\left(\Delta|\eta(\ell)| > 0\right) + N\left(\Delta|\eta(\ell)| < 0\right)}. \tag{5.6}$$

In this case the total number of accepted events increases and therefore the statistical uncertainty decreases. However, the absolute value of the asymmetry decreases because $\Delta|\eta|$ alone has less discriminating power than $\Delta|\eta|$ and Δp_T together (see right panel in Fig. 5.10). The combination of these two features yields smaller significance than $A(\eta, p_T)$. While this asymmetry is also sensitive to cuts in η, we have found that their application does not improve the significance.

[4] Selection efficiency refers to the fraction of events that pass the selection cuts to be either $N^{\pm}$.

5.1.5 Results

For our final quantitative analysis and estimation of the experimental reach, we have simulated the signal and the main backgrounds using `MadGraph5_aMC@NLO` [61], interfaced with `Herwig` [77, 78] (for $t\bar{t}$) and `Pythia8` [79, 80] (for all other processes) for showering and hadronization. The $t\bar{t}$ has been simulated at NLO in QCD to account for its non-vanishing charge asymmetry. The higher order QCD effects in the other relevant processes have been accounted for through the effective k-factors. In particular, $k_{tW(b)} = 1.35$ [81] and we assume the same k-factor for the signal.[5] The same procedure was used in the previous sections, where however only parton level results were utilized. Finally, we have simulated detector effects using `Delphes` [83]. The jets have been clustered using the anti-kt algorithm with $R = 0.6$. A 'loose' b-tagging algorithm working point has been used with a reference selection efficiency of 0.8 and a rejection factor for light jets of 100 [83, 84]. The remaining Delphes parameters have been left in the default ATLAS tune.

In all the simulations we have used $m_t = 173$ GeV. We have used the `nn23lo1` PDF for LO processes and `nn23nlo` PDF for NLO simulations [85]. All the simulations have been preformed using the dynamical factorization and renormalization scales as implemented in MadGraph5 version `MG5_aMC_v2_5_3` original tune.

We have performed the selection of events defined at the end of Sect. 5.1.4. We have checked the sensitivity of the selection cuts on the event reconstruction parameters and found that the jet veto depends quite sensitively on the jet clustering algorithm. In particular, it becomes less efficient for narrower jets.

In Table 5.2 we show how the signal and the main backgrounds behave upon detector effects and selection cuts for the above described event reconstruction and selection. Using the fifth and the last column one can visualize the importance of each contribution to the denominator and the numerator of the asymmetry defined in Eq. (5.3), respectively. In Fig. 5.11 we plot the resulting charge asymmetry $A(\eta, p_T)$ defined in Eq. 5.3 with all the detector level simulations included. One can see that the $t\bar{t}$ asymmetry dominates for $r = O(1)$ (close to the SM), but as r increases the negative contribution from the signal starts to dominate.

To quantify the versatility of the proposed charge asymmetry we have studied the prospective experimental reach in the NP parameter r by computing the difference of $A(\eta, p_T)$ to its SM expectation in units of the uncertainty. In addition to the statistical uncertainty we have included an estimation for the systematic uncertainty $\Delta_{syst} = 0.2\%$, based on a similar analysis in the di-lepton charge asymmetry performed by CMS in Ref. [86] and the expected usual improvement in the knowledge of the detector and other systematic effects with increasing luminosity. In our analysis Δ_{syst} acts as an overall estimation of all the systematic uncertainties. By adding

[5] We note that in a 5-flavor PDF scheme the QCD corrections to both processes are identical, the difference being purely in the PDFs. We also note that at NLO the signal and the $tW(b)$ background mix with the LO $t\bar{t}$ process and strategies exist for separating these with small remaining interference [82]. Unfortunately, exact NLO results and simulations of our signal are at present not publicly available and go beyond the scope of our work.

process	$\sigma \cdot B$ [fb]	$A(\ell^+\ell^- b + X)$	ϵ	$\sigma \cdot B \cdot A \cdot \epsilon$ [fb]	$A_i(\lvert\Delta\eta\rvert, \Delta p_T)$	$\sigma \cdot B \cdot A \cdot \epsilon \cdot A_i$ [fb]
signal	$1.2\,r^2$	0.17	0.16	$0.034\,r^2$	-0.2	$-0.0067\,r^2$
$t\bar{t}$	3.1×10^5	0.56	0.011	200	0.003	0.57
$tW(b)$	1.8×10^3	0.25	0.07	34	$O(10^{-3})$	$O(10^{-2})$
$Z/\gamma^* j$	5.1×10^5	0.002	4.7×10^{-4}	0.53	-0.10	-0.05
WWj	1.5×10^3	0.002	0.14	0.52	-0.06	-0.03
tj	1.7×10^4	1.2×10^{-5}	0.29	0.0062	-0.8	-0.02

Table 5.2: The relevant processes upon detector acceptance and selection cuts. A refers to the detector acceptance of $\ell^+\ell^- b$ plus anything else. Selection efficiency ϵ includes a veto on events with extra jets, cuts in E_T^{miss} and $m_{\ell\ell}$, and also a selection of events only in the first and third quadrants in $\Delta|\eta|$ and Δp_T, as defined in Eq. (5.4). The column '$\sigma \cdot B \cdot A \cdot \epsilon$' is relevant for the denominator of the total asymmetry and is dominated by $t\bar{t}$ and a small correction by $tW(b)$. A_i refers to the asymmetry defined in Eq. (5.3) for the corresponding row, constructed with the detector level events that pass all acceptance and selection requirements. Finally, the last column is relevant for the numerator of the total asymmetry and is dominated by $t\bar{t}$ for $r \lesssim 10$ and by the signal for $r \gtrsim 10$.

statistical and systematic uncertainties in quadrature, we define the significance as

$$\text{significance} = \frac{\left|A(\eta, p_T) - A(\eta, p_T)^{SM}\right|}{\sqrt{(N^+ + N^-)^{-1} + \Delta^2_{syst}}}. \tag{5.7}$$

In Fig. 5.12 we plot contours of expected significance in measuring $A(\eta, p_T)$ as a function of r and the luminosity. In order to further differentiate between the small signal and the overwhelming $t\bar{t}$ background, existing experimental analyses [73–75] of tW associated production at the LHC, in addition to basic selection cuts similar to the ones described above, employ more elaborate multivariate techniques, such as boosted decision trees or neural networks. With the rapid development of machine learning, these methods are expected to be further refined in the near future and also extremely useful for the processes and observables studied here. As a rough estimation, and motivated by Ref. [73], we include in Fig. 5.12 (in red dashed line) an estimation of the significance for the case where the $t\bar{t}$ background could be reduced by a further factor of 1/2 with negligible effect on the signal.

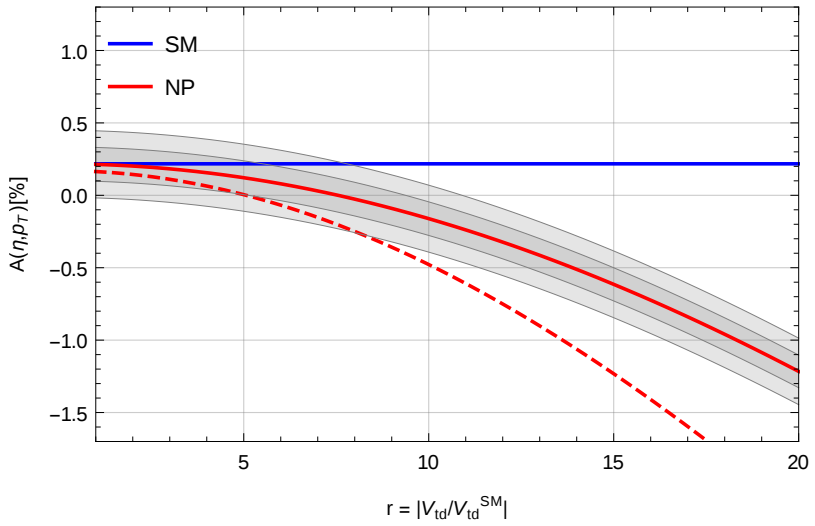

Figure 5.11: Expected value of the asymmetry $A(\eta, p_T)$ (solid red) as function of the NP parameter $r = |V_{td}/V_{td}^{SM}|$. Shaded area represents statistical (darker) + assumed systematic (lighter) uncertainties ($\pm 1\sigma$) with the event selection indicated in text at the prospective LHC luminosity of $L = 3000$ fb^{-1}. Blue line represents the SM value of the asymmetry, which is mainly due to NLO QCD effects in $t\bar{t}$. Also shown (in dashed red) is an estimation of the asymmetry assuming a reduction of the dominant $t\bar{t}$ background by half (see text for details).

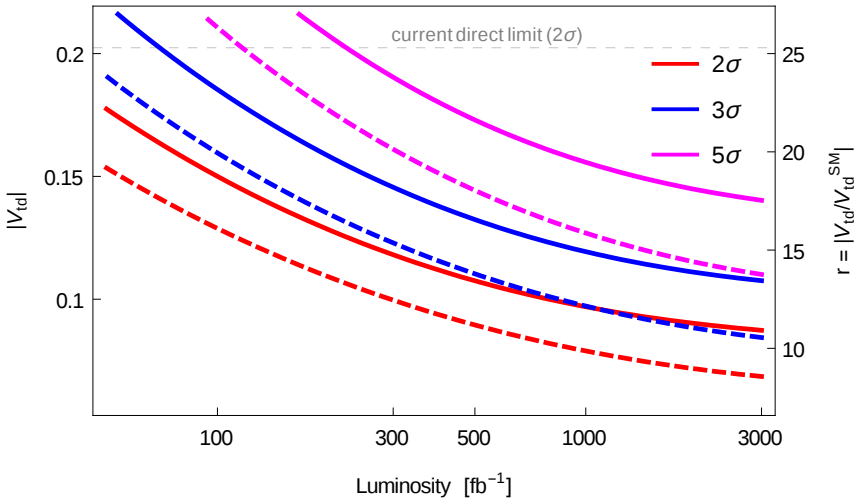

Figure 5.12: Contour lines for the 2σ, 3σ and 5σ measurement of $|V_{td}|$ parameterized as a function of $r = |V_{td}/V_{td}^{SM}|$ and the LHC luminosity. Dashed lines correspond to the estimation of the same analysis assuming a further reduction of the $t\bar{t}$ background by half (see text for details).

We observe that in using the proposed charge asymmetry $A(\eta, p_T)$ in the leptonic tW final state, an improvement in the direct bound on $|V_{td}|$ (r) compared to existing constraints is possible already with the existing LHC dataset. Furthermore, values of $r < 10$ could be directly accessible at the (HL)LHC, improving the existing best direct constraints by roughly a factor of three. A

further significant improvement would however require a reduction of systematic uncertainties below the per-mille level.

5.2 V_{td} at (HE)LHC

We performed the same analysis now at 27 TeV, which is the next step in energy in the LHC. Fig. 5.13 shows the contours of expected experimental significance for $A(\eta, p_T)$ (and r) as functions of luminosity, for 13 TeV and 27 TeV LHC. As a rough guidance we also show with dashed lines the significance for the case that the dominant $t\bar{t}$ background were further reduced by a factor of 2, e.g., by using multivariate discrimination techniques as already done in existing single top analyses [73, 75]. Values of $r < 10$ could be directly accessible at the LHC@13TeV, improving the existing best direct constraint [42] by roughly a factor of three. The current direct bound on V_{td} can be surpassed with the Run 2 dataset, while with $3000 fb^{-1}$ it could be possible to probe $V_{td} \sim V_{ts}^{SM} \simeq 0.04$.

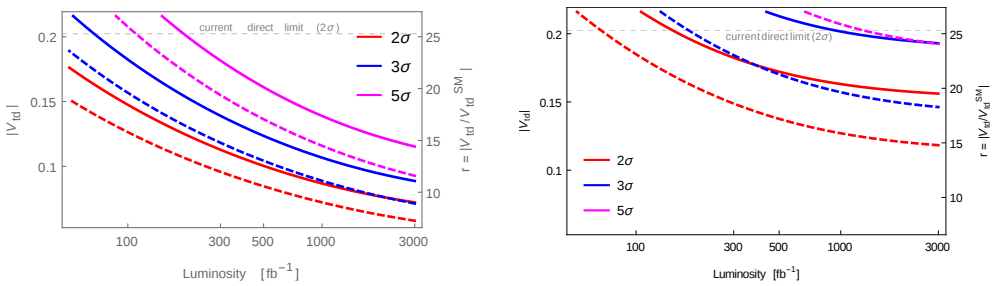

Figure 5.13: Contour lines for the 2σ, 3σ and 5σ measurement of $|V_{td}|$ parameterized as a function of $r = |V_{td}/V_{td}^{SM}|$ and the LHC luminosity. 7 TeV in the left and 27 TeV in the right. Dashed lines correspond to the estimation of the same analysis assuming a further reduction of the $t\bar{t}$ background by half.

The dominant $t\bar{t}$ background is mostly generated via gluon fusion, which is charge symmetric. There are subleading contributions from processes like $u\bar{u} \to t\bar{t}$ which are charge asymmetric, but only enter at higher orders in QCD. This is the main reason the dominant $t\bar{t}$ background has a strongly suppressed charge asymmetry. At higher collision energies, the probability of finding energetic enough gluons in the proton increases faster than that of valence quarks. Consequently, the fraction of $t\bar{t}$ events from the quark-antiquark initial state is reduced [87]. This leads to a shrinking charge asymmetry with growing collision energy. Unfortunately, the same happens to the signal, this time because at higher energies the asymmetry between d and $\bar{d}$ partons inside the proton is reduced. The net effect is a severely diminished significance at 27 TeV compared to 13 TeV for comparable luminosities.

On the other hand, at 7 TeV the significance does increase and with $3000 fb^{-1}$, values of $r < 10$ could be accesible with 3σ and values of $r \sim 10$ with 5σ. This effect is due, of course, to the

fact that at lower energies the imbalance between quarks of valence and those in the sea of the proton is higher, as mentioned before.

5.3 tj background as the signal

So far in this chapter we presented the process $gd \to tj$ as a good signal to measure V_{td}, but now we propose to use one of its backgrounds, $ud \to tj$ as a signal and perform another analysis to enhance it. This process has a background, $ub \to tj$, which has a lower production rate but at the same time has a CKM matrix element $V_{tb} > V_{td}$. This discussion has been given in Sect. 5.1.1, where we argued that the main problem is that this background is also charge asymmetric, so that it was not a good choice for a signal. In this section we propose another strategy to measure V_{td} using tj.

We are interested in the processes tj and $\bar{t}j$ due to their kinematical features that gives them different cross section. The main background is $t\bar{t}$, which is a symmetric process. We propose a method to get rid of this symmetric background which does not rely on charge asymmetry and that could allow us to diminish systematic uncertainties.

The signal, with V_{td} vertex, is $ud \to jt$ ($\bar{u}\bar{d} \to j\bar{t}$), see Fig. 5.14, so we expect to detect a jet and a $t/\bar{t}$ decaying into ℓ and b, i.e. one j, one $b-jet$, one lepton and MET. In order to be considered detected at the LHC, this implies to see a jet with $\eta_j < 5$, a jet b tagged of $\eta_b < 2.5$, and lepton with $\eta_\ell < 2.5$, all of them with $p_T > 25$GeV.

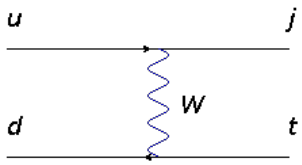

Figure 5.14: Process $ud \to jt$ ($u\bar{d} \to j\bar{t}$)

We consider three main backgrounds, $t\bar{t}$, Wjj and $ub \to jt$ and its conjugate.

The first background we need to analyse is the process with b instead of d in the diagram, see Fig. 5.15. This process is diminished by the fact that b is not of valence, but is enhanced because $V_{tb} >> V_{td}$. In this case, the particles produced are the same as with the signal but, since the b is not of valence, we have kinematical differences which are of great interest if we consider the distributions in β_z, the relativistic velocity of the whole system in the z axis.

There is also the process $us \to tj$, that we have not mentioned yet. But this process will be neglected, since s is not a valence quark nor do we expect V_{ts} to be a large number. It is left for a future work to perform an analysis looking for V_{ts}^{NP}.

There are two other important backgrounds, $t\bar{t}$ and Wjj family, see Fig. 5.16. The first needs, in order to get mistaken as our signal, to have a jet mistagged as a b and one lost lepton. We consider both the leptonic and the semileptonic decayment. The second one is a family which

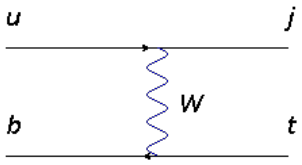

Figure 5.15: Process $ub \to jt$ ($u\bar{b} \to j\bar{t}$)

includes Wjj with j a light jet, Wcc where c is a charm-jet, Wbb with b a b-tag jet, and all the mixtures. In the case of Wjj and Wcc it needs to have a jet mistaken as a b-jet, in the case of Wbb, it needs to have a not b-tagged jet.

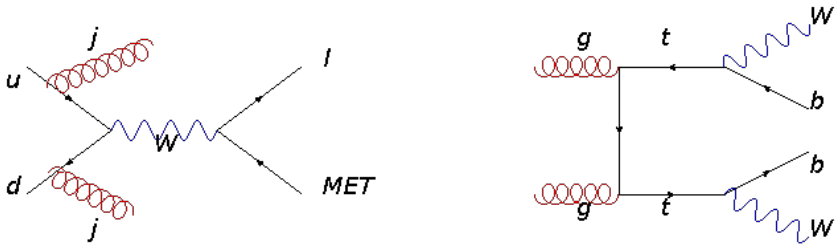

Figure 5.16: Background processes Wjj and $t\bar{t}$.

Let us write the difference of cross section between processes with a ℓ^+ and ℓ^-, $\Delta\sigma$, as

$$\Delta\sigma = \frac{\Delta N^{(V_{td})} + \Delta N^{(V_{tb})} + \Delta N^{(others)}}{\epsilon L}, \tag{5.8}$$

where $\Delta N^i = N^i_+ - N^i_-$, with $N^i_\pm$ the number of events corresponding to the i-th process with $\ell^\pm$, i the corresponding processes, and ϵ is the efficiency. The quantity $\Delta\sigma = \sigma(tj) - \sigma(\bar{t}j)$ has large sources of systematic uncertainties, mainly from the efficiency ϵ and luminosity L. We perform this analysis looking for a way to get rid of them.

The number of particles detected for a background i is $N^i = \sigma^i A^i \epsilon L$, where A is the acceptance and we have $N^i = \sigma^i A^i \epsilon L r^2$ with $r = \frac{V_{td}}{V_{td}^{SM}}$ for the signal (because the process contains V_{td}). We consider the acceptance A to be the coefficient that measures what fraction of the total simulated events can actually be detected (after cuts are applied). This can change from process to process. But there is also the efficiency ϵ, which we define as the fraction of particles which are correctly interpreted at the detector and not mistagged as another one. This comes from the parameter of Delphes and it is the same for all processes.

The process $t\bar{t}$ is symmetric, so we do not expect contribution to the numerator in Eq. 5.8, but it does contribute to the statistic uncertainty. We consider the uncertainty on each N^i as poissonian.

The goal of this work is to measure $\Delta\sigma^{(V_{td})}/\Delta\sigma^{(V_{tb})}$, since because the efficiency and luminosity are gone with the ratio, then we get rid of the systematic uncertainties to measure V_{td}/V_{tb}. Thus we need as many equations as number of processes we have. Instead we propose to use this

Process	$\sigma[pb]$	σB [pb]	ϵA	$\sigma B \epsilon A$
$pd \to tj$	$0.021 \cdot r^2$	$0.0042 \cdot r^2$	0.009	$3.9r^2 \cdot 10^{-5}$
$p\bar{d} \to \bar{t}j$	$0.0064 \cdot r^2$	$0.0013 \cdot r^2$	0.012	$1.5r^2 \cdot 10^{-5}$
$pp \to tj(5F)$	107	21.4	0.0095	0.20
$pp \to \bar{t}j(5F)$	60	12	0.01	0.13
$pp \to W^+jj$	9550	1910	$3 \cdot 10^{-6}$	0.006
$pp \to W^-jj$	6665	1333	$4 \cdot 10^{-6}$	0.005
$pp \to t\bar{t}$ (di)	504.7	20.2	0.0018	0.037
$pp \to t\bar{t}$ (semi)	504.7	141.316	0.0005	0.07

Table 5.3: Cross sections of signal and backgrounds. The first two rows include not null V_{td} and the ones indicated with 5F refers to process with b in the sea of the proton. For Wjj processes we imposed a cut in $\eta_j < 5$ in order to avoid divergencies and the ϵA numbers are multiplied by a factor of 0.01 due to the mistagg of the jet.

method with Eq. 5.8 and perform a template-fit, which will allow us to get as much information as bins we have in the distribution.

We construct a histogram of β_z for each process tj and each $\bar{t}j$, we normalize it by asking unitary area and get the distribution D_i of the process. We perform the substraction $\Delta N = N_{tj} - N_{\bar{t}j} = (\sigma_{tj} D_{tj} A_{tj} - \sigma_{\bar{t}j} D_{\bar{t}j} A_{\bar{t}j}) \epsilon L$ for signal and backgrounds and normalize the ΔN distributions.

We divided the β_z region in Fig. 5.17 in three regions: $\beta_z < 0.4$ (region I), $0.4 < \beta_z < 0.8$ (region II) and $0.8 < \beta_z < 1.0$ (region III). We measure $\Delta N(I, II, III)$ in both regions and, from Montecarlo, we predict which is the fraction $D_{i,j}$ in each region (bin) coming from V_{td}, V_{tb} and wjj. Processes w plus heavy quarks are more important, since c and b get tagged at a much higher rate than one in a hundred. We took wjc as the representant of the group because of this and because of its larger cross section.

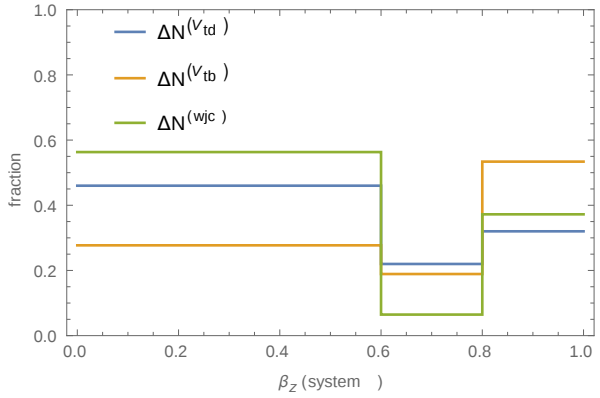

Figure 5.17: Normalized histogram for the signal with the v_{td}, V_{tb} and wjc.

The coefficients satisfy the relation $\sum D_i = 1$ for each process since the histogram is normalized and we define $a_i = D_i A$, so that a_i is the acceptance in each bin and we have a system of equations,

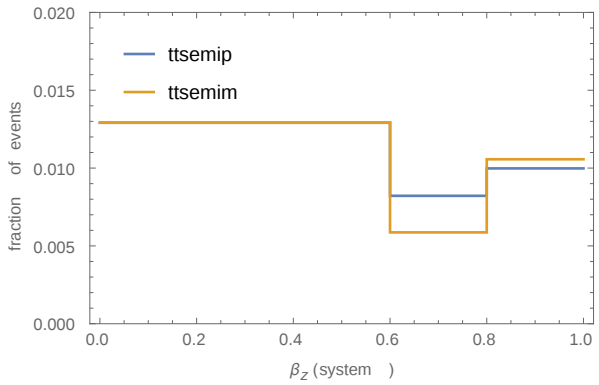

Figure 5.18: Histogram for the tt process, with semileptonic decay.

$$\begin{aligned}
\Delta N(I) &= a_{I,d}\Delta N^{(V_{td})} + a_{I,b}\Delta N^{(V_{tb})} + a_{I,w}\Delta N^{(wjc)}, \\
\Delta N(II) &= a_{II,d}\Delta N^{(V_{td})} + a_{II,b}\Delta N^{(V_{tb})} + a_{II,w}\Delta N^{(wjc)}, \\
\Delta N(III) &= a_{III,d}\Delta N^{(V_{td})} + a_{III,b}\Delta N^{(V_{tb})} + a_{III,w}\Delta N^{(wjc)}.
\end{aligned}$$

This is a 3x3 system from which we can extract the required quantities $\Delta N^{(V_{td})}$ and $\Delta N^{(V_{tb})}$. To perform the template fit, we considered the signal and the backgrounds which are assymetric, since they can contribute to $\Delta\sigma$, yet we did not include $t\bar{t}$ being symmetric but it is of main importance since its uncertainty does contribute. We make the histograms for $t\bar{t}$ events (see Fig. 5.18) in the following way. We do not want to calculate coefficients because ΔN^{tt} could be negative (its mean value being zero), so we just multiply by its cross section and then divide by the total number of events, so the number in each bin given by the histogram is cross section times acceptance. This quantity is substracted from the total ΔN when propagating the uncertainties. We assigned to $a_{i,j}$ a systematic uncertainties of 0.01%.

In real life, it is possible to measure the values corresponding to ΔN and, giving the a_i parameters that we know from MonteCarlo, we can fit the functions to get the values of $\Delta N^{(V_{td})}$ and $\Delta N^{(V_{tb})}$.

5.3.1 Selection cuts

For our quantitative analysis and estimation of the experimental reach, we have simulated the signal and the main backgrounds using `MadGraph5_aMC@NLO` [61], exactly as explained in Sec. 5.1.5. All the processes were considerated at leading order for simplicity, as a first approximation. We used a c-jet missing rate of 0.25 and a b-jet missing rate of 0.85.

The signal results in a $\ell jb E_T^{miss}$ final state so we took the following selection of events to suppress the backgrounds:

- Select events with ℓbj, with $|\eta(\ell, b)| < 2.5$, $|\eta(j)| < 4.5$ and all with $p_T > 30$ GeV.

- Veto events with $E_T^{miss} < 30$ GeV
- Ask for 160GeV $< m(\ell\nu b) <$ 180GeV and $m_T(\nu,\ell) > 50GeV$

The last item is required considering that the lepton, the b-jet and the MET all from a t quark and $m_T(\nu,\ell) > 50GeV$ is needed to suppress QCD multijet background.

To reconstruct the invariant mass of b, ν and ℓ we took the MET and the impulse coming from the lepton, took the $p_z(\nu)$ with smaller absolute value, and calculated the invariant mass of the lepton, the neutrino and the b-jet. For details, see appendix B.

5.3.2 Results

Once we perform the analysis of the previous subsections, we can invert Eqs. 5.9 and, knowing the value of ΔN and that of ΔN^{tt}, get the values for ΔN^i. We now have all the elements necessary to calculate the ratio $\Delta\sigma^{(V_{td})}/\Delta\sigma^{(V_{tb})}$ and the standard deviation. For $r = 20$ and a luminosity of $300fb^{-1}$, we get a $\sigma = 1.2$, which is not bad but is not better than the method proposed at the beginning of this chapter. At $3000fb^{-1}$, we get a $\sigma = 3.8$ which is much more interesting and could be tested at the (HL)LHC.

CHAPTER 6

Z'-EXPLORER SOFTWARE

This chapter introduces Z'-explorer , a software designed to calculate the strength that a theoretical Z' neutral particle coupled to SM particles would show if measured at the LHC@14TeV. Z'-explorer only requires the couplings or the widths to the daughter particles and the mass, and it returns the strength for each considered decay channel. It is written in C++ and created for a Linux environment. As an application, we perform a phenomenologic study of the strengths of a neutral boson from the simplified warped composite theory, and find the parameters of the model where the most sensitive channel is allowed by experiments.

6.1 Introduction

The objective of this work is to develop a tool which can be used to test against current experimental results any model predicting a Z' particle [88]. One of the main objectives pursued in this work is to create a very simple tool which could be learned and used rapidly to explore parameter space while constructing NP models or exploring pure Z' phenomenology. The only input required to test a Z' model from this phenomenological point of view would be its couplings and/or branching ratios to the allowed decaying channels.

Because of the Z' quantum numbers, its possible decay channels explored at the LHC and their corresponding latest results are jj [89–91], $b\bar{b}$ [92], $t\bar{t}$ [93, 94], e^+e^- [95, 96], $\mu^+\mu^-$ [95, 96], $\tau^+\tau^-$ [97, 98], W^+W^- [99, 100], Zh [100]. Since testing all these channels while constructing a model it is cumbersome, we study in this manuscript a new tool which would facilitate this enterprise.

To tackle this problem we observe that each decay channel has different sensitivity not only because of the specific detector and experimental techniques to reconstruct each particle, but

also because of the different SM backgrounds affecting each final state, and because all of these depend on the mass of the sought Z'. Although all these features for each channel are individually complex, and still more when combined, their relevant features are summarized in the exclusion plots presented by the experimental groups in each search. We show that using this information we can estimate in a reasonable way whether a point in parameter space in a Z' NP model is excluded or not, and which of the above is the most sensitive channel. On this basis, along this work we present the software *Z'-explorer* which can make the mentioned computation automatically in a very simple manner and for a huge amount of points in parameter space.

Z' decay modes and branching ratios depend on the specific NP model. Z' decay to dijets depends on the coupling to quarks, but its branching ratios also depends on the Z' coupling to all other particles The search of a Z' at the LHC, as for any other NP particle, is implemented in different decay channels. At the LHC, searches have been performed both by the CMS and the ATLAS Collaborations, and have superseded the results coming from searches in other colliders such as Tevatron in most of the TeV scale [101].

Although the fraction of times a Z' decays to a given channel depends solely on its corresponding branching ratio, in experimental terms the acceptance and efficiency of the detector and the background of this channel are crucial to determine its exclusion/discovery sensitivity. These features also have an important dependence on the scale of energies considered, which depends on the sought resonance mass. For instance, for the search of a Z' with $M_{Z'} \lesssim 1$ TeV at the LHC, we expect the dijet channel to have large QCD background, which dominates at low p_T. Whereas in the dilepton channel, the background is smaller in comparison, and thus the signal is likely cleaner and the channel more sensitive even though its branching ratio could be smaller. Moreover, since $\mu^+\mu^-$ channel has slightly more efficiency than e^+e^-, for equal branching ratios we can expect more sensitivity in $\mu^+\mu^-$. Considering also the W^+W^- decay mode, for the same above reasons the fully hadronic decay is hidden in QCD background, whereas the leptonic decays, although cleaner, are difficult to reconstruct due to missing energy. This scenario changes for larger masses, $M_{Z'} \gtrsim 2$ TeV. In such a case there is a more subtle interplay between the features discussed above. Not only because all backgrounds are highly reduced, but also because the techniques for detecting and reconstructing particles are also modified. In particular, in this high p_T regime, boosted massive particles, such as W boson or t quark, can decay in configurations where all particles are collimated in a single fat jet in the lab frame. This, in conjunction to a reduced QCD background yields a favorable enhancement for channels such as hadronic W and top.

From this overview on some of the features involved in determining which is the best channel to exclude (or find) a given Z', we see that there are a variety of non-trivial ingredients which affect which channel could be the most sensitive. It is of particular interest for our work to find a magnitude that condenses all the relevant information and provides an estimation on the sensitivity of each channel for each point in parameter space in a given NP Z' model.

From the phenomenological point of view, the information available on previous experimental searches in the different channels at a given energy and luminosity can be incorporated into the determination of the most sensitive decay channel, through the extraction of the predicted experimental limits. All these features are condensed in the strength (S), already defined in Chap.4,

$$S = \frac{\sigma_{pred}}{\sigma_{lim}} \tag{6.1}$$

where σ_{pred} is the predicted cross-section times branching ratio times acceptance of the new Z', and σ_{lim} is the corresponding predicted experimental upper limit at the 95% CL. The difference in using *predicted* instead of *measured* limits consists in considering the experimental techniques instead of eventual fluctuations in the data. In case the measured limit departs significantly from the predicted value, it would correspond to a discovery or a wrong prediction which in both cases should be addresses from another point of view.

6.2 Running

Z'-explorer software is built on `C++` and was only tested for Linux environments, although it may run in others. Inside the main folder `Z'-explorer` we will find another folder named `lib`. We need to compile and so we go to a terminal in `Z'-explorer` and do

```
> cd lib
> cd make
```

We have now an executable file `program.out`. We are able to run Z'-explorer . But first, we need to set the input card. This is a table with 23 columns and as many rows as desired, where the columns are separated by space and must contain

```
M guuL guuR gddL gddR gccL gccR gssL gssR gbbL gbbR gttL gttR geeL geeR
gmumuL gmumuR gtautauL gtautauR Ginv Gww Ghz Gxx
```

being `M` the mass of the Z' boson, `giiL,R` its coupling to the pair of i fermions left (right), except neutrinos, and `Gij` the decay width to the i and j particles. Couplings to fermions corresponds to a lagrangian of the form of Eq. 3.61. We require the information about the couplings to bosons as *partial width* since there is not a unique Lorentz structure in their couplings. The total width to non SM particles can be added in the computation as Γ_{xx}. It should be recalled that the Γ_{inv} width is the invisible decay and if one take it as the decay to neutrinos, a factor of 3 should be added since there are three families of neutrinos.

This input card should be named `card_1.dat` and be placed in the folder `input_cards`. Once this is done, we go back to the terminal and run the program as

```
> cd ..
> ./program.out
```

The program should run OK and when it finishes there should be a new file name `1.dat` in the `output` folder which contains the inputs from `card_1.dat` and the strength for each channel, for every line. It has the following columns

```
M guuL guuR gddL gddR gccL gccR gssL gssR gbbL gbbR gttL gttR geeL geeR
gmumuL gmumuR gtautauL gtautauR Ginv Gww Ghz Ghh Sjj Sbb Stt See
Smumu Stautau Sinv Sww Shz Sxx
```

Observe that the `Sxx` is left as a dummy variable to eventually add new possible Z' channels in the future.

The program runs very fast and using negligible CPU resources. Since each row in the input file is a different point in the parameter space for Z'-explorer, output card contains the same number of rows of data than `card_1.dat`. The running time depends on this number of rows and the CPU speed, but typically for an input card of 1000 reference points, time is less than 2 seconds.

Additionally, after running, in the `/extra` folder and in different files are available the estimated decay widths, branching ratios, the estimated σ_{pred} and the extracted σ_{lim} for each reference point in the input card. More details on these auxiliary files can be found in the `README` file.

6.3 How does it work

With the couplings provided in the incard, Z'-explorer is able to compute the widths to fermions using relations 3.63. Including the widths to bosons provided also by the user in the incard, Z'-explorer calculates the branching ratios to the ten channels, jj, bb, tt, ee, $\mu\mu$, $\tau\tau$, WW, hZ, xx and the invisible decay. The total production cross section is obtained by simulating the production processes in `MadGraph` and creating a discrete list where for each mass of Z' there is a cross section (see Sect. 6.4). Z'-explorer performs the product between the branching ratios and the total cross section in order to have the cross section corresponding to each channel. Once this is obtained, these predictions for each possible final state are compared to the corresponding 95% upper limit on the product of the cross section times branching fraction, coming from the most sensitive searches performed both by the ATLAS and CMS collaborations (see Sect. 6.5). The comparison is made through the calculus of the aforementioned strength S, explained in the previous section.

6.4 Simulations cards

As mentioned before, Z'-explorer uses cards with cross sections simulated using `MadGraph@14TeV`. To perform the simulations, we generated the processes $q\bar{q} \to Z'$ where $q = u,d,s,c,b$ are the quarks in the proton+valence sea, using a tailored Z' model which couples with unity to only one quark in the proton each time and for a set of values of $M_{Z'}$ between 0.4 and 8.1 TeV, with a step of 0.01 TeV, and at $\sqrt{s} = 13$ TeV. Since LHC protons are unpolarized we set same couplings for Left and Right chiralities at this level. These calculus, stored in the repository as `/cards/sim_cards`, are used during program execution: the predicted production cross section $\sigma_q(M_{Z'})$ for an specific reference point is the sum of the five contributions of quarks (u, d, c, s and b). Each of them adjusted by the sum of the corresponding squared chiral couplings, that are extracted from the input card. This general formula is given by

$$\sigma_{sim}(M_{Z'}) = \sum_q \left(g_{qR}^2 + g_{qL}^2\right) \frac{\sigma_{sim,q}(M_{Z'})}{2}, \tag{6.2}$$

where g_{qL} and g_{qR} are the couplings of Z' to q_L and q_R respectively and σ_{sim} is the total production cross section. It is posible to perform this separation of parton cross section because the feynmann diagram of the production do not interfere. The software selects inside the simulations the record with the mass $M_{Z'}$ that is closest to the one in the input card at the corresponding reference point. The total production cross section is then used in each possible decay channel to compute the σ_{pred} needed in Eq. 6.1, multiplying by the corresponding branching ratio, which is calculated by the program using the input parameters.

There are in total five simulated cards, one for each quark in the proton+valence sea. These can be found in the folder `cards` and can be replaced by anothers if the users wishes so. They contain two columns, one for the mass of the boson and one for the cross section. To know the correspondence between card number and quark, see Table 6.1.

#card	1	2	3	4	5
quark	u	d	c	s	b

Table 6.1: Correspondance between number of sim card and quark in the proton+valence sea

6.5 Experimental cards

The experimental limits used by the program, corresponding to the value of σ_{lim} required in Eq. 6.1, are stored in `/cards/exp_cards`. The searches included in the program, performed by both ATLAS and CMS collaborations and considering the latest results up to date, include the following channels and references: jj [89], $b\bar{b}$ [92], $t\bar{t}$ [93], e^+e^- [95], $\mu^+\mu^-$ [95], $\tau^+\tau^-$ [97], W^+W^- [99], Zh [100]. We use the digitalization [102] of the numerical values of 95% upper limits on the product of the cross section and the branching fraction versus $M_{Z'}$ from the corresponding

published plots. It is worth noticing that since searches are constantly updated, the user can modify the experimental limits for a given channel just by modifying the corresponding `exp_card` and propose the update of the repository. The program includes a `README` file in which the numeric labeling of `exp_card` for each channel is displayed.

To know the correspondence between card number and decay particles (daughters), see Table 6.2.

# card	1	2	3	4	5	6	7	8	9	10
daughters	jj	bb	tt	ee	$\mu\mu$	$\tau\tau$	inv	ww	hz	xx

Table 6.2: Correspondance between number of exp card and decay particles.

6.6 Testing Z'-explorer on a warped-composite model

In this section, we test the Z'-explorer software using the theory developed in Chapter 3. All new Z_i's could be in principle easily tested through Z'-explorer once the corresponding couplings are explicitly written. We work out as an example the phenomenology of the Z_1 boson. Observe that Z_1 equals W_3^* at zeroth order in the *vev* in Eq. 3.60. We therefore computed the required Z_1 couplings to the SM fermions by substituting the change of basis in the Lagrangian and extracting the couplings at second order in v. Couplings of the Z_1 to SM particles can be found in Appendix D.

The model started with many parameters, $g_{el}, g_*, Y_*, m, \tilde{m}, \Delta, \tilde{\Delta}, M_*, \lambda_H$ and μ_H, but after the diagonalizations performed we have a lagrangian written in terms of the parameters of the SM g, Y, λ_H, μ_H, the warped composite model parameters $m_*, \tilde{m}_*, M_*$ and the mixing angles $\theta, \phi, \tilde{\phi}$. The parameter space can be explored by varying these parameters, giving that

$$g = g_* \sin\theta, \tag{6.3}$$

$$Y_{SM} = \sin\phi_{\psi_L} Y_* \sin_{\psi_R}, \tag{6.4}$$

are fairly well reproduced. We suppose for this work that the Yukawa matrix is diagonal, and that

$$g_*, Y_* \sim 1-4, \tag{6.5}$$

considering that the composite sector is more strongly coupled than the elementary one.

For the given setup, we compute mixing angles to fit first and third generation. A further tuning should be performed if one would like the model to also reproduce second generation and flavor physics constraints[1]. However, for the purposes of this work, where we aim to show

[1]For NP masses in the order of a few TeV, this could be achieved for instance in the lines of Ref. [103].

the utility of Z'-explorer and not to explore the full details of the model, the outcome of this diagonalization and mixing angles is enough to capture the essence of a Z' with varying couplings to the different generations due to mass mixing terms.

The masses of the SM quarks should also be preserved. Fermion masses are functions of the mixing angles, Y_*, m_* and $\tilde{m}_*$, these two masses being fixed. We scan on possible values of these parameters while requiring to accomplish the quarks masses and obtained the allowed region in parameter space.

In order to accomplish this goal, we took the matrix in Eq. 3.46 and we replaced Y by Y_* following Eq. 6.4. Then we multiplied it by its transposed as explained in Sec. 3.3.1 and then computed the eigenvalues numerically using Mathematica. We set the masses in fixed values $m_* = \tilde{m}_* = 2TeV$ since we have no interest in the new fermions and we suppose they must be quite heavy in order to be undetected until the day. So the remaining free variables are the ϕ angles and the Yukawas Y_*. Remember that these angles are function of the Δ parameters, so giving a limit for them is equal to give a limit for Δ. Since t_L, b_L is a doublet, both quarks share a unique parameter Δ, while in the case of the right quarks, t_R and b_R are singlets are therefore each one has its own parameter, $\tilde{\Delta}_t$ and $\tilde{\Delta}_b$, respectively. The same goes for the light generations and for leptons.

Results are shown in Fig. 6.1. We made a scatter plot of $\sin\phi_R$ vs $\sin\phi_L$ for $Y_* = 1,2,3,4$ showing the areas where 1GeV$< m_b <$ 10 GeV, 164GeV$< m_t <$ 184GeV and $0 < m_q <$ 0.005GeV for light quarks. It is important to recall that, while the y-axis represents $\sin\phi_L$ which is the same for both up and down type quarks, the x-axis represents $\sin\psi_R$, which is different for each type. In this plot both appear together for simplicity but it must be understood as a different axis for each quark type.

Coloured areas in plots of Fig. 6.1 represents the allowed angles for the values of the masses to hold giving certain range. We see that, as Y_* increases, the sine of the angles decreases, getting closer to zero. For light quarks, it is almost the same for up and down quarks, both allowing the same areas with really small angles. This is no surprising since the Yukawas and composite couplings were chosen to give strong coupling for the composite sector to the top and and to give weak couplings to the light fermions. For simplicity, we took $\phi_L = \phi_R = 0$ for all light fermions, including also the electron, since they are so close to zero. For bottom and top the thing is quite different. We see in the plots that the area allowed for the botton is similar to that of the light fermions, for ϕ_R, but it is another story for the left component ϕ_L. This angle should be very large since it also has to allow the top mass to be reached. The top quark needs both ϕ to be large. So finally we have that $\sin\phi_{b_R} \sim 0$, $\sin\phi_{t_R} \sim 1$ and $\sin\phi_L \sim 1$, which can be translated to $\tilde{\Delta}_b \sim 0$, $\tilde{\Delta}_t \gg 1$ and $\Delta \gg 1$.

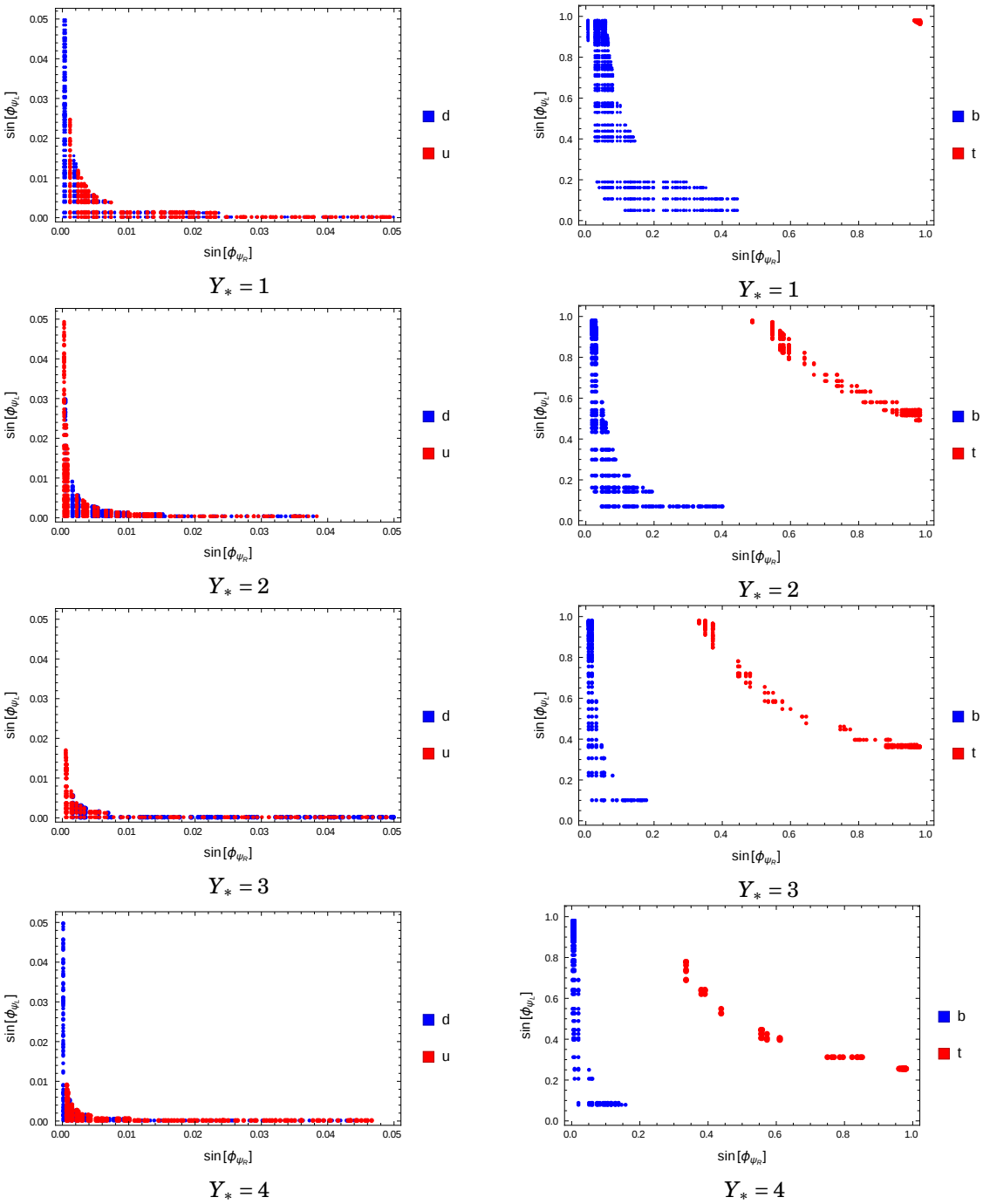

Figure 6.1: Scatter plot $\sin\phi_R$ vs $\sin\phi_L$ for $Y_* = 1,2,3,4$. On the left we have the light quarks while on the right we have the top and bottom. Coloured areas indicates the space allowed by masses using limits of 1GeV$< m_b <$ 10 GeV, 164GeV$< m_t <$ 184GeV and $0 < m_q <$ 0.005GeV for light quarks.

As mentioned before, since $\sin\phi = \frac{\Delta}{\sqrt{\Delta^2+m^2}}$, large Δ means $\sin\phi \sim 1$ (large mixing between fermions) and small Δ means $\sin\phi \sim 0$ (small mixing). So we have that b_L, t_L and t_R are much

coupled to the composite fermions while the light SM fermions and b_R are almost decoupled from them.

In the light of this approximations, we use in the following $0.4 < \phi_{t_L} < 0.9$. Whereas ϕ_{t_R} is determined once ϕ_{t_L} is chosen to reproduce the top mass within its limits. Observe that within our approximation couplings do not depend on ϕ_{t_R}.

Finally, we can set limits to the θ angles. We have already chosen $2 < g_* < 4$ and from the SM we know that $g_{weak} = g_2 \sim 0.64$ and $g_Y \sim 0.34$. Given the relation $\tan\theta = \frac{g_{el}}{g_*}$, which is valid for both composite couplings, we arrive to

$$0.15 < \theta_2 < 0.3, \tag{6.6}$$

$$0.065 < \theta_1 < 0.13, \tag{6.7}$$

where we used that $g_Y = \sqrt{\frac{3}{5}} g_1$.

6.6.1 Signals and Strength

The main goal of this work is to be able to estimate the strength of the signals of the cross sections of this Z_1 particle decaying to SM particles compared to the limits measured at the LHC. This procedure has already been presented and explained in Chap. 4. In this section, we will work with the strength calculated using the software Z'-explorer and we will show the results.

We take the couplings of the Z_1 to the fermions and the decay width to W^+W^- and to hZ to obtain the strengths to jj, bb, tt, ee, $\mu\mu$, $\tau\tau$, $\nu\nu$, W^+W^- and hZ. We fix the parameters $v = 0.246\text{TeV}$, $m_t = 0.174\text{TeV}$, $m = \tilde{m} = 2\text{TeV}$, $Y_t = 1$, and run M_* from $1-5\text{TeV}$, ϕ_L from $0.4-0.8$ and θ_1 and θ_2 from $0-1$, only to have a bigger look into the scene, knowing the real ranges are giving in Eq. 6.7.

Ref. [53] uses the couplings of fermions and bosons before the last diagonalization, as a simplified approximation. We compared the branching ratios giving in the paper with the ones obtained above using the diagonalization. For completeness, we give here the simplify widths from the paper,

$$\begin{aligned}
\Gamma(W^{*3} \to q\bar{q}) = 3\Gamma(W^{*3} \to \ell\bar{\ell}) &= \frac{g_2^2 M_*}{32\pi}\tan^2(\theta_2), \\
\Gamma(W^{*3} \to t\bar{t}) = \Gamma(W^{*3} \to b\bar{b}) &= \frac{g_2^2 M_*}{32\pi}\left(\sin^2(\phi_L)\cot(\theta_2) - \cos^2(\phi_L)\tan(\theta_2)\right)^2, \\
\Gamma(W^{*3} \to Zh) = \Gamma(W^{*3} \to W^+W^-) &= \frac{g_2^2 M_*}{192\pi}\cot^2(\theta_2).
\end{aligned} \tag{6.8}$$

At first look, we can see that the widths depends on the same variables that the ones calculated in this thesis using the diagonalization. Being the b quark massless, we need go to the next order in v to make ϕ_R and θ_1 appear. It is easy to see here that decays to light fermions and decays to

bosons are opposite in behaviour. For small θ_2, the decay to light fermions is small and it gets larger as θ_2 goes to 1, while decay to bosons goes exactly the other way. For heavy quarks, the widths behave in the same way as with the light quarks when ϕ_L is small, and they behave as the boson decay when ϕ_L is larger. This is because if ϕ_L is small the mixing between heavy quarks and composite heavy quarks does not practically exist and so they behave as light quarks. Having a larger coupling makes them mimic the behaviour of the bosons, which are strongly coupled to W^{*3}.

In Fig. 6.2 we can see that the branching fractions are much alike and the only appreciable difference appears for small ϕ_L. As a validity check, we verify that we recover the branching fractions in Ref. [53] in the corresponding limit.

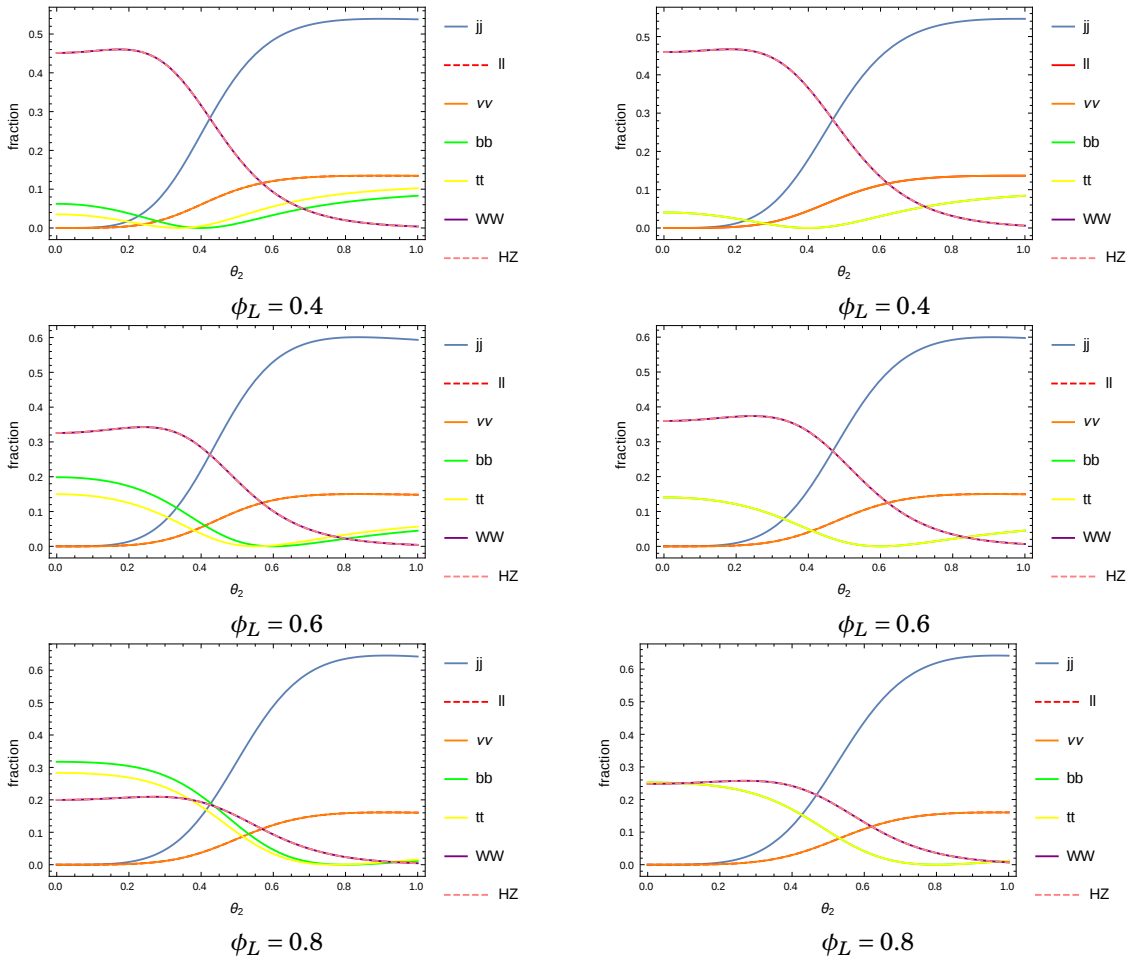

Figure 6.2: Branching ratios as function of θ_2 for $\phi_L = 0.4, 0.6, 0.8$. In the left we used the widths calculated in this thesis while in the right we used the widths given in [53].

Once the above calculations, details and validity checks for the Warped/Composite model have been performed, we can easily process the model through Z'-explorer and analyze the strength in each channel. We show the results for Z'-explorer output in Fig. 6.3. As it can be seen, three of

the channels are the most sensitive depending on the parameter region. For $0 < \theta_2 < 0.3$, it is the W^+W^- channel, which agrees with the plot of the branching ratios in Fig. 6.2, since this final state has a considerable larger fraction than other channels for small θ_2. This is the θ_2 range in which the theory considered to set the limits on this angle is preserved, but since there could be exceptions on the considerations, we also analyze the whole plot for $\theta_2 > 0.3$.

As θ_2 increases above 0.3 there is an interplay between the $\mu\mu$ branching ratio increase in Fig. 6.2 and its sensitivity, becoming this final state the most sensitive channel (largest strength). In some part of the parameter space –smaller masses, black color in Fig. 6.3– the model is discarded by $\mu\mu$, whereas in the other part is still allowed and also $\mu\mu$ is the most sensitive channel. As M_{Z_1} goes above 5.5 TeV, there are no $\mu\mu$ results and channel jj becomes the most sensitive one for large θ_2 and tt the most sensitive for small θ_2. The dijet final state also has a considerable increase in its branching ratio in this region. But in the case of tt, it may be surprising that it is not the channel with largest branching ratio, except for large ϕ_L. Nevertheless, for masses above 5.5 TeV there are only three channels with experimental limits, jj, tt and inv, being the last one discarded because of its small width. As a result, for large mass, tt is sensitive where it has the largest width and the same happens to jj. Results in Fig. 6.3 have almost negligible dependence on ϕ. Below in Fig. 6.4 we show some scatterplots of θ_2 vs $\sin\phi_L$ for M_* =2, as an example of the strength for each channel, showing allowed and excluded areas for each one.

In this chapter we have developed a software that computes the strength of the decay channels for a generic neutral boson coupled to the SM particles, using only the couplings or the width of the interaction. As it can be seen in Fig. 6.3, the software Z'-explorer condenses a large amount of information regarding the model itself and the experimental techniques for each specific channel, into one number –the strength– which yields a plot with the relevant information for the phenomenological analysis of the model. We have also performed a phenomenological study of the warped simplified theory by Contino and, using Z'-explorer , found the areas allowed by all the channels. This may be an interesting beginning in the search for new neutral bosons at the LHC.

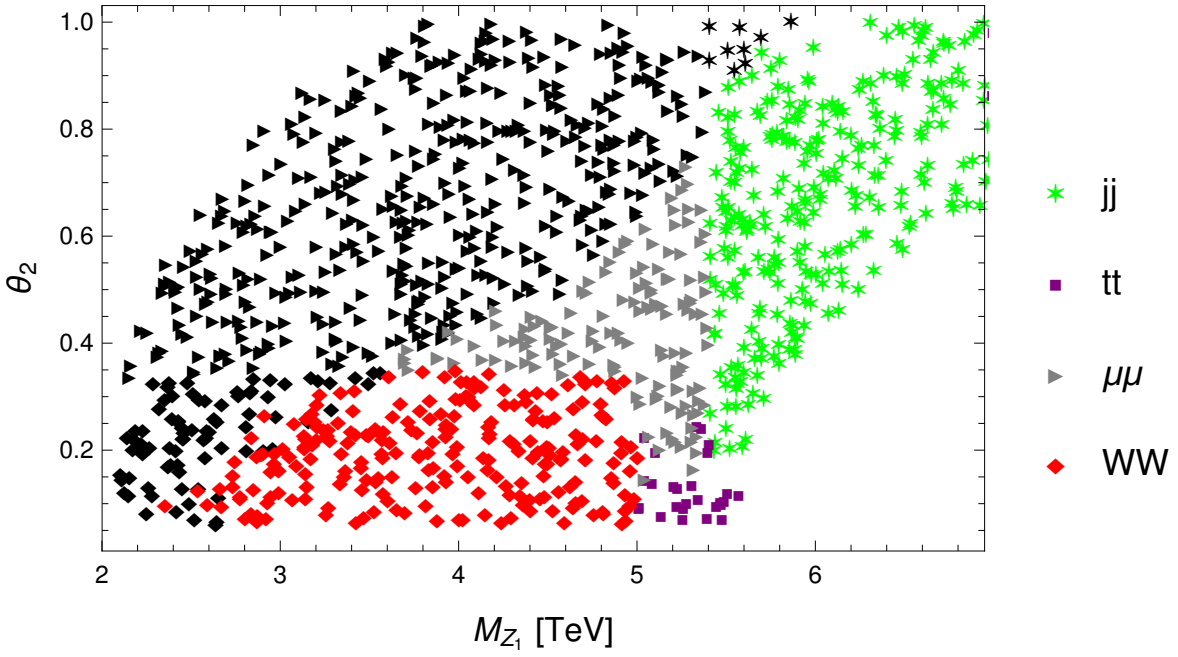

Figure 6.3: Exclusion plots for the different channels as function of θ_2 and M_{Z_1}. Color and shapes show the most sensitive channel; black meaning that the point in parameter space is excluded by the channel corresponding to its shape.

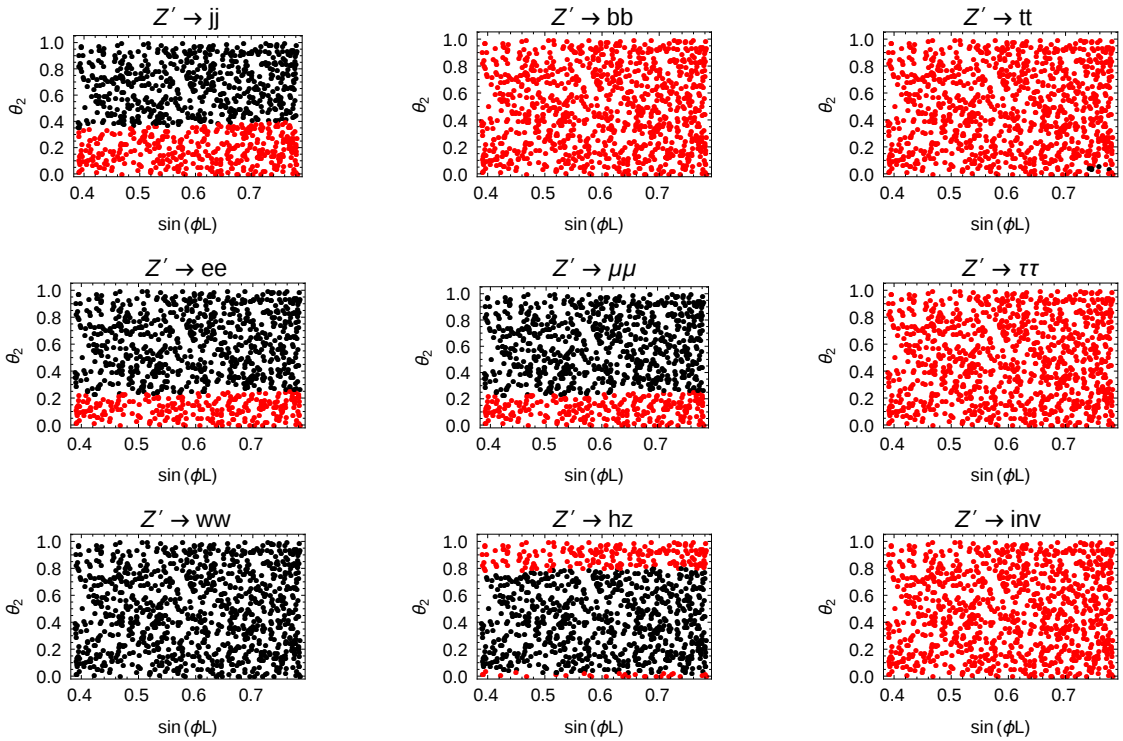

Figure 6.4: Exclusion plots for the different channels as function of θ_2 and ϕ_L, for $M_* = 2$TeV. Red indicates allowed points, black the excluded ones.

CHAPTER 7

CONCLUSIONES

Los resultados experimentales presentados en el Capítulo 2 y también la teoría discutida en el Capítulo 3 explican por qué la tercera generación de quarks representa una pista importante cuando se busca nueva física más allá del ME. En esta tesis estudiamos en profundidad diferentes características de la fenomenología a la hora de buscar nueva física en la tercera generación de quarks, prestando especial atención a los resultados experimentales y observables del LHC. Es la recopilación de muchos trabajos que persiguen el hallazgo de alguna pista que nos pueda ayudar a encontrar nuevas partículas. En la tesis proponemos una magnitud que nos permite buscar más fácilmente nuevas partículas, estudiamos teorías más allá del ME y también partículas con acoplamientos genéricos para conseguir una búsqueda más sencilla. También proponemos mediciones directas para algunos parámetros del ME que hasta el día de hoy no se han medido con precisión, y finalmente presentamos un programa que condensa una gran cantidad de información en un unicó párametro, arrojando una gráfica con la información relevante para el análisis fenomenológico del modelo. Esta tesis es el resultado de cuatro publicaciones [104–107], que se describen en los Capítulos 4, 5 y 6. A continuación resumimos las conclusiones de cada trabajo presentado en esta tesis.

A lo largo del Capítulo 4, hemos probado modelos de NF simplificados que se acoplan exclusivamente a quarks top y bottom en el marco del proceso $pp \to t\bar{t}b\bar{b}$. Hemos explorado modelos de NF con spín 0, 1 y 2 y encontramos la región en el espacio de parámetros en la que se espera que las búsquedas en $t\bar{t}bX$ sean más sensible que las búsquedas de $t\bar{t}t\bar{t}$, $b\bar{b}bX$ y $t\bar{t}$, así como el espacio de parámetros ya descartado. Hemos realizado un análisis cualitativo de los diagramas de Feynman más relevantes en los modelos de NF en función de las diferentes características de los modelos y realizamos una comparación cuantitativa calculando las secciones eficaces correspondientes y contrastándolas con la sensibilidad experimental en las búsquedas disponibles.

Encontramos que muchos de los resultados podrían ser entendidos a partir del análisis cualitativo. Hemos discutido posibles problemas en la detección de NF en el estado final $t\bar{t}bX$ a través de secciones eficaces totales debidos a que los generadores Montecarlo pueden fallar reproduciendo las distribuciones del quark bottom en el estado final. Propusimos un nuevo observable llamado M_{boosted} que se basa en la separación angular de los productos de decaimiento de una resonancia en función de su momento. M_{boosted} podría entenderse como una extensión de $\Delta R_{b\bar{b}}$ para el caso de producción asociada. Hemos demostrado que una resonancia tendrá una acumulación especial de eventos en el plano $\Delta R - p_T$, y hemos mostrado cómo se puede agrupar y medir este exceso. Además M_{boosted} es un observable con impacto reducido de Montecarlo, ya que permite entender un exceso a partir de la cinemática; al igual que ocurre con observables como la masa invariante o el ángulo de separación de los productos de decaimiento. Este observable puede ser útil en búsquedas de resonancia a través de este estado final, así como en otros contextos. Sin embargo, se requieren más análisis experimentales para estudiar la utilidad de este observable. Utilizando resultados experimentales preliminares, hemos realizado una primer estimación del alcance de descubrimiento del LHC durante los próximos años. Hemos propuesto mejoras simples al observable que mostramos a lo largo del trabajo que podrían extender este alcance. Este trabajo muestra que el estudio del estado final $t\bar{t}bX$ es importante para restringir NF que se acople a la tercera generación de quarks. El resultado más importante es que hemos identificado una fracción importante del espacio de parámetros en estos modelos de NF que aún no se ha puesto a prueba y en la que se espera que $t\bar{t}bX$ sea el canal más sensible. El interés en esta región del espacio de parámetros está motivado además por un ligero exceso encontrado en muchos observables relacionados.

Los elementos CKM V_{td} y V_{ts} son parámetros fundamentales del ME que gobiernan el cambio de sabor en el sector del top. Su determinación a través de mediciones directas es una tarea difícil que requiere procesos con quarks top on-shell. En el Capítulo 5 hemos propuesto un observable que puede testear $|V_{td}|$ a $O(10^{-1})$ en la creación de tW en el LHC. Seleccionando un estado final con $\ell^+\ell^- b\, p_T^{miss}$, hemos definido una asimetría de carga usando las variables η y p_T de los leptones, que es sensible a $|V_{td}|$. Hemos estudiado y caracterizado la señal y los backgrounds principales a nivel partónico, así como mediante el uso de simulaciones hasta el nivel de detector (paramétrico). Demostramos que, aunque los backgrounds tienen secciones eficaces de producción grandes, son altamente simétricos y eventualmente puede surgir una señal asimétrica. Hemos calculado la asimetría en función de $|V_{td}|$ y hemos determinado el alcance de descubrimiento del LHC en función de la luminosidad. Demostramos que el límite actual en la determinación directa de $|V_{td}|$ puede superarse con el set de datos del LHC existente, y que con $3000 fb^{-1}$ podría ser posible excluir $|V_{td}| \gtrsim 0.1$ a 2σ.

El background dominante $t\bar{t}$, aunque es de carga simétrica a primer orden, suprime fuertemente la asimetría al dar una gran contribución al denominador. Por lo tanto, una mejora crucial de nuestro enfoque basado en cortes sería reducir aún más este background mientras se conserva

la señal (utilizando, por ejemplo, técnicas de aprendizaje automático o multivariante). Como ejemplo, hemos mostrado en la Fig. 5.12 que, al reducir $t\bar{t}$ en un factor 2, sería posible excluir $|V_{td}| \gtrsim 0.1$ con $600 fb^{-1}$ de luminosidad. Finalmente, una reducción adicional significativa en las incertidumbres sistemáticas por debajo de nuestra estimación actual de 0.2% podría permitir que el (HL)LHC eventualmente testee valores más bajos de $|V_{td}|$. De hecho, tomando como referencia los sistemáticos actuales de asimetría de carga de $t\bar{t}$ en el estado final dileptónico [87], vemos que las principales fuentes de errores sistemáticos provienen de la incertidumbre debida a las variaciones de escala en la factorización y en la renormalización en la predicción teórica de $t\bar{t}$, y debido al número limitado de eventos en la muestra `MC@NLO` de Monte Carlo, ambos aportan 0.2%. Esto último no debería ser un problema en el futuro, mientras que lo primero requeriría el uso de predicciones teóricas mejoradas.

Encontramos que a 27 TeV con $3000 fb^{-1}$ podría ser posible probar $V_{td} \sim V_{ts}^{SM} \simeq 0.04$. Por otro lado, a 7 TeV la significancia también aumenta y con $3000 fb^{-1}$, los valores de $r < 10$ podrían ser accesibles con 3σ y los valores de $r \sim 10$ con 5σ. Esto es posible debido al hecho de que a energías más bajas el desbalance entre los quarks de valencia y los del mar del protón es mayor.

También hemos estudiado varias definiciones alternativas de la asimetría de carga, incluidas las asimetrías solo en $\eta(\ell)$, así como la implementación de cortes adicionales que podrían aumentar su tamaño. Descubrimos que en todos los casos la incertidumbre total aumenta y la significancia es, en el mejor de los casos, comparable con la original.

Finalmente, comentamos sobre otros procesos que también podrían brindar información valiosa para la determinación directa de V_{tq} en el LHC. Por ejemplo, las distribuciones cinemáticas en la producción de un solo top de canal t también podrían usarse para probar las contribuciones suprimidas de V_{ts} (y V_{td}) [50]. Sin embargo, un ejemplo mucho menos explorado como $pp \to W^+W^-$ que es sensible a V_{td} y V_{ts} y puede estudiarse en el LHC, podría ser complementario a los observables propuestos en este capítulo y en la literatura existente y ciertamente merece un estudio más detallado.

También propusimos otra estrategia para medir V_{td}, utilizando los backgrounds $gd \to tj$, $ud \to tj$ como señal y realizando otro análisis para mejorarlo. Estos procesos, junto con sus conjugados, tienen características cinemáticas que les otorgan una sección eficaz diferente. La estrategia implica el uso de un ajuste de plantilla e intenta deshacerse del background simétrico que no depende de la asimetría de carga y que podría permitirnos disminuir las incertidumbres sistemáticas. Encontramos que para $r = 20$ y una luminosidad de $300 fb^{-1}$, obtenemos un $\sigma = 1.2$, que no está mal pero tampoco es mejor que el método propuesto al principio del capítulo. A $3000 fb^{-1}$, obtenemos un $\sigma = 3.8$ que es mucho más interesante y podría ponerse a prueba en el (HL)LHC.

En el Capítulo 6 hemos diseñado un nuevo programa *Z'-explorer* para testear fácilmente modelos de NF con un bosón Z' en comparación con las restricciones experimentales en todos los canales de decaimiento de Z' que se pueden medir en el LHC. La idea principal de esta

herramienta es extraer los límites de producción por relación de ramificación por aceptancia de los resultados de ATLAS y CMS y aplicarlos sistemáticamente al modelo de NF de Z'. La entrada básica para Z'-explorer es un punto en el espacio de parámetros con la información fenomenológica relevante, y el programa devuelve como salida un número positivo para cada canal, que es la *fuerza* correspondiente. Si este número es mayor que 1, significa que el canal correspondiente rechaza el punto en el espacio de parámetros. Además, la sensibilidad al punto dado en el espacio de parámetros en cada canal se puede comparar estudiando la fuerza en cada canal: cuanto mayor es la fuerza, más sensible es el canal para rechazar (u observar) el modelo de NF.

El programa no necesita que el usuario ingrese el modelo ni ejecute ninguna simulación de Monte Carlo. En cambio, solo necesita la masa del Z', los acoplamientos a fermiones cargados y anchos parciales a decaimientos de tipo invisible, WW y Zh, en un archivo de texto simple, donde cada fila es un punto diferente en el espacio de parámetros para ser probado. Z'-explorer pretende ser lo más simple posible y, por lo tanto, muy rápido: en una computadora normal puede procesar 1000 puntos en unos pocos segundos. Todo el programa es de código abierto escrito en `C ++` y puede ser utilizado, modificado y mejorado por otros usuarios a través de su interfaz de `Github` [88].

Hemos validado Z'-explorer aplicándolo al modelo Warped/Composite. Hemos bosquejado el trabajo requerido antes de ejecutar el programa, que consiste en identificar el autoestado de masa Z', sus acoplamientos a los fermiones del ME y su ancho de decaimiento a los bosones del ME. La ejecución de Z'-explorer usando estos modelos de NF y el análisis correspondiente de su salida, ha demostrado cómo Z'-explorer condensa el lado teórico del modelo y las técnicas experimentales para cada canal incluyendo sus antecedentes relevantes, exhibiendo el poder de la herramienta presentada. En consecuencia, muchas de estas características se analizan a lo largo del texto.

Hemos analizado los beneficios y problemas de un programa tan sencillo y cómo, en algunos casos, los problemas pueden tener una solución. También discutimos diferentes posibles mejoras a Z'-explorer. Consideramos que incluir la correlación entre los canales, los resultados de la física de baja energía y los límites de la materia oscura sería muy conveniente. El objetivo principal del programa presentado Z'-explorer es proporcionar una herramienta útil para que el teórico y el experimental pongan a prueba los modelos de NF con Z' con los datos del LHC.

En el capítulo 3 repasamos el modelo Warped/Composite simplificado. Reproducimos los resultados teóricos y mostramos explícitamente todos los cálculos. Elegimos realizar una aproximación para resolver el problema de diagonalización, escribiendo los nuevos estados como una serie de potencias de v^2. De esta forma, obtuvimos los acoplamientos de un nuevo bosón neutro Z_1 a las partículas del ME. Recuperamos los resultados previos. El uso de Z'-explorer nos permitió calcular las fuerzas de los muchos canales de decaimiento y analizar su comportamiento. Descubrimos que tres de los canales son los más sensibles según el espacio de parámetros. El canal W^+W^- es

el más sensible en el rango del ángulo en el que se conserva la teoría considerada para establecer los límites, ya que este estado final tiene una fracción considerablemente mayor que otros canales para θ_2 pequeño. De esta manera, si se buscan bosones neutros con las características de una partícula compuesta del modelo de Contino en el LHC, entonces debería ser factible encontrar pistas mirando el canal de decaimiento W^+W^-.

Estamos en una era de precisión, donde los experimentos se refinan cada día y donde la medición de excesos relacionada con la presencia de nuevas partículas cada vez parece estar más lejos. Esta tesis intenta aportar métodos directos e indirectos para realizar mediciones en el LHC que podrían servir para encontrar pistas de una Nueva Física aún desconocida, así como estudiar modelos teóricos con el fin de tener un mejor entendimiento de la fenomenología que esto conlleva. Podría ser que los excesos de hoy impliquen una Nueva Física oculta, y que estemos a las puertas de un descubrimiento.

CHAPTER 8

CONCLUSIONS

The experimental results presented on Chapter 2 and also the theory discussed in Chapter 3 explain why the third generations of quarks represents a smoking gun when looking for new physics beyond the SM. In this thesis we deeply studied different characteristics of the phenomenology when searching for new physics in the third generation of quarks, taking special care of the experimental results and observables of the LHC. It is the compilation of many works that pursue the find of any clue that could help us find new particles. We propose a magnitude that allows us to seek more easily for new particles, studied theories beyond the SM and also particles with generic couplings to get an easier search. We also propose direct measurements for some SM parameters which until the day have not been measured with precision, and finally we present a software that condenses a large amount of information into one number, yielding a plot with the relevant information for the phenomenological analysis of the model. This thesis is the result of four publications [104–107], which are described in Chapters 4, 5 and 6. In the following we summarize the conclusions of each work presented in this thesis.

Along Chapter 4 we have tested simplified NP models that couple exclusively to top and bottom quarks in the context of the $pp \to t\bar{t}b\bar{b}$ process. We have explored spin 0, 1 and 2 NP models and find the region in parameter space in which searches in $t\bar{t}bX$ are expected to be more sensitive that searches in $t\bar{t}t\bar{t}$, $b\bar{b}bX$ and $t\bar{t}$, as well as the already discarded parameter space. We have made a qualitative analysis of the most relevant Feynman diagrams in the NP models as a function of the different features of the models. We have made the quantitative comparison by computing the corresponding cross-sections and comparing them to the experimental sensitivity in available searches. We found that many of the results could be understood from the qualitative analysis. We have discussed potential issues in detecting NP in the $t\bar{t}bX$ final state through

total cross-sections, since Montecarlo generators may fail in reproducing the bottom quark distributions in the final state. We have proposed a new observable called M_{boosted} which is based in the angular separation of the decay products of a resonance as a function of its momentum. M_{boosted} could be understood as an extension of $\Delta R_{b\bar{b}}$ for the case of associated production. We have shown that a resonance will have a special accumulation of events in the $\Delta R - p_T$ plane, and we have shown how this excess can be binned and measured. We show that M_{boosted} is an observable with reduced impact of Montecarlo, since an excess can be understood from the kinematics; just as it happens with observables as the invariant mass or the angle of separation of decay products. This observable may be useful in a resonance search through this final state, as well as in other contexts. Further experimental analysis is required to study the usefulness of this observable. Using preliminary experimental results we have done a raw estimation of the discovery reach for LHC during the next years. We have proposed simple improvements to the observable which we show along the work that could extend the reach. This work shows that the study of the $t\bar{t}bX$ final state is important in constraining NP that couples to third generation of quarks. The most important result is that we have identified an important fraction of parameter space in these NP models that has not been probed yet and in which $t\bar{t}bX$ is expected to be the most sensitive channel. The interest in this region of parameter space is further motivated by slight excess found in many related observables.

The CKM elements V_{td} and V_{ts} are fundamental parameters of the SM governing flavor conversion in the top sector. Their determination through direct measurements is a difficult task that requires processes with on-shell top quarks. Along Chapter 5 we have proposed an observable that can test $|V_{td}|$ to $O(10^{-1})$ in the creation of tW at the LHC. Selecting a final state with $\ell^+\ell^- b\, p_T^{miss}$, we have defined a charge asymmetry using the variables η and p_T of the leptons, that is sensitive to $|V_{td}|$. We have studied and characterized the signal and main backgrounds at parton level, as well as by using simulations up to (parametric) detector level. We have shown that, although the backgrounds have overwhelming production cross sections, they are highly symmetric and an asymmetric signal can eventually emerge. We have computed the asymmetry as a function of $|V_{td}|$, and determined the prospective reach of the LHC as a function of the luminosity. We have shown that the current bound on direct determination of $|V_{td}|$ can be surpassed with the existing LHC dataset, and that with $3000 fb^{-1}$ it could be possible to exclude $|V_{td}| \gtrsim 0.1$ at the 2σ level.

The dominant $t\bar{t}$ background, although being charge-symmetric at leading order, strongly suppresses the asymmetry by giving a large contribution to its denominator. A crucial improvement upon our cut-based approach would therefore be to further reduce this background while preserving the signal (using e.g. multivariate or machine-learning techniques). As an example, we have shown in Fig. 5.12 that, by lowering $t\bar{t}$ by a factor 2, it would be possible to exclude $|V_{td}| \gtrsim 0.1$ already with $600 fb^{-1}$ of luminosity. Finally, a further significant reduction in systematic uncertainties below our current estimate of 0.2% could allow the (HL)LHC eventually to probe lower

values of $|V_{td}|$. In fact, taking as reference the current $t\bar{t}$ charge asymmetry systematics in the dileptonic final state [87], we see that the main sources of systematics come from the uncertainty due to the factorization and renormalization scale variations in the theoretical $t\bar{t}$ prediction, and due to the limited number of events in the MC@NLO Monte Carlo sample, both contributing 0.2%. The latter would not be a problem in the future, whereas the former would require the use of improved theoretical predictions.

We found that at 27 TeV with $3000fb^{-1}$ it could be possible to probe $V_{td} \sim V_{ts}^{SM} \simeq 0.04$. On the other hand, at 7 TeV the significance also increase and with $3000fb^{-1}$, values of $r < 10$ could be accesible with 3σ and values of $r \sim 10$ with 5σ. This is posible due to the fact that at lower energies the imbalance between quarks of valence and those in the sea of the proton is higher.

We have also studied a number of alternative definitions of the charge asymmetry, including asymmetries only in $\eta(\ell)$, as well as the implementation of additional cuts that could increase their size. We found that in all the cases the total uncertainty increases, and the significance is at best comparable with the original one.

Finally, we comment on other processes that could also give valuable information for the direct determination of V_{tq} at the LHC. For example, kinematical distributions in t-channel single top production could also be used to probe V_{ts} (and V_{td}) suppressed contributions [50]. A much less explored example is however $pp \to W^+W^-$ that is sensitive to V_{td} and V_{ts} and can be studied at the LHC. It can be complementary to the observables proposed in this chapter and in the existing literature and certainly deserves a detailed study.

We also proposed another strategy to measure V_{td}, using one of $gd \to tj$ backgrounds, $ud \to tj$, as a signal and perform another analysis to enhance it. This process, together with its conjugate, have kinematical features that give them different cross section. The strategy involves the use of a template fit and tries to get rid of the symmetric background which does not rely on charge asymmetry and that could allow us to diminish systematic uncertainties. We found that for $r = 20$ and a luminosity of $300fb^{-1}$, we get a $\sigma = 1.2$, which is not bad but is not better than the method proposed at the beginning of the chapter. At $3000fb^{-1}$, we get a $\sigma = 3.8$ which is much more interesting and could be tested at the (HL)LHC.

On Chapter 6 we have designed a new software Z'-*explorer* to easily test NP models with a Z' boson against experimental constraints in all Z' decay channels that can be measured at LHC. The main idea of this tool is to extract the bounds in production times branching ratio times acceptance from the ATLAS and CMS results and apply them systematically to the NP Z' model. The basic input for Z'-explorer is a point in parameter space with the relevant phenomenological information, and the program returns as output a positive number for each channel, which is its corresponding strength. If this number is larger than 1, means that the point in parameter space is rejected by the corresponding channel. Moreover, the sensitivity to the given point in parameter space in each channel may be compared by studying the strength in each channel: the larger the strength, the more sensitive is the channel to reject (or observe) the NP model.

The program does not need the user to input the model, nor run any Monte Carlo simulation. Instead, just needs the Z' mass, couplings to charged fermions and partial widths to invisible, WW and Zh, in a simple text file, where each row is a different point in parameter space to be tested. Z'-explorer is intended to be as simple as possible, and therefore very fast: in a normal computer it can process 1000 points in a few seconds. The whole program is open source written in `C++` and can be used, modified and improved by other users through its `Github` interface [88].

We have validated Z'-explorer by applying it to the Warped/Composite model. We have sketched the required work before running the software, which consists in identifying the mass eigenstate Z', its couplings to SM fermions, and its width to SM bosons. The running of Z'-explorer on this NP models and the corresponding analysis of its output, has shown how Z'-explorer condenses the theoretical side of the model, and the experimental techniques for each channel including its relevant backgrounds, exhibiting the power of the presented tool. Many of these features are accordingly discussed along the text.

We have discussed benefits and issues of such a straightforward software and how in some cases the problems may have a workaround. We have also discussed different possible improvements to Z'-explorer. We consider that including correlation between channels, low-energy physics results and Dark Matter bounds, would be very compelling.

The main objective of the presented software Z'-explorer is to provide a useful tool for theorist and experimentalist to test Z' NP models against LHC data.

In Chapter 3 we revisited the simplified warped composite model. We reproduced the theoretical results and explicitly showed all the calculations. We choose to perform an approximation to solve the diagonalization problem, writing the new states as a power series of v^2. In this way, we obtained the couplings of a new neutral boson Z_1 to the SM particles. We recovered the results in the paper. Using Z'-explorer allowed us to calculate the strengths to the many decay channels and analyze their behavior. We found that three of the channels are the most sensitive depending on the parameter region. The W^+W^- channel is the most sensitive in the range of the angle in which the theory considered to set the limits is preserved, because this final state has a considerable larger fraction than other channels for small θ_2. In this way, if someone is looking for a neutral bosons with the characteristics of a composite particle from the Contino model at the LHC, then it should be feasible to find a hint looking at the W^+W^- decay channel.

We are in an era of precision, where experiments are refined every day and where the measurement of excesses related to the presence of new particles seems to be further and further away. This thesis attempts to provide direct and indirect methods to carry out measurements at the LHC that could be used to find clues of a unknown New Physics, as well as to study theoretical models in order to have a better understanding of the phenomenology that this entails. It could be that today's excesses imply a hidden New Physics, and that we are at the doors of a discovery.

Lista de Publicaciones

La siguiente es la lista de publicaciones realizadas durante mi doctorado:

- E. Alvarez and M. Estevez. "$ttbb$ as a probe of new physics at the LHC". In: *Phys. Rev. D* 96, 035016 (2017). DOI: 10.1103/PhysRevD.96.035016. arXiv: 1701.04427
- E. Alvarez, L. Da Rold, M. Estevez, and J. F. Kamenik. "Measuring $|V_{td}|$ at the LHC". In: *Phys. Rev. D* 97, 033002 (2018). DOI: 10.1103/PhysRevD.97.033002. arXiv: 1709.07887
- M. Estevez, D. Faroughy, J. Kamenik. "Opportunities in flavour physics at the HL-LHC and HE-LHC". In: *CERN Yellow Reports* Vol.7 (2019). DOI: 10.1103/PhysRevD.96.035016. arXiv: 1812.07638
- E. Alvarez, M. Estevez, and R. M. S. Seoane. "Z'-explorer: a simple tool to probe Z' models against LHC data". *Awaiting publication*. arXiv: 2005.05194

List of Publications

The following is the list of the works published during my PhD:

- E. Alvarez and M. Estevez. "$ttbb$ as a probe of new physics at the LHC". In: *Phys. Rev. D* 96, 035016 (2017). DOI: 10.1103/PhysRevD.96.035016. arXiv: 1701.04427
- E. Alvarez, L. Da Rold, M. Estevez, and J. F. Kamenik. "Measuring $|V_{td}|$ at the LHC". In: *Phys. Rev. D* 97, 033002 (2018). DOI: 10.1103/PhysRevD.97.033002. arXiv: 1709.07887
- M. Estevez, D. Faroughy, J. Kamenik. "Opportunities in flavour physics at the HL-LHC and HE-LHC". In: *CERN Yellow Reports* Vol.7 (2019). DOI: 10.1103/PhysRevD.96.035016. arXiv: 1812.07638
- E. Alvarez, M. Estevez, and R. M. S. Seoane. "Z'-explorer: a simple tool to probe Z' models against LHC data". *Awaiting publication*. arXiv: 2005.05194

APPENDIX A

NP MODELS IN CHAPTER 4

We provide some more details on the NP models presented in Sect. 2.2

Scalar ϕ

$$F(z) = \begin{cases} \frac{3}{2}z\left(1+(1-z)\left(-\frac{1}{4}\left[\log\left(\frac{1+\sqrt{1-z}}{1-\sqrt{1-z}}\right)-i\pi\right]^2\right)\right) & z<1 \\ \\ \frac{3}{2}z(1+(1-z)\quad \arctan^2\left[\frac{1}{\sqrt{z-1}}\right]) & z>1 \end{cases} \tag{A.1}$$

$$\Gamma(\phi \to q\overline{q}) = c_{\phi q}^2 \frac{3M}{8\pi}\beta^3(m_q, M), \tag{A.2}$$

$$\Gamma(\phi \to gg) = \frac{\alpha_s^2 M^3}{144\pi^3}\left|\frac{c_{\phi t}}{m_t}F(z_t)+\frac{c_{\phi b}}{m_b}F(z_b)\right|^2. \tag{A.3}$$

$$\beta(m_q, M) = \sqrt{1-\frac{4m_q^2}{M^2}} \tag{A.4}$$

Pseudoscalar A

$$H(z) = z\begin{cases} -\frac{1}{4}\left[\log\left(\frac{1+\sqrt{1-z}}{1-\sqrt{1-z}}\right)-i\pi\right]^2 & z<1 \\ \\ \arcsin^2\left(\sqrt{\frac{1}{z}}\right) & z>1 \end{cases} \tag{A.5}$$

$$\Gamma(A \to q\overline{q}) = c_{Aq}^2 \frac{3M}{8\pi}\beta(m_q, M), \tag{A.6}$$

$$\Gamma(A \to gg) = \frac{\alpha_s^2 M^3}{64\pi^3}\left|\frac{c_{At}}{m_t}H(z_t)+\frac{c_{Ab}}{m_b}H(z_b)\right|^2. \tag{A.7}$$

CP-violating scalar φ

$$\Gamma(\varphi \to q\bar{q}) = c_{\varphi q}^2 \frac{3M}{8\pi}\beta(m_q, M)(1+\beta^2(m_q, M)), \tag{A.8}$$

$$\Gamma(\varphi \to gg) = \frac{\alpha_s^2 M^3}{144\pi^3}\left|\frac{c_{\varphi t}}{m_t}F(z_t)+\frac{c_{\varphi b}}{m_b}F(z_b)\right|^2 + \frac{\alpha_s^2 M^3}{64\pi^3}\left|\frac{c_{\varphi t}}{m_t}H(z_t)+\frac{c_{\varphi b}}{m_b}H(z_b)\right|^2. \tag{A.9}$$

Vector Z'

$$\Gamma(Z' \to q_R \bar{q}_R) = \frac{3c_{Z'q}^2}{24\pi M^2}(M^2 - m_q^2)\beta(m_q, M) \tag{A.10}$$

Axial Vector $\tilde{Z}'$

$$\Gamma(Z' \to q\bar{q}) = \frac{3c_{\tilde{Z}'q}^2}{12\pi M^2}\beta^3(m_q, M) \tag{A.11}$$

Graviton G

$$\begin{aligned} A_G(z,\mu_0) = &-112\Big[-94z(z+2)[2\tanh^{-1}(\sqrt{1-z})-i\pi]^2 \\ &+ 3(5z+4)\sqrt{1-z}[2\tanh^{-1}(\sqrt{1-z})-i\pi]-39z-35-12\ln\mu_0^2 m_q^2\Big] \quad (z<1) \end{aligned} \tag{A.12}$$

$$\begin{aligned} A_G(z,\mu_0) = &-112\Big[94z(z+2)[2\tan^{-1}(\sqrt{z-1})-\pi]^2 \\ &- 3(5z+4)\sqrt{z-1}[2\tan^{-1}(\sqrt{z-1})-\pi]-39z-35-12\ln\mu_0^2 m_q^2\Big] \quad (z>1) \end{aligned} \tag{A.13}$$

Where following Ref. [52] we take $\mu_0 = M$ which represents the energy scale of the process.

$$\Gamma(G \to q_R \bar{q}_R) = \frac{3M^3}{320\pi\Lambda^2}\beta(m_q, M)^{3/2}\left(c_{Gq}^2\left(1-\frac{2m_q}{3M}\right)\right), \tag{A.14}$$

$$\Gamma(G \to gg) = \frac{M^3}{10\pi\Lambda^2}\frac{\alpha_s^2}{144\pi^2}\left|c_{Gt}A_G(z_t,\mu_0)+c_{Gb}A_G(z_b,\mu_0)\right|^2. \tag{A.15}$$

APPENDIX B

TOP TRANSVERSE MASS RECONSTRUCTION

In this section we give a brief guide on how to calculate the invariant mass of a top that produces MET in its decay. In this case, the top decays into a b-jet and a W, which decays leptonically (see Fig. B.1). The neutrinos cannot be detected on the LHC, thus they are known as missing energy. The z component of the momentum, being z the axis where the beams come from, has an initial component unknown, since we do not know exactly the initial momentum. On the other side, we do know that there is no initial momentum in the other axis, so that we can calculate the transversal components of the neutrino momentum using momentum conservation. This is the MET. When the neutrino comes from a W decayed leptonically, we can calculate $p_z(\nu)$.

Since we only know the x and y components of the neutrino momentum, that is equivalent to know its p_T and ϕ, giving the relations

$$p_x = p_T \cos(\phi), \tag{B.1}$$

$$p_y = p_T \sin(\phi), \tag{B.2}$$

$$p_z = p_T \sinh(\eta), \tag{B.3}$$

$$E = \sqrt{p_x^2 + p_y^2 + p_z^2 + m_{inv}^2}. \tag{B.4}$$

Here we work with a mixture of names because in this case calculations are easier with Cartesian coordinates but the measurements are giving in the other frame.

From the conservation of momentum we have

$$P_W^2 = (P_\ell + P_\nu)^2, \tag{B.5}$$

where P is a four-moment vector. And it is also true that $P_W^2 = m_W^2$, which in this whole thesis it has been taken to $m_W = 80.4 GeV$, and we consider $m_\ell = m_\nu = 0$ since the 3-dimensional

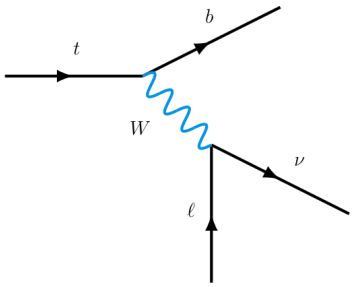

Figure B.1: Feynman diagram of the top quark decay $t \to bW \to b\ell\nu$.

momentum is much larger than the mass. This way we also have $P_i^2 = 0$ and $|\bar{P}_i| = E_i$, with $i = \ell, \nu$. We can use this in Eq. B.5 and thus

$$m_W^2 = 2(E_\ell E_\nu - \bar{P}_\ell \cdot \bar{P}_\nu), \tag{B.6}$$

which can be rewritten as

$$\left(\frac{m_W^2}{2} + p_\ell^x p_\nu^x + p_\ell^y p_\nu^y + p_\ell^z p_\nu^z\right)^2 = |\bar{P}_\ell|^2 (p_\nu^{x\,2} + p_\nu^{y\,2} + p_\nu^{z\,2}). \tag{B.7}$$

This equation is quadratic in p_ν^z and can be solved in `Mathematica`. There are two solutions, and following [108], we choose the one with smaller absolute value as the most probable solution to these physics. Now we are able to calculate the lepton-neutrino transverse mass $m_T^{\ell\nu}$,

$$m_T^{\ell\nu} = \sqrt{2 p_T^\ell p_T^\nu (1 - \cos(\phi^\ell - \phi^\nu))}. \tag{B.8}$$

Finally, using the conservation of momentum for the top, we have $P^t = P^\nu + P^\ell + P^b$ and we can calculate the invariant mass of the top m_t as

$$m_t = \sqrt{E_t^2 - |\bar{P}_t|^2}, \sqrt{2} \tag{B.9}$$

APPENDIX C

SIMULATION OF tW AT NLO IN MADGRAPH

There is a problem when trying to generate the processes $pp \to tW$ and $pp \to tWb$, with 4 and 5 flavors, respectively, both at NLO in `MadGraph5`. It starts calculating non converging loops and thus never finishes. In this appendix we try to explain a possible way to hand-solve this problem.

The problem with tW production is that, in the 5F scheme, the real emission can have contributions like $gg \to tWb$ with intermediate on-shell top, which need to be subtracted [109]. The automation of the subtraction used in the cited paper is not yet complete, so there is not an easy way out, unless you kill the diagrams with intermediate tops by hand.

So trying to generate `p p > t w [QCD]` with sm-ckm does not work. What we should do is run

```
> import model loop_sm-no_b_mass
> generate p p > t w- [QCD]
> add process p p > t~ w+ [QCD]
> output
> launch
```

This is NLO and the model is a 5F scheme with a massless b quark, see Sect. 3 in [109]. If we run launch at this stage, MG5 will stay indefinitely running, as mentioned before. But what we do is to run it anyway so it generates the running files and then kill it. We go to the new folder created and search for the `SubProcesses` file, and then look for folders like `P0_bg_wmt`, which contain certain process that compounds the main one, depending on the initial states. We need to enter in each one of those folders and remove the ones with a resonant top [double top, see [76], Fig. 2] . In the case of tW, the troublesome real emission will be one bb initiated and three gg initiated ones. We find the corresponding `matrix_*.f` file and if we look at the feynman diagrams

(e.g. the corresponding ps or jpeg files), we see which diagrams involving a resonant top they are. In order to set them to zero, edit the .f file, where you have the end of the helas calls

```
JAMP(1)=+1D0/2D0*(+1D0/3D0*AMP(1)+AMP(2)+AMP(3)+1D0/3D0*AMP(4))
JAMP(2)=+1D0/2D0*(-AMP(1)-1D0/3D0*AMP(2)-1D0/3D0*AMP(3)-AMP(4))
```

There is the list of processes. Next we need to do is set to zero the AMP() that we do not want right before the JAMP lines. For example, if they are the number 2, 4 and 7, we set

```
AMP(2) = dcmplx(0d0,0d0)
AMP(4) = dcmplx(0d0,0d0)
AMP(7) = dcmplx(0d0,0d0)
```

where dcmplx(0d0,0d0) is the complex zero of Fortran. The other partonic subprocesses follow in total analogy, note that the number of the matrix_x.f corresponding to the gg and bb initiated real emission may change, and also the number of the diagrams to be set to zero (there will always be 3 diagrams for gg and 1 for bb).

And that's it, we now can run the process going to MG5, set in the tW folder, and run ./bin/generate_events.

APPENDIX D

COUPLINGS OF THE $Z1$ TO SM FERMIONS

We can know the couplings of the Z_1 boson to the fermions by substituting the old bosons for the mass states after the diagonalization in Eq. 3.28. We extract the couplings at second order in v.

Since we take all the fermions with the exception from the top as massless, we considered $Y_f = 0$ except $Y_t = 1$. Also, given the results in Sect. 6.6, we take $\phi_{bR} = 0$. This simplifies the model and allows us to comprehend a little more the behaviour of the couplings. We can see that all light fermions have a similar coupling, with the left ones having an extra term coming from their $SU(2)$ interaction. The top quarks has extra terms, in particular the left top. The same goes for the bottom, except that since this is a massless quark, its Yukawa is zero so it kills some extra terms and also $\phi_{bR} = 0$.

Couplings to the first two generation of quarks, both considered light, are given by Eqs. D.2,

$$\begin{aligned}
g_{uL} &= -\frac{g_2 g_y (g_2^2+g_y^2)\cos(\theta_2)^2\cot(\theta_2)v^2}{24\sqrt{g_y^2+g_2^2}M_*^2} + \frac{1}{2}g_2\tan(\theta_2),\\
g_{uR} &= -\frac{g_2 g_y (g_2^2+g_y^2)\cos(\theta_2)^2\cot(\theta_2)v^2}{6\sqrt{g_y^2+g_2^2}M_*^2},\\
g_{dL} &= -\frac{g_2 g_y (g_2^2+g_y^2)\cos(\theta_2)^2\cot(\theta_2)v^2}{24\sqrt{g_y^2+g_2^2}M_*^2} - \frac{1}{2}g_2\tan(\theta_2),\\
g_{dR} &= \frac{g_2 g_y (g_2^2+g_y^2)\cos(\theta_2)^2\cot(\theta_2)v^2}{12\sqrt{g_y^2+g_2^2}M_*^2}.
\end{aligned} \tag{D.1}$$

The couplings to the third generation of quarks are given in Eq. D.3, where the top is considered heavy and the bottom is massless.

$$
\begin{aligned}
g_{tL} &= -\frac{g_2 g_y (g_2^2+g_y^2)\cos(\theta_2)^2\cot(\theta_2)v^2}{24\sqrt{g_y^2+g_2^2}M_*^2} + \frac{v g_2 Y_t \cot(\phi_L)}{2\sqrt{2}m_*}\cos(\phi_L)\csc(\theta_2)\sec(\theta_2)\sin(\phi_L) \\
&\quad - \frac{1}{2}g_2\left(\cot(\theta_2)\sin(\phi_L)^2 - \tan(\theta_2)\cos(\phi_L)^2\right) - \frac{v^2 g_2 Y_t^2 \cot(\phi_L)^2}{4m_*^2}\left(\cot(\theta_2)\cos(\phi_L)^2 - \tan(\theta_2)\sin(\phi_L)^2\right), \\
g_{tR} &= -\frac{g_2 g_y (g_2^2+g_y^2)\cos(\theta_2)^2\cot(\theta_2)v^2}{6\sqrt{g_y^2+g_2^2}M_*^2}, \\
g_{bL} &= -\frac{g_2 g_y (g_2^2+g_y^2)\cos(\theta_2)^2\cot(\theta_2)v^2}{24\sqrt{g_y^2+g_2^2}M_*^2} + \frac{1}{2}g_2\left(\cot(\theta_2)\sin(\phi_L)^2 - \tan(\theta_2)\cos(\phi_L)^2\right), \\
g_{bR} &= \frac{g_2 g_y (g_2^2+g_y^2)\cos(\theta_2)^2\cot(\theta_2)v^2}{12\sqrt{g_y^2+g_2^2}M_*^2},
\end{aligned}
\tag{D.2}
$$

where $m_* = \frac{m}{\cos(\phi_L)}$, see Eq. 3.21, and remember m_* is the diagonalized mass. Finally, couplings to all leptons are given in Eq. D.4, where the three generations are considered light.

$$
\begin{aligned}
g_{eL} &= \frac{g_2 g_y (g_2^2+g_y^2)\cos(\theta_2)^2\cot(\theta_2)v^2}{8\sqrt{g_y^2+g_2^2}M_*^2} - \frac{1}{2}g_2\tan(\theta_2), \\
g_{eR} &= \frac{g_2 g_y (g_2^2+g_y^2)\cos(\theta_2)^2\cot(\theta_2)v^2}{4\sqrt{g_y^2+g_2^2}M_*^2}, \\
g_{\nu L} &= \frac{g_2 g_y (g_2^2+g_y^2)\cos(\theta_2)^2\cot(\theta_2)v^2}{8\sqrt{g_y^2+g_2^2}M_*^2} - \frac{1}{2}g_2\tan(\theta_2), \\
g_{\nu R} &= 0.
\end{aligned}
\tag{D.3}
$$

BIBLIOGRAPHY

[1] J. Wess and B. Zumino, Nucl. Phys. **B70**, 39 (1974).

[2] P. Fayet and S. Ferrara, Phys. Rept. **32**, 249 (1977).

[3] L. Randall and R. Sundrum, Phys. Rev. Lett. **83**, 4690 (1999), hep-th/9906064.

[4] T. Carli (ATLAS, CMS), Nucl. Part. Phys. Proc. **273-275**, 29 (2016).

[5] M. Moreno Llacer (ATLAS), PoS **CORFU2014**, 082 (2015).

[6] F. Margaroli (ATLAS, CDF, CMS, D0), Nuovo Cim. **C38**, 10 (2015).

[7] T. A. collaboration (ATLAS) (2016).

[8] V. Khachatryan et al. (CMS), Phys. Rev. **D91**, 052009 (2015), 1501.04198.

[9] C. Patrignani et al. (Particle Data Group), Chin. Phys. **C40**, 100001 (pp. 624 (2016).

[10] R. Mankel (CMS), PoS **EPS-HEP2015**, 125 (2015).

[11] S. Chatrchyan et al. (CMS), Phys. Lett. **B722**, 207 (2013), 1302.2892.

[12] V. Khachatryan et al. (CMS), JHEP **11**, 071 (2015), 1506.08329.

[13] T. A. collaboration (2016).

[14] L. Beck (CMS), in *9th International Workshop on Top Quark Physics (TOP 2016) Olomouc, Czech Republic, September 19-23, 2016* (2016), 1611.09607, URL http://inspirehep.net/record/1500694/files/arXiv:1611.09607.pdf.

[15] C. Collaboration (CMS) (2016), CMS-PAS-TOP-16-016.

[16] E. Alvarez, D. A. Faroughy, J. F. Kamenik, R. Morales, and A. Szynkman, Nucl. Phys. **B915**, 19 (2017), 1611.05032.

[17] V. Khachatryan et al. (CMS), Phys. Lett. **B746**, 132 (2015), 1411.5621.

[18] G. Aad et al. (ATLAS), Eur. Phys. J. **C76**, 11 (2016), 1508.06868.

[19] T. A. collaboration (ATLAS) (2016), ATLAS-CONF-2016-020.

[20] G. Aad et al. (ATLAS), Phys. Rev. **D89**, 072012 (2014), 1304.6386.

[21] V. Khachatryan et al. (CMS), Eur. Phys. J. **C76**, 379 (2016), 1510.03072.

[22] T. A. collaboration (ATLAS) (2016).

[23] C. Collaboration (CMS) (2016).

[24] S. Gori, I.-W. Kim, N. R. Shah, and K. M. Zurek, Phys. Rev. **D93**, 075038 (2016), 1602.02782.

[25] M. J. Dolan, M. Spannowsky, Q. Wang, and Z.-H. Yu, Phys. Rev. **D94**, 015025 (2016), 1606.00019.

[26] Y. K. Jo, S. Y. Choi, Y. J. Roh, and T. J. Kim, J. Korean Phys. Soc. **67**, 807 (2015), 1506.04818.

[27] G. Bevilacqua and M. Worek, JHEP **07**, 135 (2014), 1403.2046.

[28] J. Hajer, Y.-Y. Li, T. Liu, and J. F. H. Shiu, JHEP **11**, 124 (2015), 1504.07617.

[29] P. S. Bhupal Dev and A. Pilaftsis, JHEP **12**, 024 (2014), [Erratum: JHEP11,147(2015)], 1408.3405.

[30] N. Greiner, K. Kong, J.-C. Park, S. C. Park, and J.-C. Winter, JHEP **04**, 029 (2015), 1410.6099.

[31] J. H. Kim, K. Kong, S. J. Lee, and G. Mohlabeng, Phys. Rev. **D94**, 035023 (2016), 1604.07421.

[32] A. M. Sirunyan et al. (CMS), Eur. Phys. J. C **80**, 75 (2020), 1908.06463.

[33] A. M. Sirunyan et al. (CMS), JHEP **07**, 125 (2020), 2003.06467.

[34] N. Craig, J. Galloway, and S. Thomas (2013), 1305.2424.

[35] G. C. Branco, P. M. Ferreira, L. Lavoura, M. N. Rebelo, M. Sher, and J. P. Silva, Phys. Rept. **516**, 1 (2012), 1106.0034.

[36] J. F. Gunion, H. E. Haber, G. L. Kane, and S. Dawson, Front. Phys. **80**, 1 (2000).

[37] N. Cabibbo, Phys. Rev. Lett. **10**, 531 (1963), URL https://link.aps.org/doi/10.1103/PhysRevLett.10.531.

[38] F. Halzen and A. D. Martin, *QUARKS AND LEPTONS: AN INTRODUCTORY COURSE IN MODERN PARTICLE PHYSICS* (1984), ISBN 978-0-471-88741-6.

[39] M. Kobayashi and T. Maskawa, Prog. Theor. Phys. **49**, 652 (1973).

[40] C. Patrignani et al. (Particle Data Group), Chin. Phys. **C40**, 100001 (2016).

[41] J. Charles et al., Phys. Rev. **D91**, 073007 (2015), 1501.05013.

[42] V. Khachatryan et al. (CMS), Phys. Lett. **B736**, 33 (2014), 1404.2292.

[43] M. Aaboud et al. (ATLAS), JHEP **04**, 086 (2017), 1609.03920.

[44] M. Aaboud et al. (ATLAS), Eur. Phys. J. **C77**, 531 (2017), 1702.02859.

[45] A. M. Sirunyan et al. (CMS), Phys. Lett. **B772**, 752 (2017), 1610.00678.

[46] J. M. Campbell, R. Frederix, F. Maltoni, and F. Tramontano, Phys. Rev. Lett. **102**, 182003 (2009), 0903.0005.

[47] P. Kant, O. M. Kind, T. Kintscher, T. Lohse, T. Martini, S. Mölbitz, P. Rieck, and P. Uwer, Comput. Phys. Commun. **191**, 74 (2015), 1406.4403.

[48] M. Brucherseifer, F. Caola, and K. Melnikov, Phys. Lett. **B736**, 58 (2014), 1404.7116.

[49] E. L. Berger, J. Gao, C. P. Yuan, and H. X. Zhu, Phys. Rev. **D94**, 071501 (2016), 1606.08463.

[50] H. Lacker, A. Menzel, F. Spettel, D. Hirschbuhl, J. Luck, F. Maltoni, W. Wagner, and M. Zaro, Eur. Phys. J. **C72**, 2048 (2012), 1202.4694.

[51] T. Lagouri, in *7th International Workshop on the CKM Unitarity Triangle (CKM 2012) Cincinnati, Ohio, USA, September 28-October 2, 2012* (2012), 1212.0013, URL https://inspirehep.net/record/1205139/files/arXiv:1212.0013.pdf.

[52] E. Alvarez, L. Da Rold, J. Mazzitelli, and A. Szynkman (2016), 1610.08451.

[53] R. Contino, T. Kramer, M. Son, and R. Sundrum, JHEP **05**, 074 (2007), hep-ph/0612180.

[54] M. S. Chanowitz and M. K. Gaillard, Nucl. Phys. **B261**, 379 (1985).

[55] D. Pappadopulo, A. Thamm, R. Torre, and A. Wulzer, JHEP **09**, 060 (2014), 1402.4431.

[56] R. Frederix and F. Maltoni, JHEP **01**, 047 (2009), 0712.2355.

[57] P. Langacker, Rev. Mod. Phys. **81**, 1199 (2009), 0801.1345.

[58] B. Hespel, F. Maltoni, and E. Vryonidou, JHEP **10**, 016 (2016), 1606.04149.

[59] G. Aad et al. (ATLAS), JHEP **08**, 148 (2015), 1505.07018.

[60] M. Estévez and E. Álvarez, *Np in the ttbb final state at the lhc*, http://icas.unsam.edu.ar/talks/2016.09.07_NP_in_the_ttbb_final_state_at_the_LHC.Mariel_Estevez.pdf (2016).

[61] J. Alwall, R. Frederix, S. Frixione, V. Hirschi, F. Maltoni, O. Mattelaer, H. S. Shao, T. Stelzer, P. Torrielli, and M. Zaro, JHEP **07**, 079 (2014), 1405.0301.

[62] J. Alwall, M. Herquet, F. Maltoni, O. Mattelaer, and T. Stelzer, JHEP **06**, 128 (2011), 1106.0522.

[63] N. Greiner, A. Guffanti, T. Reiter, and J. Reuter, Phys. Rev. Lett. **107**, 102002 (2011), 1105.3624.

[64] G. Bevilacqua and M. Worek, JHEP **07**, 111 (2012), 1206.3064.

[65] V. Khachatryan et al. (CMS), JHEP **11**, 154 (2014), 1409.7339.

[66] F. Maltoni, G. Ridolfi, and M. Ubiali, JHEP **07**, 022 (2012), [Erratum: JHEP04,095(2013)], 1203.6393.

[67] F. Cascioli, P. Maierhofer, N. Moretti, S. Pozzorini, and F. Siegert, Phys. Lett. **B734**, 210 (2014), 1309.5912.

[68] J. A. Aguilar-Saavedra, R. Benbrik, S. Heinemeyer, and M. Perez-Victoria, Phys. Rev. **D88**, 094010 (2013), 1306.0572.

[69] W. Buchmuller and D. Wyler, Nucl. Phys. **B268**, 621 (1986).

[70] B. Grzadkowski, M. Iskrzynski, M. Misiak, and J. Rosiek, JHEP **10**, 085 (2010), 1008.4884.

[71] S. Fajfer, A. Greljo, J. F. Kamenik, and I. Mustac, JHEP **07**, 155 (2013), 1304.4219.

[72] T. M. P. Tait and C. P. Yuan, Phys. Rev. **D63**, 014018 (2000), hep-ph/0007298.

[73] S. Chatrchyan et al. (CMS), Phys. Rev. Lett. **112**, 231802 (2014), 1401.2942.

[74] G. Aad et al. (ATLAS), JHEP **01**, 064 (2016), 1510.03752.

[75] M. Aaboud et al. (ATLAS) (2016), 1612.07231.

[76] S. Frixione, E. Laenen, P. Motylinski, B. R. Webber, and C. D. White, JHEP **07**, 029 (2008), 0805.3067.

[77] J. Bellm et al., Eur. Phys. J. **C76**, 196 (2016), 1512.01178.

[78] M. Bahr et al., Eur. Phys. J. **C58**, 639 (2008), 0803.0883.

[79] T. Sjöstrand, S. Ask, J. R. Christiansen, R. Corke, N. Desai, P. Ilten, S. Mrenna, S. Prestel, C. O. Rasmussen, and P. Z. Skands, Comput. Phys. Commun. **191**, 159 (2015), 1410.3012.

[80] T. Sjostrand, S. Mrenna, and P. Z. Skands, JHEP **05**, 026 (2006), hep-ph/0603175.

[81] N. Kidonakis, in *Proceedings, 15th International Workshop on Deep-inelastic scattering and related subjects (DIS 2007). Vol. 1 and 2: Munich, Germany, April 16-20, 2007* (2007), pp. 443–446, 0705.2431, URL https://inspirehep.net/record/750785/files/arXiv:0705.2431.pdf.

[82] C. D. White, S. Frixione, E. Laenen, and F. Maltoni, JHEP **11**, 074 (2009), 0908.0631.

[83] J. de Favereau, C. Delaere, P. Demin, A. Giammanco, V. Lemaître, A. Mertens, and M. Selvaggi (DELPHES 3), JHEP **02**, 057 (2014), 1307.6346.

[84] A. Collaboration, Tech. Rep. ATL-PHYS-PUB-2015-022, CERN, Geneva (2015), URL https://cds.cern.ch/record/2037697.

[85] A. Buckley, J. Ferrando, S. Lloyd, K. Nordstrom, B. Page, M. Rufenacht, M. Schonherr, and G. Watt, Eur. Phys. J. **C75**, 132 (2015), 1412.7420.

[86] M. Naseri (ATLAS, CMS), in *Proceedings, 9th International Workshop on Top Quark Physics (TOP 2016): Olomouc, Czech Republic, September 19-23, 2016* (2016), 1703.03558, URL https://inspirehep.net/record/1516915/files/arXiv:1703.03558.pdf.

[87] V. Khachatryan et al. (CMS), Phys. Lett. **B760**, 365 (2016), 1603.06221.

[88] E. Alvarez, M. Estevez and R.M. Sanda Seoane, source scripts for software in this work, GIT repository https://github.com/ro-sanda/Z--explorer.

[89] G. Aad et al. (ATLAS) (2019), 1910.08447.

[90] C. Collaboration (CMS) (2019).

[91] M. Aaboud et al. (ATLAS), Phys. Rev. Lett. **121**, 081801 (2018), 1804.03496.

[92] M. Aaboud et al. (ATLAS), Phys. Rev. **D98**, 032016 (2018), 1805.09299.

[93] A. M. Sirunyan et al. (CMS), JHEP **04**, 031 (2019), 1810.05905.

[94] M. Aaboud et al. (ATLAS), Eur. Phys. J. **C78**, 565 (2018), 1804.10823.

[95] Tech. Rep. CMS-PAS-EXO-19-019, CERN, Geneva (2019), URL https://cds.cern.ch/record/2684757.

[96] G. Aad et al. (ATLAS), Phys. Lett. **B796**, 68 (2019), 1903.06248.

[97] M. Aaboud et al. (ATLAS), JHEP **01**, 055 (2018), 1709.07242.

[98] V. Khachatryan et al. (CMS), JHEP **02**, 048 (2017), 1611.06594.

[99] M. Aaboud et al. (ATLAS), JHEP **03**, 042 (2018), 1710.07235.

[100] A. M. Sirunyan et al. (CMS), Phys. Lett. **B798**, 134952 (2019), 1906.00057.

[101] M. Tanabashi et al. (Particle Data Group), Phys. Rev. **D98**, 030001 (2018).

[102] P. Uwer (2007), 0710.2896.

[103] R. Barbieri, D. Buttazzo, F. Sala, D. M. Straub, and A. Tesi, JHEP **05**, 069 (2013), 1211.5085.

[104] E. Álvarez and M. Estévez, Phys. Rev. D **96**, 035016 (2017), URL https://link.aps.org/doi/10.1103/PhysRevD.96.035016.

[105] E. Alvarez, L. Da Rold, M. Estevez, and J. F. Kamenik, Phys. Rev. D **97**, 033002 (2018), URL https://link.aps.org/doi/10.1103/PhysRevD.97.033002.

[106] A. Cerri, V. Gligorov, S. Malvezzi, J. Camalich, J. Zupan, and M. Della Morte (2018), URL https://e-publishing.cern.ch/index.php/CYRM/article/view/954.

[107] E. Alvarez, M. Estevez, and R. M. S. Seoane (2020), 2005.05194.

[108] G. Van der Velde, Licenciatura thesis, https://bibliotecadigital.exactas.uba.ar/download/seminario/seminario_nFIS000057_VanderVelde.pdf.

[109] F. Demartin, B. Maier, F. Maltoni, K. Mawatari, and M. Zaro, Eur. Phys. J. **C77**, 34 (2017), 1607.05862.